AN INVESTIGATION OF CARRIER RECOVERY TECHNIQUES FOR PSK MODULATED SIGNALS IN CDMA AND MULTIPATH MOBILE ENVIRONMENTS

by
Steven P. Nicoloso

Thesis submitted to the Faculty of the
Virginia Polytechnic Institute and State University
in partial fulfillment of the requirements for the degree of

MASTER OF SCIENCE
in
The Bradley Department of Electrical Engineering

Approved:

Dr. Jeffrey H. Reed
(Chairman)

Dr. Warren Stutzman

Dr. Brian D. Woerner

June 1997
Blacksburg, Virginia

An Investigation of Carrier Recovery Techniques for PSK Modulated Signals in CDMA and Multipath Mobile Environments

by
Steven P. Nicoloso
Committee Chairman: Dr. Jeffrey H. Reed
The Bradley Department of Electrical Engineering

Abstract

The challenge of carrier recovery for digitally phase modulated, suppressed-carrier signals has been the target of much attention in mobile radio system design for many years. Code division multiple access (CDMA) cellular systems are now being deployed in mobile environments, and the performance of carrier recovery for CDMA is much less well understood. CDMA systems typically utilize lower bit energies, relying instead upon coding gain for reliable performance. As an additional challenge, the multiple access interference (MAI) inherent to direct-sequence spread-spectrum (DSSS) signalling further hampers many carrier recovery techniques.

This thesis first surveys general carrier recovery strategies, conventional as well as new, and then applies them to the particular task of recovering a suppressed carrier in mobile CDMA systems. First some of the theory surrounding conventional, closed-loop carrier recovery techniques and several newer open-loop estimation structures based on the *maximum likelihood* (ML) principle is presented. A novel decision-feedback ML phase estimator is proposed. The statistical behavior of this new structure as well as the related squaring estimator are examined and are shown to be equivalent to the stochastic performance of classical closed-loop techniques.

Candidate receivers based upon closed- and open-loop carrier recovery structures are proposed and then examined via simulation. Both forward and reverse cellular links are examined under a variety of both of single-path and multipath conditions. The notion of exploiting cyclostationary MAI in CDMA systems by applying adaptive receiver techniques is also examined, especially as this scheme relies to some extent upon coherent carrier recovery for its promising performance enhancements. This work concludes with recommendations of the best carrier recovery strategies for the variety of environments examined and suggestions for future research are made.

Acknowledgements

The work presented herein was made possible by the personal contributions of a variety of individuals with the Mobile and Portable Radio Research Group (MPRG) to whom I am greatly indebted. Nitin Mangalvedhe has been very involved in every portion of this research. He has made key contributions, both theoretical and practical, throughout. His leadership and broad knowledge have been of benefit not only to me, but to many of my colleagues as well. Francis Dominique, more than any other person, suggested and motivated me toward this research near the very beginning of my tenure at MPRG. Mike Buehrer not only contribued excellent edits to the theoretical portions of this work, but personally contributed to my development as an engineer and thinker. Working side-by-side with Neiyer Correal and Paul Petrus in coding up algorithms for DSP-implementation, though well-outside the scope of the work presented here, was nevertheless a pleasure and an outstanding learning experience for me.

Among the original *GloMo-Gang*, Nevena Zečević and Milap Majmundar were our original investigators of the adaptive filtering receivers examined in this work. I have a memory of Milap sitting down with me very early in my stint at MPRG and explaining quite clearly to me the implementation of adaptive equalization—long before I even knew what an FIR filter was! Dan Bailey, though long matriculated, was very helpful and patient with me in getting started in coding algorithms for our tarket DSP hardware. Don Breslin, Keith Blankenship, Pascal Renucci, Tom Biedka, Greg Durgin, Kim Phillips, Rich Ertel, and Kevin and Donna Krizman have not only made valuable comments to me concerning this work, but have also been great fun to be around at MPRG. Jeff Laster, a legendary student of ours in his own right, served me not only as an experienced learner and teacher but also as a spiritual advisor and friend. His recent moving on to industry creates a void for us that will undoubtedly be difficult to compensate. A host of new names and faces has arrived at MPRG, some of which I hardly know. For each of you, I extend a confident hope that your graduate school experience will be as personally rewarding as has been mine. Many thanks to all!

My committee members have been nothing but helpful both inside and outside of class. Jeff Reed has been everything one could want in an advisor. His recent tenure at Virginia Tech is well-deserved. He unequivocally sees and brings out the very best in all of his students. His constant encouragement, liberality, and trust for me have been strong personal motivators, and I consider Jeff Reed a close personal friend. It has been an honor to have a professor of the stature of Warren Stutzman on my thesis committee. Though the distance between Whittemore Hall and Pointe West Commons has separated us, he has been extremely helpful on a number of occasions, and accomodated my faults. Taking a class, any class, from Dr. Stutzman is highly recommended, though it may take 6-8 weeks to realize "he was probably joking!" Brian Woerner's commitment to his students and teaching is legendary. His expertise in modulation, coding, and information theory as well as simulation has often been helpful throughout this work. Many thanks to each of these men!

The staff of MPRG has been simply superb in supporting each of us. They have not only helped me, time and again, with specific needs but consistently take care of the administrative tasks and day-to-day business of MPRG in such a way as to make these needs transparent. Their only failure may be in doing the job so well as to cause the rest of us to take them for granted. Let me avoid such an error here. To our fine staff, both past and present, Prab Koushik, Wayne Erchak, Annie Wade, Kathy Wolfe, Jenny Frank, Hilda Reynolds, Aurelia Scharnhorst, Rennie Givens, and Lori Hughes, I salute and thank you for your hard work on my behalf, and on behalf of all of us.

Much of my financial support for the last two years was provided by the Defense Advanced Research Projects Agency (DARPA) who expressed their faith in the work of the MPRG by sponsoring the Global Mobile Communications Initiative (GloMo). As a participant in this project, I developed most of the professional relationships I now have and learned most of what is presented here and even more that is not.

I'd like to point out that my family has endured these last five years of my being a full-time student with remarkable grace and strength. To Robin, who was there from the beginning, all of my love and gratitude. And for Daniel and Karen, who "popped up" along the way as a serendipitous by-product of love, my committment to getting this degree, though you probably cannot understand it now, has been both because of you and for you. To my parents, Luigi and Karen Nicoloso, I give heartfelt thanks not only for the financial sacrifices which made graduate school possible for me but for the sacrifice of love and support upon which no price can be placed. The participants of Grace Covenant Presbyterian Church have been very much like a family for us in Blacksburg. We love each

of you, and have constantly benefited from your love and strength. Finally, to my LORD and Savior, Jesus Christ, God of very God, I reserve the highest of all praise!—in whose life I find life, and to whose wisdom I forever humbly submit.

Contents

List of Tables

List of Figures

Chapter 1

Introduction

1.1 Motivations for Research

Nearly three years ago, members of the Mobile and Portable Radio Research Group (MPRG) began investigating adaptive interference suppression for CDMA systems, sponsored by the Defense Advanced Research Projects Agency's (DARPA's) Global Mobile Information Systems (GloMo)* Intiative. Early results from this research suggested dramatic performance enhancements and, thus, corresponding capacity increases for certain cellular systems. These improvements resulted from the ability of a fractionally-spaced adaptive equalizer to both mitigate code division multiple access (CDMA) interference that shared spectral properties with the signal of interest (SOI) and coherently combine multiple paths of the SOI when fractional sampling allows sufficient time resolution for the various paths.

As is common with preliminary investigations, however, certain simplifying and necessary assumptions were made concerning the adaptive receivers under investigation. One assumption was the availability of an ideal coherent reference carrier for the SOI. This assumption is somewhat realistic when a pilot tone is transmitted on the forward link of a CDMA system, such as in the IS-95 U.S. digital CDMA standard. On the reverse link of this system and in many other potential multiple access strategies planned for the Industrial, Scientific, and Medical (ISM) bands in the U.S., however, the existence of pilot tone is either impossible or not planned.

We therefore began to examine some adaptive receiver structures in the presence of frequency offsets. The immediate result was catastrophic degradation and failure. This implied a fundamental need for either carrier recovery or the redesigning of adaptive algorithms to work with differentially coherent reception. The latter solution was quickly

*GloMo was known formerly as the Wireless Adaptive Mobile Information System (WAMIS) program.

discovered and is outlined in section 4.2.7 of this thesis. Though the performance degradation associated with moving from coherent to differentially coherent reception is well-known for conventional receivers, it seemed to be *amplified* in adaptive receivers, as discussed in section 7.1. This left us with a nagging question: How can we "buy back" some or all of this performance degradation caused by differential detection? The question prompted others and led to the research described in this thesis.

1.2 Thesis Overview

The layout of this thesis serves not only the thematic organization of the investigations contained herein, but generally represents their chronological order as well. This chapter begins to describe the challenges that motivated the work. The literature survey presented in Chapter 2 was really the beginning of investigative process. Therein we searched a wide range of historically noteworthy as well as more recent literature concerning synchronization, concentrating on applications to suppressed-carrier recovery. Making sense of this literature led to the work presented in Chapters 3 through 5. In these chapters, a theoretical substrate is formed upon which the design of carrier recovery structures relevant to this particular application, mobile CDMA environments, can be based. As such, these three chapters serve very much as an introduction to the topic of carrier recovery.

Chapter 6 bridges the gap between the more theoretical observations of the previous chapters and the results-oriented chapters that conclude this work. Therein, we describe our simulation strategy, the assumptions that have been kept and those that have been thrown out, and the details of wireless CDMA system under investigation. We use all these details to propose candidate receiver structures with and without carrier recovery for observation. The field is immediately narrowed by some preliminary simulation results. This yields a field of "finalists," including both conventional and adaptive receivers, for further simulation in Chapters 7 and 8.

The additive white Gaussian noise (AWGN) channel is given significant attention in Chapter 7. The relative performance of carrier recovery strategies is presented, always in view of the performance of differential detection and ideal coherent reception. Substantive remarks are made about the susceptibility of carrier recovery strategies to degradation due to spread-spectrum multiple access interference (MAI). Chapter 8 moves beyond the AWGN channel to investigate the performance of candidate architectures in more challenging conditions faced in a mobile environment, viz., those of fading due to multipath. Flat fading and a variety of frequency-selective environments are examined. A three-finger differentially coherent RAKE receiver, similar to one used in IS-95, is also simulated to provide an

important basis for comparison. At all times in these chapters, both forward and reverse cellular links are considered.

Finally, this presentation concludes with a review of the significant observations and contributions of this research and numerous recommendations for future research. We ultimately realize that this work has only scratched the surface of problem of carrier recovery for CDMA, especially as it is linked to adaptive interference suppression. We therefore intend for this effort to be seen as a solid *introduction* to this issue, and hope that it will prove seminal for such future work.

1.3 Overview of PSK Reception

Before moving on to the chronicle the research effort in the chapters that follow, it is useful to briefly give a high-level view of some important concepts and notation that will be called upon throughout this work. To this end, we give a brief summary of digital phase shift keying (PSK) modulation strategies in section 1.3.1. We then define *coherent reception* in section 1.3.2, and further explain the notion of differential detection for PSK. Section 1.3.3 concludes this chapter with a brief introduction to the notions of closed- and open-loop phase compensation. This serves as preview for much of the theoretical and descriptive work to follow.

1.3.1 PSK Signals

Receiver architectures for digital signals either require or benefit from accurate estimation of a variety of signal parameters. Among these are amplitude, phase, frequency, and delay. In land mobile and cellular radio, the use of *phase shift keying* (PSK) has become a very popular method for digital signaling because it represents a well-balanced tradeoff between energy and bandwidth efficiency for the given mobile environment. Receivers for digital PSK expect to receive a signal of constant magnitude. This simplifies the analysis of the signal and the design of appropriate receiver structures. The information contained in a received PSK signal is, by definition, embedded either in the absolute or relative phase of the received signal. Thus the received signal may be represented by

$$s(t) \quad = \quad \sqrt{2P} \cdot \cos\left(2\pi f_c t + \phi(t) + \theta(t)\right) + n(t) \tag{1.1}$$

where P is the received signal power, f_c is the received carrier frequency in Hz, $n(t)$ is, for now, a random bandpass process, $\theta(t)$ is the possibly time-varying phase of the carrier, and

$$\phi(t) \in \left\{ \frac{2\pi m}{M} \ , m = 1, 2, \ldots, M-1 \right\}$$

is the information contained in the signal where M is the number of points in the signal constellation. The desire to correctly estimate $\phi(t)$ motivates the design of the digital receiver.

Consider next the quadrature downconversion of this signal by a local reference carrier generated by the receiver as outlined Fig. 1.1, viz.,

$$v_d(t) = \cos\left(2\pi f_c t + \hat{\theta}(t)\right) \qquad \text{and} \qquad v_q(t) = -\sin\left(2\pi f_c t + \hat{\theta}(t)\right)$$

where we have assumed that the instantaneous frequency of the VCO exactly matches the incoming carrier, and $\hat{\theta}(t)$ is an estimate of its phase.[†] Allowing the dependence of $\hat{\theta}$ on time allows this simplification without loss of generality. This yields

$$\begin{aligned} i(t) &= s(t) \cdot v_d(t) \\ &= \sqrt{\frac{P}{2}}\left[\cos\left(\phi(t) + \theta(t) - \hat{\theta}(t)\right) + \cos\left(4\pi f_c t + \phi(t) + \theta(t) + \hat{\theta}(t)\right)\right] \\ &\quad + n_d(t) \end{aligned} \tag{1.2}$$

and

$$\begin{aligned} q(t) &= s(t) \cdot v_q(t) \\ &= \sqrt{\frac{P}{2}}\left[\sin\left(\phi(t) + \theta(t) - \hat{\theta}(t)\right) - \sin\left(4\pi f_c t + \phi(t) + \theta(t) + \hat{\theta}(t)\right)\right] \\ &\quad + n_q(t) \end{aligned} \tag{1.3}$$

where n_d and n_q are, for now, unspecified noise processes. Assuming that the low pass filters (LPFs) work well, the double frequency terms in (1.2) and (1.3) may be neglected. Sampling at time, $t = kT$, then yields

$$i_k = \sqrt{\frac{P}{2}} \cdot \cos\left(\phi_k + \theta_k - \hat{\theta}_k\right) + n_{d,k} \tag{1.4}$$

and

$$q_k = \sqrt{\frac{P}{2}} \cdot \sin\left(\phi_k + \theta_k - \hat{\theta}_k\right) + n_{q,k} \tag{1.5}$$

as input to the baseband detector where ϕ_k is still the transmitted symbol and $n_{d,k}$ and $n_{q,k}$ are samples of the heretofore unspecified noise processes. It will be convenient to regard i_k and q_k together as single complex-valued sample,

$$r_k = i_k + jq_k = \sqrt{P} \cdot e^{j\left(\phi_k + \theta_k - \hat{\theta}_k\right)} + n_{d,k} + jn_{q,k} \tag{1.6}$$

in the chapters that follow.

[†]Throughout the thesis, we consistently view the quadrature downconversion process as multiplication by $\cos(\cdot)$ and $-\sin(\cdot)$ due to its natural correspondence with multiplication by $\exp(-j(\cdot))$.

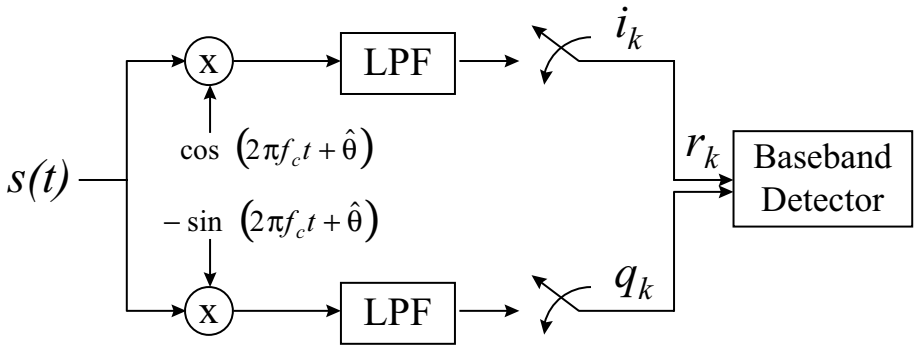

Figure 1.1: Basic detection structure for PSK signals

1.3.2 Coherent Reception

What are the challenges to obtaining an accurate estimate of $\hat{\theta}_k \approx \theta(kT)$, or equivalently, coherent carrier recovery? There are two broad categories. First of all, θ may be time-varying for any number of reasons. Residual carrier offset introduces a constant rotation in the phase parameter that can be a significant fraction of the baud rate in practical systems. Doppler spread has the same effect as residual offset, but may vary with time, creating non-zero second and higher order derivatives of the instantaneous phase. Fading due to multipath further complicates matters by introducing potentially wild variations in carrier phase over just a few symbols and providing multiple carriers with respectively arbitrary phases to the synchronization system.

The other major challenge to obtaining $\hat{\theta}$ comes from the noise terms n_d and n_q. Portions of these noise terms come from realizations of an additive white Gaussian noise (AWGN) channel. AWGN introduces random perturbations in the phase and amplitude of r_k, that obviously will hinder the prediction of the carrier phase and thus the transmitted symbol, ϕ. Still AWGN is zero mean, uncorrelated, and stationary, the effects of which might somehow be averaged out. More pathological effects may be observed when co-channel and adjacent-channel interference are taken into account. These can make the statistics of the noise non-stationary and quite difficult to predict.

Still there are certain advantages to coherent reception. First, many equalization strategies require coherent carrier recovery. As equalization strategies become more popular in mobile radio, the motivation to coherently detect PSK signals increases. In addition, coherent reception of PSK provides a 1 to 3 dB power advantage versus noncoherent techniques.

Coherent detection in a mobile channel is extremely challenging. Differentially coherent phase shift keying (DPSK) simplifies the challenge of phase estimation by using the previous

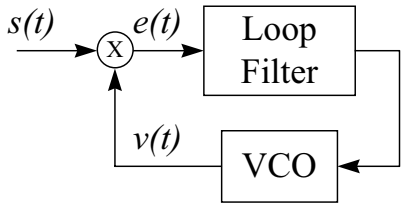

Figure 1.2: Example of a feedback control system: A simple PLL model

phase estimate as a reference for the current one, viz.,

$$r_k \cdot r_{k-1}^{\star} = P \cdot e^{j(\phi_k - \phi_{k-1} + \theta_k - \theta_{k-1})} + \text{noise} \ . \tag{1.7}$$

This is based on the generally safe assumption that θ_k changes very little between successive symbols, and therefore $\theta_k - \theta_{k-1}$ is very close to zero. Note that the transmitted symbol must first be differentially encoded at the transmitter by $\Delta\phi = \phi_k - \phi_{k-1}$, the difference between the current information symbols and the previous one. However, because the receiver is using a noisy reference, i.e., the previous estimate, M-ary DPSK (MDPSK) suffers in performance versus coherent M-ary PSK (MPSK). This degradation can be up to 3 dB for large M but is only about 1 dB for $M = 2$. Consequently, there is now a great deal of interest in schemes to perform *coherent* detection of DPSK. Coherently detected MDPSK differs only by about a factor of two in BER (for most E_b/N_o ratios of interest) from MPSK. Such schemes, of course, lead us back to all the same challenges of estimating instantaneous carrier phase mentioned above. It is, therefore, one purpose of this work to present a wide overview of techniques for the estimation and/or compensation of carrier phase and frequency offset in PSK reception.

1.3.3 Closed Vs. Open Loop Compensation

Phase and frequency synchronization techniques can be broadly categorized as either *closed-loop* or *open-loop* schemes. Closed-loop schemes involve a feedback path in the system to make corrections for errors. The basic design of such a system is illustrated by the ubiquitous PLL detailed in Fig. 1.2. The PLL is a very basic feedback control system consisting of a phase detector (PD), a loop filter, and a voltage controlled oscillator (VCO). This basic configuration is similar to that of an automatic gain control (ACG) loop or an automatic frequency control (AFC) loop. The shared feature of all such control schemes is that an error signal is fed back to the system input to drive the error term to zero at steady-state.

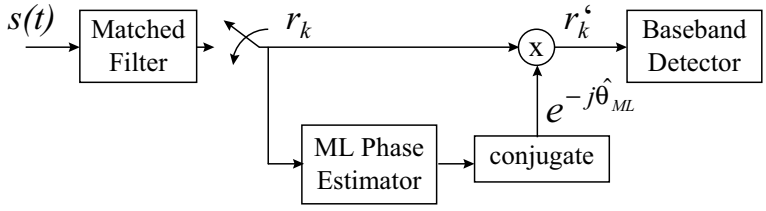

Figure 1.3: Example open-loop compensation scheme: ML phase estimator

In contrast to closed-loop, open-loop schemes do not contain a feedback path. Open-loop parameter estimation is classically derived from either *maximum likelihood* (ML) or *maximum a posteriori* (MAP) decision rules. These, in the case of no prior knowledge of the input parameter vector, are shown to be equivalent in [1]. Figure 1.3 provides an example of an open-loop phase estimation scheme derived from the ML principle. Note that the removal of phase occurs at the output of the loop rather than at the input.

Chapters 3 through 5 provide an overview of both closed-loop and open-loop phase and frequency compensation schemes. First, the PLL is described and analyzed. Performance measures are described, and the discrete-time implementation of second and third-order PLLs is derived. Then, in Chapter 4, we apply the concepts of the PLL to the task of carrier recovery, and review a variety of techniques for this task, and their performance. Also in Chapter 4, we introduce several open-loop phase estimation structures based on the ML principle. Both sets of structures are applied to the task of detection of PSK waveforms. Then in Chapter 5, coverage of AFC and its application to carrier recovery issues are presented.

Chapter 2

A Brief Survey of Prior Research

Before moving on to detailed descriptions of carrier recovery techniques and structures presented in Chapters 3 through 5, a brief review of pertinent literature concerning this problem is in order. In this chapter we review the literature and thus the history concerning this far-reaching topic. Closed-loop synchronization, addressed in section 2.1, has a very diverse history reflected in its seminal papers over the last seventy years. Open-loop estimation in section 2.2, while having a rich literature as well, has only more recently been applied to the task of carrier recovery. Insofar as they are based upon newer concepts, open-loop techniques therefore get somewhat less attention in this chapter—a deficiency that will hopefully be made up in later chapters of this work.

2.1 Closed-Loop Synchronization

The subject of classical closed-loop phase and frequency synchronization is both rich and diverse. The first description of the *phase-locked loop* (PLL) was by English physicist Edward Appleton, appearing in the *Proceedings of the Cambridge Philosophical Society* in 1923.[2] The subject remained in relative obscurity until just before World War II when the PLL began to find its way into the advancing communication technologies of the day, specifically frequency modulation (FM). The 1950s saw the recommendations of the National Television Standard Committee (NTSC) for commercial broadcast television as well as an increased interest in suppressed-carrier techniques for wireless communications. These spawned a rich period of study in phase and frequency lock techniques. Gruen's 1953 paper [3] was one of the first published works to deal specifically with the subject of *automatic frequency control* (AFC). This was in an application of retrieving the color subcarrier in the NTSC standard. Costas [4] proposed a PLL capable of demodulating a suppressed-carrier AM signal. At

the time, the double side-band suppressed-carrier (DSB-SC) modulation was presented as a favorable alternative to single side-band modulation, attracting a great deal of interest in military applications where low probability of jam and/or intercept was crucial. The Costas loop and a whole family of related structures are now standard detection schemes for suppressed-carrier, coherent PSK.

Gupta's tutorial paper [2] contains 188 references that survey the history of PLLs up to 1975. The paper also provides a concise survey of a wide variety of PLLs and related topics. In addition to Gupta's survey, Blanchard [5] and Gardner[6] are standard textbooks on the subject, that should prove adequate for all but the most serious students of phase-lock phenomena. Lindsey[7] and Lindsey & Simon [8] are described by Gardner as "massive assaults" on the difficult problems associated with PLLs. Taken together these works, without doubt, constitute the most comprehensive study of the subject ever undertaken. In 1966, Viterbi [9] contributed the monumental undertaking of an exact non-linear solution to the first-order PLL. References [10] and [11] are edited collections that are a rich resource for seminal papers on the performance and design of PLLs and AFC loops for a large number of applications.

Over the years, the study of phase and frequency loops has diverged into a number of separate areas. References [2], [10], and [11] do a good job in pointing the student or designer interested in these different areas to suitable publications ranging from the introductory to the advanced. We make a few additional recommendations here, as well. A good introductory treatment of the subject of digital PLLs may be found in [12]. For further study, references [13], [14], and [15] should prove helpful.

Application of PLLs to symbol timing recovery and tracking is best summarized in Franks classic tutorial [16]. J. J. Spilker in [17] and [18] was one of the earliest writers on the subject, proposing the delay-lock discriminator for binary signals. Early treatments of carrier tracking and Costas loops may be found in [19] - [25].

Automatic frequency control (AFC) loops, though based on the same error feedback principle, differ in a strict sense from PLLs. As will be shown, the latter perform phase-coherent tracking by feeding back an error as a function of the *phase* difference between the signal of interest (SOI) to the reference. AFC loops, strictly speaking, are non-coherent devices where the feedback error depends on the *frequency* difference. The subject of AFC, though well-studied, is not nearly so widely published as that of phase-locked loops. Two reasons for this are:

1. The design and performance AFC loops are a natural extension of well-established

PLL theory, as we show in Chapter 5. If one can build a PLL, then one can probably build an AFC loop.

2. AFC loops are not nearly as ubiquitous as PLLs. The latter are found in nearly every conceivable application, from industrial control to radio astronomy. In contrast, the use of AFC loops is generally limited to RF communications and ranging applications.

Two references, in particular, are noteworthy in the study of AFC. Natali's 1984 seminal paper [26] proposes a number of practical structures for AFC implementation, all but one of which is digital. Gardner in [27] provides an excellent tutorial on the subject, concentrating on the structure of frequency difference detectors (FDDs). AFC is often seen as an aid to frequency acquisition of a PLL. Two early works in this area are from Cahn [28] and Messershmitt [29]. Later works of interest include [30]- [32].

2.2 Open-Loop Schemes

Open-loop phase and frequency synchronization schemes are based on either the *maximum a priori* (MAP) or *maximum likelihood* (ML) parameter estimation principles. As such, these are generally *feedforward* techniques in that the signal parameter is actively estimated and then treated as a statistic for a detection algorithm. This is a completely different approach from classical closed-loop schemes, which, as noted above, use error feedback control to minimize the error in the received signal. Before the days of high-performance digital computers and signal processors, the idea of open-loop phase and frequency compensation was primarily an academic one, finding little application in the design of real-time communication systems. Interest in open-loop approaches has, however, increased tremendously as it has become more and more feasible in recent years to implement them.

Since these techniques are relatively new in their application to real communication systems, their literature is scattered and not well-organized. One commonality in many papers on open-loop estimation is the citation of Van Trees' [33] - [35] classic texts. Meyr and Ascheid in [36] devote several chapters to open-loop phase and frequency estimation, in addition to providing a comprehensive treatment of classical loops. Proakis' [1] Chapter 6 provides one of the best introductions to the topic. Feedforward estimation techniques embedded within practical receivers have been suggested by Simon and Divsalar in the particularly useful papers [37] - [41]. Recent, noteworthy references on the subject also include [42] - [46]. It is important to note here that likelihood rules for estimation do not *necessarily* imply open-loop detection structures. In an unusual and interesting paper,

Simon and others, in [47], rigorously show that closed-loop recovery schemes may be derived from the likelihood functions of estimation theory.

Chapter 3

The Phase-Locked Loop

Feedback phase and frequency control loops consist of three main components: 1) an error detector of some sort, which for the PLL is a PD, modeled in Figure 3.1 as a multiplier, 2) a loop filter, and 3) a VCO. Note that for an AFC loop the error term is given by a *frequency difference detector* (FDD). PLLs can either be fully analog circuits, partially analog and partially digital, or fully digital. Moreover, PLLs find many uses in communications. They can be used for frequency demodulation, providing superior performance over a conventional discriminator circuit. They are also used in de-noising oscillators, in frequency multipliers and dividers, in frequency synthesizers, and in synchronizing digital signals. We are mainly interested in the PLL for the purpose of carrier recovery, a simple description of which is as follows.

3.1 Introductory View

Consider the situation portrayed in Figure 3.1 where an input signal,

$$s(t) = \cos(\omega_c t + \theta) \tag{3.1}$$

where ω_c is the radian frequency of the carrier and θ is its arbitrary phase, is applied to the input of the receiver and multiplied by the local reference,

$$v(t) = -\sin(\omega_c t + \hat{\theta}) \; . \tag{3.2}$$

We may assume, without loss of generality, that the input and reference frequencies are identical if we consider $\hat{\theta}$, an estimate of θ, to be a time-varying parameter. The output of the PD is an error signal given by

$$e(t) \;\; = \;\; s(t) \cdot v(t)$$

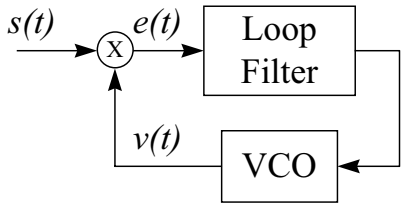

Figure 3.1: Simple illustrative PLL model

$$\begin{aligned} &= -\cos(\omega_c t + \theta) \cdot \sin(\omega_c t + \hat{\theta}) \\ &= -\frac{1}{2}\sin(2\omega_c t + \theta + \hat{\theta}) + \frac{1}{2}\sin(\theta - \hat{\theta}) \,. \end{aligned} \tag{3.3}$$

In practice, the double frequency term will lead to a ripple in the error control signal, which can be a problem in practical systems and compensated for with a lowpass filter (LPF). The loop filter is, itself, a LPF with a very narrow bandwidth. Therefore, for the purposes of introduction, we neglect the double frequency term and simplify (3.3) as

$$e(t) = \frac{1}{2}\sin(\theta - \hat{\theta}). \tag{3.4}$$

The loop filter, $F(s)$, for the moment, is simply some sort of lowpass filter for the error signal. The design of this filter, the specification of its order and related parameters, will require the most attention as the discussion of PLL design progresses.

3.2 Linearized Analog PLL Model

Assuming that after some convergence period the error term, $e(t)$, will become small, the approximation $\sin\left(\theta - \hat{\theta}\right) \approx \theta - \hat{\theta}$ may be applied. This yields the equivalent phase domain model of Figure 3.2 where the VCO is modeled as a perfect integrator with gain K_o. The gain factor, K_d, is that of the detector.* Linearization allows the use of the Laplace transform,

$$X(s) = \mathcal{L}\left\{x(t)\right\} \triangleq \int_0^\infty x(t)e^{-st}dt \,. \tag{3.5}$$

Thus the transform of the input phase, $\mathcal{L}\{\theta(t)\}$ is denoted by $\Theta(s)$. Similarly, $\mathcal{L}\{\hat{\theta}(t)\} = \hat{\Theta}(s)$, and, for the phase error, $\mathcal{L}\{\phi(t)\} = \Phi(s)$. We have then, from linear system theory, that the closed-loop transfer function, i.e., the relationship of the input phase to the output phase estimate, may be given by

$$H(s) \doteq \frac{\hat{\Theta}(s)}{\Theta(s)} = \frac{K_d K_o F(s)}{s + K_d K_o F(s)} \,. \tag{3.6}$$

*For a more thorough explanation of detector gain, see section 3.4.1.

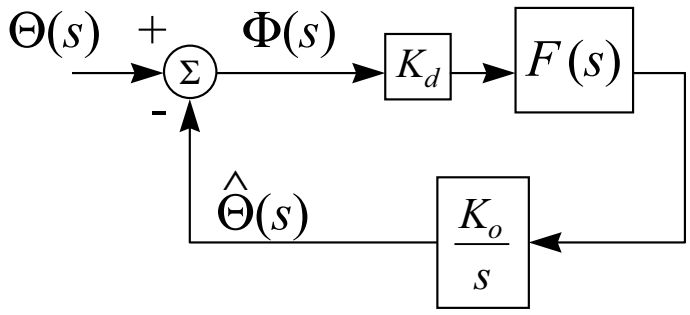

Figure 3.2: Linearized, phase domain model of PLL

3.2.1 The Second-Order PLL

The order of a PLL, based upon servo terminology, is defined by the number of "perfect integrators," n, in the loop. An integrator defined by $1/s$ is merely a pole placed at $s = 0$, or DC. Since the VCO represents one such pole, n is one more than the number of integrators in $F(s)$. Thus, an nth-order PLL may be constructed using an $(n-1)$th-order loop filter. A first-order RC filter built with a high gain DC amplifier (as shown in Figure 3.3) is of the most interest here since it meets this criterion. This will lead to the very well-known and widely implemented second-order PLL. Such a filter has a transfer function,

$$F(s) = \frac{s\tau_2 + 1}{s\tau_1} \tag{3.7}$$

where τ_1 and τ_2 are the time constants of the network, defined in Figure 3.3. Letting

$$\tau_1 = \frac{K_d K_o}{\omega_n^2} \text{ and } \tau_2 = \frac{2\zeta}{\omega_n} \tag{3.8}$$

we obtain

$$H(s) = \frac{2\zeta\omega_n s + \omega_n^2}{s^2 + 2\zeta\omega_n s + \omega_n^2} \tag{3.9}$$

where ω_n and ζ are the well-known parameters of natural frequency in [rad/s] and damping factor, respectively. Equation (3.9) shall be called the canonical, continuous-time, second-order PLL model.

Use of this particular second-order model is advantageous for a couple of reasons. Since it a true second-order loop[†], it is applicable to a wide range of applications including carrier recovery. Furthermore, specifying $\zeta = \frac{1}{\sqrt{2}}$ is shown in [6] to produce the optimal second-order PLL as discussed in section 3.6.

[†]A second-order loop built with a RC lag filter would technically be second-order, but Gardner [6] shows that due to a lack of high DC gain, it should be viewed as a modified first-order PLL.

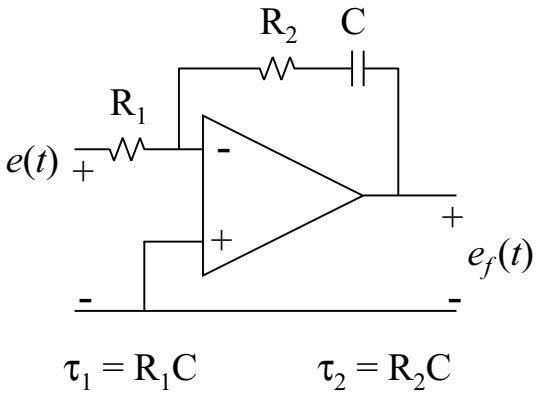

Figure 3.3: High gain, active, lowpass filter suitable to realize loop filter in canonical PLL model

The simplest of all possible PLLs, one of first-order, may be constructed with a loop filter, $F(s)$, equal to a constant. While such a PLL does have many applications, it is of no value for the task of carrier recovery since it compensates poorly in the presence of frequency offset and fails utterly to compensate in the presense of a frequency ramp. A second-order loop filter will lead to a third-order PLL that will prove useful for the task of carrier recovery.

3.2.2 The Third-Order PLL

Though not as commonly used as the second-order, the third-order PLL does have some advantages. Most importantly, it is capable of tracking a frequency ramp with zero steady-state error. The second-order PLL can only do so with a finite steady-state error.

At the heart of the third-order PLL is the second-order loop filter specified by

$$F(s) = \frac{s^2 + a_2 s + a_3}{s^2} \tag{3.10}$$

where a_2 and a_3 are design parameters. Note that the loop filter now has two poles at DC in addition to that obtained from the VCO. Substituting (3.10) into (3.6), we find

$$H(s) = \frac{K_o K_d \left(s^2 + a_2 s + a_3\right)}{s^3 + K_o K_d \left(s^2 + a_2 s + a_3\right)} \,. \tag{3.11}$$

For the sake of simplicity, it is convenient to define the various parameters in terms of a corner frequency, ω_3. Letting $K_o K_d = 2\omega_3$, $a_2 = \omega_3$, and $a_3 = \frac{1}{2}\omega_3^2$, we obtain

$$H(s) = \frac{\omega_3^3 + 2\omega_3^2 s + 2\omega_3 s^2}{\omega_3^3 + 2\omega_3^2 s + 2\omega_3 s^2 + s^3} \,. \tag{3.12}$$

Equation (3.12) shall be denoted as the canonical, continuous-time, third-order PLL model. This loop is shown in [6] to be optimal according to the Wiener criteria discussed in section 3.6. Having to specify only the single parameter ω_3 simplifies the design process and streamlines further discussion of the third-order PLL.

The particular loops defined by (3.9) and (3.12) are well-known and well-analyzed in the classic PLL treatments of [5], [6], and [36]. Due to these and related treatments, theoretical results for the performance of these PLLs, the steady-state variance of output phase estimate as well as cycle slipping characteristics, are well known. As such, these will serve as baselines for the simulations presented later in this work. Finally, we choose to implement these classical loops because the design parameters, ω_n and ζ (which is usually chosen to be $\frac{1}{\sqrt{2}}$) for the second-order, and ω_3 for the third-order, have simple, intuitively understandable meanings. This simplifies the design process while preserving the well-known properties of these loops. We will examine these performance characteristics in section 3.4, but first proceed with a derivation of the discrete-time PLL that will be useful for computer simulation and, ultimately, for integration in a fully digital receiver.

3.3 Derivation of Discrete-time PLL Models

3.3.1 Discrete-time Second-Order PLL

We begin by considering the canonical *continuous-time* transfer function given by (3.9). Note that the poles of $H(s)$ are very near zero, i.e., $\omega_n \ll 2\pi/T$, enabling a straightforward application of the bilinear z-transform (BZT) without frequency pre-warping. This allows a simple substitution for s. Let

$$s = \frac{2}{T} \cdot \frac{1 - z^{-1}}{1 + z^{-1}} \tag{3.13}$$

where T is the sampling interval in seconds. Substituting (3.13) into (3.9) leads to the following expression for $H(z)$:

$$H(z) = \frac{\hat{\Theta}(z)}{\Theta(z)} = \frac{b_0 + b_1 z^{-1} + b_2 z^{-2}}{a_0 + a_1 z^{-1} + a_2 z^{-2}} \tag{3.14}$$

where

$$\begin{aligned} b_0 &= (\omega_n T)^2 + 4\zeta\omega_n T & \qquad a_0 &= 4(\omega_n T)^2 + \zeta\omega_n T + 4 \\ b_1 &= 2(\omega_n T)^2 & \qquad a_1 &= 2(\omega_n T)^2 - 8 \\ b_2 &= (\omega_n T)^2 - 4\zeta\omega_n T & \qquad a_2 &= (\omega_n T)^2 - 4\zeta\omega_n T + 4 \end{aligned}$$

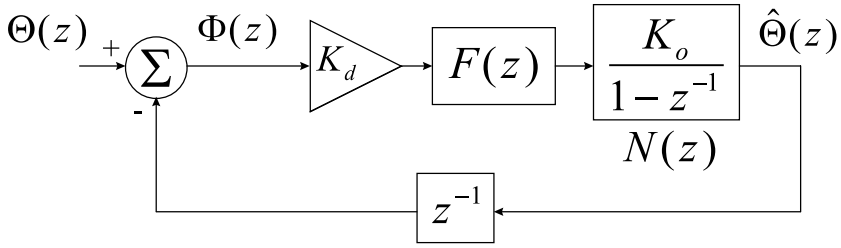

Figure 3.4: Discrete-time, phase domain model of PLL

which we will denote as the canonical discrete-time transfer function. It is expected that any discrete-time implementation of this transfer function would match the performance of the canonical continuous-time model.

Discrete-time, digital implementation of the PLL requires adjustment in the modeling of the loop components. Note that the VCO in Figure 3.2 has been replaced in Figure 3.4 with a numerically controlled oscillator (NCO), $N(z)$. Whereas the VCO was modeled as a perfect *integrator*, the NCO is modeled as a perfect *accumulator*. Thus, the NCO is now modeled by the transfer function

$$N(z) = \frac{K_o}{1 - z^{-1}} \tag{3.15}$$

where K_o is the output voltage amplitude of the device. This is an accurate model for many off-the-shelf NCOs currently available. Note also the addition of the delay in the feedback path. This is needed to make the system causal.

Given these modifications, we now wish to find a model for the loop filter, $F(z)$[‡], that will preserve the overall transfer function of (3.14). From linear system theory, we know that

$$\begin{aligned} H(z) = \frac{K_d F(z) N(z)}{1 + K_d F(z) N(z) z^{-1}} \implies F(z) &= \frac{H(z)}{K_d N(z)\left[1 - H(z) z^{-1}\right]} \\ &= \frac{1}{K_d K_o} \cdot \frac{H(z)\left(1 - z^{-1}\right)}{1 - H(z) z^{-1}} \,. \end{aligned} \tag{3.16}$$

Solving directly for $F(z)$ leads to a third-order loop filter, which is somewhat surprising since the overall transfer function is only of order two and the continuous-time loop filter is of order one. It turns out that we can obtain the expected performance of the second-order discrete-time PLL using only a first-order loop filter.

[‡]Note $F(z)$ will *not*, in general, be the BZT of $F(s)$.

To create this filter we specify a loop filter, $F_2(z)$[§], and constrain it to be of first-order, as is its continuous-time cousin, $F(s)$, with a pole at $z = 1$, i.e., at DC. For convenience, we specify the filter by

$$F_2(z) = \frac{g_0 + g_1 z^{-1}}{1 - z^{-1}} \,. \tag{3.17}$$

Then $H_2(z)$ is given by

$$\begin{aligned} H_2(z) &= \frac{K_d F_2(z) \cdot \left(\frac{K_o z^{-1}}{1-z^{-1}}\right)}{1 + K_d F_2(z) \cdot \left(\frac{K_o z^{-1}}{1-z^{-1}}\right)} \\ &= \frac{K_d K_o \left(g_0 z^{-1} + g_1 z^{-2}\right)}{1 + \left(K_d K_o g_0 - 2\right) z^{-1} + \left(K_d K_o g_1 + 1\right) z^{-2}} \,. \end{aligned} \tag{3.18}$$

Note that $H_2(z)$ cannot, in general, be made to equal the canonical $H(z)$ given in (3.14). Instead, following the reasoning of [48], we merely equate the denominator of (3.18) with the normalized denominator of (3.14), i.e., let

$$K_d K_o g_0 - 2 = \frac{a_1}{a_0} \qquad \text{and} \qquad K_d K_o g_1 + 1 = \frac{a_2}{a_0} \,.$$

After some algebra, the forward coefficients g_0 and g_1 in (3.17) are found to be

$$g_0 = \frac{1}{K_d K_o}\left(\frac{a_1}{a_0} + 2\right) \quad \text{and} \quad g_1 = \frac{1}{K_d K_o}\left(\frac{a_2}{a_0} - 1\right) \tag{3.19}$$

where the a_is are as defined in 3.14. Thus, the design of the discrete-time second-order PLL is complete.

3.3.2 Discrete-time Third-Order PLL

For the third-order PLL, we follow exactly the same procedure as for the second-order. Substituting (3.13) into (3.12), we obtain

$$H(z) = \frac{\hat{\Theta}(z)}{\Theta(z)} = \frac{d_0 + d_1 z^{-1} + d_2 z^{-2} + d_3 z^{-3}}{c_0 + c_1 z^{-1} + c_2 z^{-2} + c_3 z^{-3}} \tag{3.20}$$

where

$$\begin{aligned} d_0 &= (\omega_3 T)^3 + 4(\omega_3 T)^2 + 8\omega_3 T & c_0 &= (\omega_3 T)^3 + 4(\omega_3 T)^2 + 8\omega_3 T + 8 \\ d_1 &= 3(\omega_3 T)^3 + 4(\omega_3 T)^2 - 8\omega_3 T & c_1 &= 3(\omega_3 T)^3 + 4(\omega_3 T)^2 - 8\omega_3 T - 24 \\ d_2 &= 3(\omega_3 T)^3 - 4(\omega_3 T)^2 - 8\omega_3 T & c_2 &= 3(\omega_3 T)^3 - 4(\omega_3 T)^2 - 8\omega_3 T + 24 \\ d_3 &= (\omega_3 T)^3 - 4(\omega_3 T)^2 + 8\omega_3 T & c_3 &= (\omega_3 T)^3 - 4(\omega_3 T)^2 + 8\omega_3 T - 8 \,. \end{aligned}$$

[§]Use of the subscript $_2$, is not intended to cause confusion. It is chosen because it leads to a second-order discrete-time PLL. Similarly, the subscript $_3$ is chosen later for the loop filter in a third-order PLL.

But similar to the loop filter for the second-order PLL, solving directly for $F(z)$ results in a fourth-order expression, two orders higher than its continuous-time cousin.[¶] Rather, we specify a second-order loop filter

$$F_3(z) = \frac{h_0 + h_1 z^{-1} + h_2 z^{-2}}{(1 - z^{-1})^2} \ . \tag{3.21}$$

Then $H_3(z)$ is given by

$$\begin{aligned} H_3(z) &= \frac{K_d F_3(z) \cdot \left(\frac{K_o z^{-1}}{1 - z^{-1}}\right)}{1 + K_d F_3(z) \cdot \left(\frac{K_o z^{-1}}{1 - z^{-1}}\right)} \\ &= \frac{K_d K_o \left(h_0 z^{-1} + h_1 z^{-2} + h_2 z^{-3}\right)}{1 + \left(K_d K_o h_0 - 3\right) z^{-1} + \left(K_d K_o h_1 + 3\right) z^{-2} + \left(K_d K_o h_2 - 1\right) z^{-3}} \ . \end{aligned} \tag{3.22}$$

Note that, as with the second-order model, $H_3(z)$ cannot in general be made to equal the $H(z)$ of (3.20). Instead, we simply equate the denominators of (3.20) and (3.22) and find the forward coefficients of the loop filter to be

$$h_0 = \frac{1}{K_d K_o}\left(\frac{c_1}{c_0} + 3\right) \ , \quad h_1 = \frac{1}{K_d K_o}\left(\frac{c_2}{c_0} - 3\right) \text{ and } \quad h_2 = \frac{1}{K_d K_o}\left(\frac{c_3}{c_0} + 1\right) \tag{3.23}$$

where the c_is are defined in 3.20. This completes the design of the discrete-time third-order PLL.

The second and third-order PLLs may now be accurately modeled and simulated on a digital computer, as well as implemented in real-time using commercially available integrated circuits (ICs) or using software generated for a digital signal processor (DSP). The motivations for completely digital and/or software implemented PLLs are manifold. One advantage is the elimination of device parasitics, which cause unintended poles in the transfer functions of PLLs with analog loop filters. Another advantage is the ability within a digital filter to actually have a pole, or poles, at DC, providing a loop filter with an open-loop gain of infinity. This is only approximated with the analog filter of Figure 3.3. Finally, we maintain that it is actually simpler to build a PLL using fully digital components or in software, which matches the performance of the canonical *analog* PLL described in section 3.2, than it is to build one using completely analog components. Digital components give the designer much more precise control. An important next step to this research is to examine the performance of these derived discrete-time models. Do they, indeed, give the performance we expect? Before this all-important question is addressed, however, performance measures for these PLLs must be established.

[¶]Direct solution for this fourth-order filter has been observed in this research to cause instability due to machine precision effects. This is yet another motivation to constrain the poles to lie precisely at DC.

3.4 Performance Measures for PLLs

Any synchronization structure employing the PLL operates in one of two modes: 1) acquisition mode or 2) tracking mode. With each of these modes, we wish to specify a set of performance measures that will aid in the design of the loop components for a specific application. In acquisition mode, the most important measure is acquistion time, t_{acq}, how long it takes for the error signal, $e(t)$, or, in the presence of severe noise, some short term averaged function thereof, to settle below some predefined limit. The parameter t_{acq} turns out to be a random variable that can be characterized by some probability distribution function, $\Pr[t_{acq} < t]$. This is an extremely important question, but unfortunately no theory exists to predict this function [49]. Some experimental results, however, can be obtained and will be reported in following sections. Intuition relating acquisition time to loop parameters will also be emphasized.

In tracking mode of operation, the most important questions involve the reliability and accuracy of the reconstructed phase, $\hat{\theta}$. We are interested in the susceptibility of the loop to temporarily loose lock. This phenomenon is known as *cycle slipping*. In addition, we would like to know how the loop operates in a variety of signal environments. Specifically, we examine the transient error response seen in $e(t)$ due to a phase step, a phase ramp (frequency step), and a frequency ramp. Finally, we would like to know if (and how) the variance of $\hat{\theta}$, denoted *output phase jitter*, can be related to the input signal to noise ratio (SNR) and the loop design parameters. We answer this last question first since it gives rise to the very important notion of *loop noise bandwidth*.

3.4.1 Loop Noise Bandwidth

What is the effect of noise at the input of a PLL on the steady-state phase estimate available at feedback? To answer this all-important question, it is convenient to define the notion of loop bandwidth, B_L.* Considering once again the simple model of Figure 1.2, we have as one input to the multiplier, a sinusoidal signal of interest and bandpass Gaussian noise,

$$s(t) = \sqrt{2P} \cdot \cos\left(2\pi f_c t + \theta(t)\right) + n(t) \tag{3.24}$$

and a pure reference signal,

$$v(t) = -V_o \sin\left(2\pi f_c t + \hat{\theta}(t)\right) \ . \tag{3.25}$$

*This derivation parallels Gardner's in[6]. His sign and phase conventions, however, differ slightly from those presented here.

It is permissible and convenient to express the stationary, bandpass noise as

$$n(t) = n_d(t)\cos(2\pi f_c t) - n_q(t)\sin(2\pi f_c t) \ . \tag{3.26}$$

Assume that n_d and n_q are independent, identically distributed processes. In a manner completely analogous to (3.3) and (3.4), we may write the multiplier output as

$$e(t) = \sqrt{\frac{P}{2}}V_o \sin\left(\theta(t) - \hat{\theta}(t)\right) + \frac{V_o n_q(t)}{2}\cos\hat{\theta}(t) - \frac{V_o n_d(t)}{2}\sin\hat{\theta}(t) \ . \tag{3.27}$$

Define detector gain as $K_d = \sqrt{P/2}\, V_o$ and now, for notational convenience, assume an implicit dependence on time for e, θ, $\hat{\theta}$, n_d, and n_q. Thus, we may express the error as

$$e = K_d \cdot \left[\sin\left(\theta - \hat{\theta}\right) + \frac{n_q}{\sqrt{2P}}\cos\hat{\theta} - \frac{n_d}{\sqrt{2P}}\sin\hat{\theta}\right] \ . \tag{3.28}$$

An additive noise equivalent for the linearized phase domain model of Figure 3.2 may now be given by

$$n' = \frac{n_q}{\sqrt{2P}}\cos\hat{\theta} - \frac{n_d}{\sqrt{2P}}\sin\hat{\theta} \tag{3.29}$$

which can be included in the summer. Thus,

$$e = K_d \cdot \left[\sin\left(\theta - \hat{\theta}\right) + n'\right] \tag{3.30}$$

where e is now considered a superposition of a *signal* term, $K_d \sin(\theta - \hat{\theta})$, and a *noise* term, $K_d n'$.

It can be assumed that, after some, heretofore unspecified, transient behavior, that a steady-state will be reached in which $\hat{\theta}$ will have a constant mean. Moreover, we assume that n' is zero mean. The variance of n' may thus be given by

$$\sigma_{n'}^2 = \frac{1}{2P}\left(\overline{n_q^2}\cos^2\hat{\theta} + \overline{n_d^2}\sin^2\hat{\theta} - 2\overline{n_q n_d}\sin\hat{\theta}\cos\hat{\theta}\right) \tag{3.31}$$

where the overbar is the time averaging operator. Note that $\overline{n_q^2} = \overline{n_d^2} = \overline{n^2} = \sigma_n^2$, $\overline{n_q n_d} = 0$, and $\cos^2\hat{\theta} + \sin^2\hat{\theta} = 1$. Thus [†],

$$\sigma_{n'}^2 = \frac{\sigma_n^2}{2P} \ . \tag{3.32}$$

The power spectral density of n' is shown in [6] to be

$$\Phi_{n'}(f) = \frac{1}{2P}\left[\Phi_n(f_c - f) + \Phi_n(f_c + f)\right] \tag{3.33}$$

[†]Here, we are making an assumption that $\hat{\theta}$ is independent of n_d and n_q, which in general is clearly not true. This assumption is used, however, in all known treatments and is justified in [6] for the (common) situation wherein $B_L \ll B_i$.

where $\Phi_n(f)$ is the original single-sided spectral density of the bandpass noise. For the special case of white noise where $\Phi_n(f) = N_o$, the spectrum becomes

$$\Phi_{n'}(f) = \frac{N_o}{P} \tag{3.34}$$

where N_o is the single-sided noise spectral density in [W/Hz]. The variance of the output phase estimate due to additive noise may thus be calculated using (3.33),

$$\overline{\hat{\theta}_n^2} = \int_0^\infty \Phi_{n'}(f)|H(j\omega)|^2 df \quad [\text{rad}^2] \tag{3.35}$$

which, in general, may or may not be tractable. Given white noise, however, this integral reduces to

$$\begin{aligned} \overline{\hat{\theta}_n^2} &= \frac{N_o}{P}\int_0^\infty |H(j\omega)|^2 df \quad [\text{rad}^2] \\ &= \frac{1}{\text{SNR}_i B_i}\int_0^\infty |H(j\omega)|^2 df \quad [\text{rad}^2] \end{aligned} \tag{3.36}$$

where $\omega = 2\pi f$, SNR_i is the input SNR, and B_i is the noise bandwidth of the signal applied to the phase detector [‡]. This allows a convenient definition of *noise bandwidth* for the loop as

$$B_L = \int_0^\infty |H(j\omega)|^2 df \quad [\text{Hz}] \implies \overline{\hat{\theta}_n^2} = \frac{N_o B_L}{P} = \frac{B_L}{\text{SNR}_i B_i}[\text{rad}^2]\,. \tag{3.37}$$

For the canonical, second-order PLL defined in (3.9), this bandwidth can be shown to equal

$$B_{L,2} = \frac{1}{2}\,\omega_n\left(\zeta + \frac{1}{4\zeta}\right) \tag{3.38}$$

which, with $\zeta = \dfrac{1}{\sqrt{2}}$, implies $B_{L,2} = \omega_n \frac{3\sqrt{2}}{8}$. This value of B_L is used to give the theoretical values of phase variance plotted as the lines in Figure 3.13. For the third-order PLL defined by (3.11), this noise bandwidth is given by

$$B_{L,3} = \frac{1}{4}\,K_o K_d \frac{a_2 K_o K_d + a_2^2 - a_3}{a_2 K_o K_d - a_3} \tag{3.39}$$

which, when we define the parameters as in (3.12), simplifies to $B_{L,3} = \dfrac{6}{5}\omega_3$. This value of B_L is that from which the theoretical values of phase variance for third-order PLL plotted as the lines in Figure 3.14.

Loop bandwidth for the canonical second-order loop is shown in Figure 3.5, normalized to the choice of ω_n as a function of ζ. Note that it is a minimum at $\zeta = 0.5$ but also that it is nearly minimum in a fairly broad range around 0.5. It turns out that $\zeta = \frac{1}{\sqrt{2}} \approx 0.707$ will be optimal in terms of acquisition performance and is thus the value most often used in

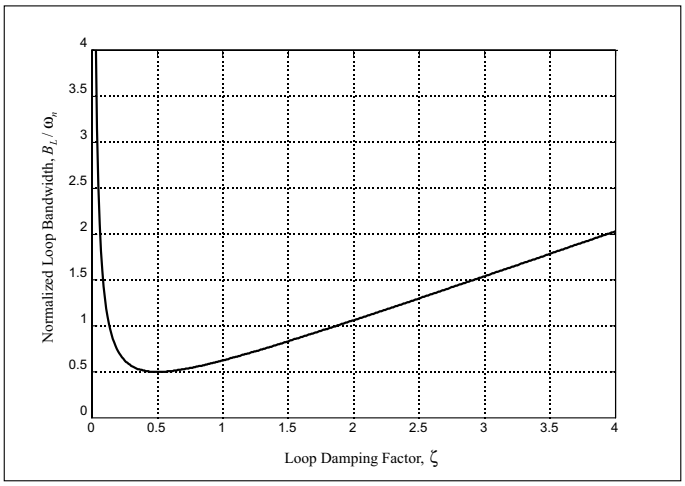

Figure 3.5: Normalized loop bandwidth, $B_L\omega_n$ plotted as a funtion of ζ, for canonical second-order loop, $H(s)$

practice. This corresponds to the *critically damped* state of the loop according to classical control theory.

Given an expression for loop bandwidth, it follows that we may define the notion of loop signal-to-noise ratio, SNR_L.[§] The phase jitter of the input signal may be defined by

$$\overline{\theta_n^2} = \frac{1}{2\text{SNR}_i} \quad [\text{rad}^2] \tag{3.40}$$

because $\frac{1}{2}$ of the noise power is orthogonal to the signal phase. By analogy then, we define a relationship between output phase jitter and loop SNR by

$$\overline{\hat{\theta_n}^2} = \frac{1}{2\text{SNR}_L} \quad [\text{rad}^2]. \tag{3.41}$$

Using (3.37), we define

$$\text{SNR}_L = \frac{\text{SNR}_i B_i}{2B_L} \tag{3.42}$$

where SNR_i and B_i are as defined in (3.36), and B_L is defined by (3.37). Thus, a notion of "gain" may be attributed to the PLL as $10\log_{10}(B_i/B_L) - 3$ [dB]. The PLL "cleans up" the input signal by this amount in providing a locally generated reference. Note that B_L could be made arbitrarily low to allow the PLL to function in an arbitrarily low SNR

[‡]For all simulations presented in this work, B_i is taken to be the sample rate, F_s, or, in the case of digital signalling with matched filters, the baud rate, R_b.

[§]There is actually no "signal" in the PLL. This definition is ultimately arbitrary and simply a helpful measure. Note that the definition in (3.42) is consistent with that used in [6] but is 3 dB lower than the SNR_L expression used in [5], [9], and [36].

environment. Doing so, however, is at the risk of a potentially *long* acquisition period that will be discussed in section 3.4.4.

3.4.2 Transient Responses

We examine the transient behavior of the phase-locked loop for three different inputs: 1) a phase step, 2) a phase ramp or equivalently, a frequency step, and 3) a frequency ramp. The attempt is to give a qualitative, versus quantitative, view of loop performance. Note that these transient behaviors are applicable to the tracking behavior of the PLL whenever these inputs are encountered after the PLL has reached a steady-state. In other words, the PLL will essentially re-acquire phase-lock with the measures of performance given. For brevity, we devote primary coverage to the transient performance of the second-order loop. All of the transient responses shown are simulation results for $H_2(z)$, defined by (3.18) with parameters defined by (3.19). Theoretical results in zero noise are available in [6] to which the following experimental examples match well. For the sake of brevity we choose not to present these complicated results and refer the interested reader to this excellent reference for these expressions.

Figure 3.6 shows transient results for $H_2(z)$ due to a phase step of $\pi/2$ radians, in the absense of noise, for a variety of loop damping factors. Time is normalized with ω_n to provide a generalized view of the effect of ζ as a parameter. In part A, the phase error term, $\sin\phi = \sin(\theta - \hat{\theta})$ where the $\sin(\cdot)$ functions disappear at steady-state. Note that the error oscillates for low ζ. For high ζ, the appearance of fast convergence is deceiving since the error decays very slowly. The curve corresponding to $\zeta = 1/\sqrt{2}$ converges fastest to zero steady-state error. After convergence, the first, second, and third-order PLLs all operate with zero steady-state error in the presence of no noise.

Figure 3.6(B) shows the output phase estimate (denoted ϕ_o instead of the usual $\hat{\theta}$). The behavior is very similar to that of the phase error except that here the values converge to the actual phase value, $\pi/2$.

Figures 3.7(A) and 3.7(B) show the error response of the second-order loop due to frequency steps of ω_n and $2\omega_n$ radians respectively. In both cases, once again $\zeta = 1/\sqrt{2}$ proves to be optimal in the sense of forcing the steady-state error to zero quickly. For frequency steps larger than these examined, we would begin to observe a number of sinusoidal oscillations during the transient response before the convergence behavior. The length of this acquisition period is described in section 3.4.4. Note that the steady-state output phase in this situation would not converge to a single value but rather to a ramp of slope equal to the frequency offset.

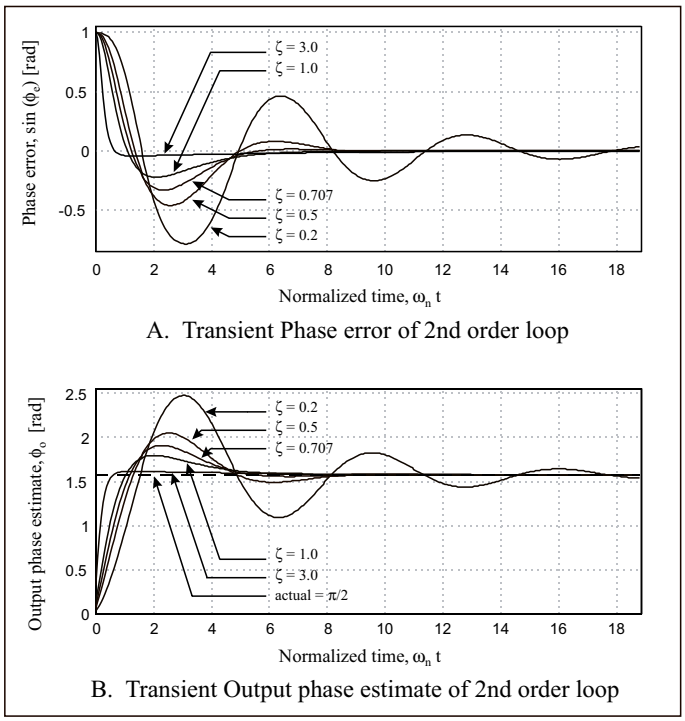

Figure 3.6: Transient responses of 2nd-order PLL for various values of ζ due to phase step input of $\pi/2$ radians

The first-order PLL is not capable of responding to a frequency step with non-zero steady-state error. The error will instead converge to a finite value. The canonical second-order loop, i.e., one built with a loop filter with infinite DC gain, can track with zero error as is shown. Second-order loop configurations built without an infinite DC gain loop filter perform more like a first-order loop with finite steady-state error. This characteristic defends our assertion in section 3.2 that this type of second-order loop is actually better described as a modified first-order loop. The third-order PLL, like the second-order canonical loop, tracks a frequency step with zero error.

In Figure 3.8, we show the response of $H_2(z)$ to a frequency ramp of magnitude $\Delta\dot{\omega}$ [rad/s^2]. This would correspond to a constant acceleration in doppler for mobile or satellite communications. Note that the error does not now go to zero in steady-state, but rather to a constant, $\Delta\dot{\omega}/\omega_n^2$. This value is, however, fairly small for reasonable system parameters and for practical ramps that might be encountered in terrestrial wireless or satellite communications. Therefore, the second-order loop is not disqualified from consideration for the purpose of carrier recovery. The first-order PLL cannot keep up with a phase acceleration

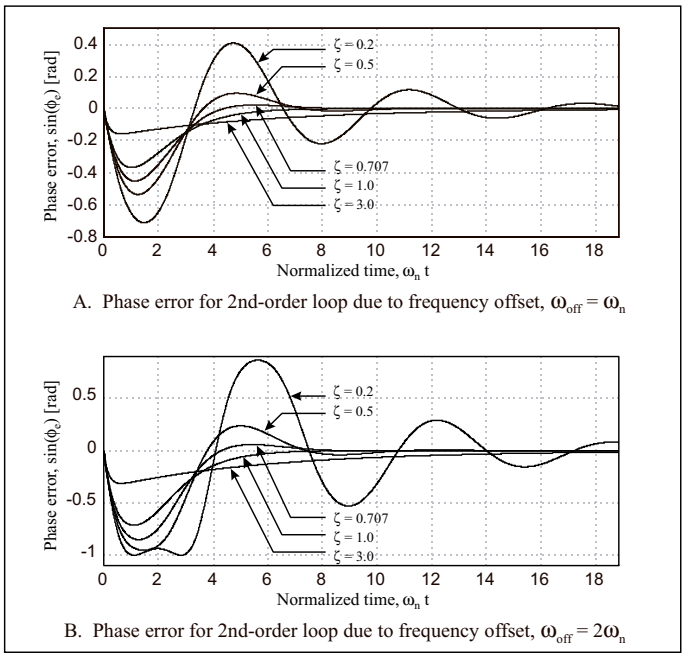

Figure 3.7: Transient responses of 2nd-order PLL for various values of ζ due to frequency step input: (A) Frequency step, $\omega_{off} = \omega_n$; (B) Frequency step, $\omega_{off} = 2\omega_n$

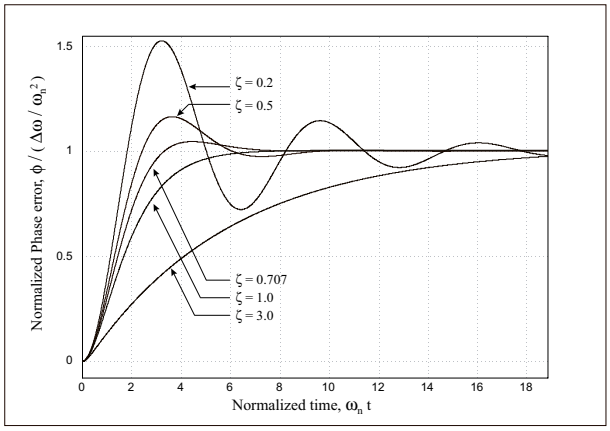

Figure 3.8: Transient responses of 2nd-order PLL for various values of ζ due to frequency ramp input (time normalized with ω_n; error normalized with $\omega_n^2/\Delta\dot{\omega}$)

such as this and its steady-state error approaches infinity. For zero steady-state error, the third-order PLL is required.

3.4.3 Cycle Slipping

In some operating conditions, instantaneous noise spikes can cause the PLL to temporarily loose lock. Figure 3.9 shows an example of this phenomena where the output phase estimate, $\hat{\theta}$, is plotted as a function of normalized time. The input signal to noise ratio in this example, SNR_i, is set to -8 dB. Loop bandwidth, B_L is set to approximately 10 times the input bandwidth, B_i, yielding a PLL gain of about 10 dB. Loop SNR is thus given by $\mathrm{SNR}_L \approx 2$ dB. In this region of SNR_L, cycle slipping becomes an important attribute of PLL operation. The actual value of the phase, θ, being tracked is $\pi/2$. Note that the PLL quickly acquires the phase, but after some time, noise dislodges this steady-state condition. The PLL subsequently re-acquires to various multiples of $2\pi + \pi/2$, and this behavior continues randomly over time.

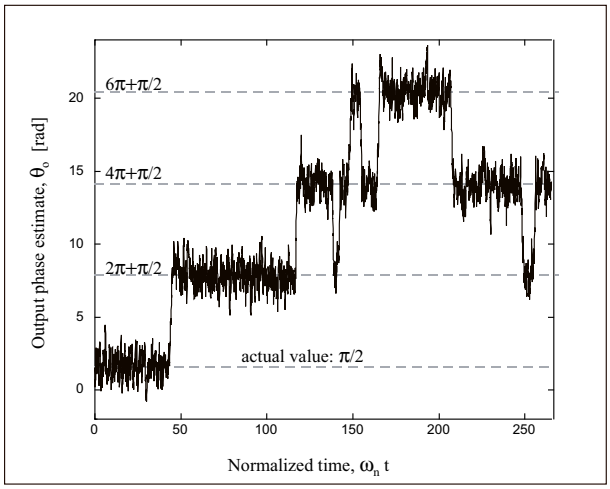

Figure 3.9: Example of cycle slipping (input SNR = -8 dB, $B_i/B_L \approx 10$)

Viterbi [9], using Fokker-Planck equations, was able to derive a theoretical value for the average time between cycle slips, T_{AV}, for a first-order PLL, viz.,

$$T_{AV} = \frac{\pi^2 \, \mathrm{SNR}_L \, I_o^2 \, (\mathrm{SNR}_L)}{2B_L} \tag{3.43}$$

where SNR_L is expressed in linear form, and $I_o(x)$ is the zeroth-order modified Bessel function of the first kind. For reasonably high SNR_L, this expression may be approximated

by

$$T_{AV} \approx \frac{\pi}{4B_L} \exp\left(2\mathrm{SNR}_L\right) \ . \tag{3.44}$$

This expression does not take into account the fact that cycle slips may cluster however.

It is sufficient to note that for values of $SNR_L > 10$ dB, which are of interest for carrier recovery in PSK modulation schemes, the predicted values of T_{AV} are quite high. Note once again that B_L can be made arbitrarily small to control cycle slipping if necessary.

3.4.4 Acquisition Time

The aquisition process of a phase-locked loop is an inherently non-linear one. No simplifying linear approximations can hold. Therefore, as noted above, no present exact theory exists to predict the probability distribution of acquisition time, t_{acq}, in the presence of noise. We therefore appeal to simulation results to give an intuitive notion of the acquisition behavior of the PLL.

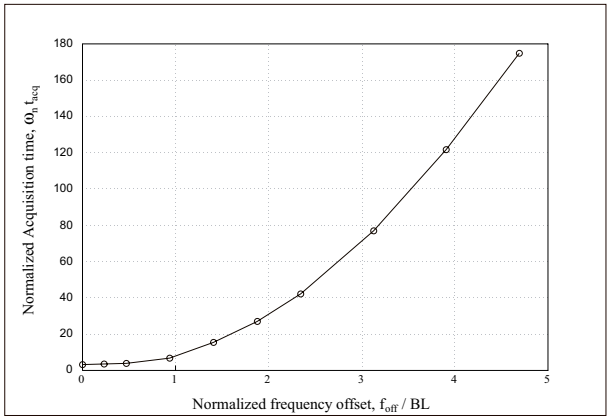

Figure 3.10: Acquisition time for 2nd-order PLL for various values of initial frequency offset ($\zeta = 2^{-\frac{1}{2}}$)

Figure 3.10 shows the time, normalized to loop natural frequency ω_n, for the phase error out of the detector to reduce to less than 15^o, given an initial frequency offset, which is normalized to loop bandwidth, B_L. Note that the choice of 15^o as a measure of acquisition is completely arbitrary and serves only as a basis for comparison. In short, for frequency offsets less than than B_L, the loop converges quite quickly. As the offset increases, however, the acquisition time rises exponentially. A narrow loop bandwidth is desirable for noise immunity, but clearly it cannot be arbitrarily narrow if *reasonable* acquisition time is a necessity. The exponential behavior of acquisition time in the presence of the frequency

offset serves to motivate the discussion of AFC-aided acquisition in Chapter 5.

3.5 Performance of Derived Discrete-time Models

We wish to briefly show simulation results that validate the discrete-time models developed in section 3.3 before moving on to address the topic of PLL optimality in section 3.6. This is accomplished by 1) comparing the frequency responses of the derived loops to those of the canonical models defined by (3.9) and (3.12); and 2) comparing the phase jitter performance of the derived models to that of the canonical models, the theoretical values of which were developed in section 3.4.

Remember that in section 3.3 we proposed discrete-time second and third-order PLLs, (3.18) and (3.22), which did not identically match the transfer functions, (3.14) and (3.20), derived from the BZT of the canonical continuous-time models. The fundamental difference between the models proposed and those predicted by an exact solution is the lack of a single zero at $z = -1$ in the proposed models. Figures 3.11 and 3.12 show the frequency responses of the proposed second and third-order models versus exact solutions respectively. In each case, two corner frequency values, ω_n or ω_3, are shown. Clearly the lack of a high frequency zero does change the shape of the frequency response. Nevertheless, the change is only noticable for the very high frequency values, approaching $\frac{1}{2}F_s$. Note also that the differences between ideal $H(z)$s and the suggested $H_2(z)$ and $H_3(z)$ are less critical as the corner frequencies become smaller, i.e., move farther away from $\frac{1}{2}F_s$. Since the corner frequency is *usually* chosen to be relatively small compared to the sample rate, F_s, we therefore recommend these PLLs for general use with the caveat that in extremely wide loop bandwidth conditions, the proposed loops may not perform as well as expected in the area of noise immunity.

Figures 3.13 and 3.14 show the performance of the second and third-order PLL models derived in section 3.3 in the important measure of steady-state variance of the phase estimate, $\hat{\theta}$. In both cases, the theoretical lines are simply plots of (3.37) with B_L given by equations (3.38) and (3.39) respectively. As can be seen in Figure 3.13, the proposed second-order model almost perfectly matches theory. The match is somewhat less than perfect for the third-order model in 3.14 where the approximate model of (3.22) actually performs better than theory. It is unclear exactly why this is so but nevertheless shows that the performance of the derived third-order loop is approximately consistent with theory and moreover, is consistent with itself for a wide variety of input SNRs.

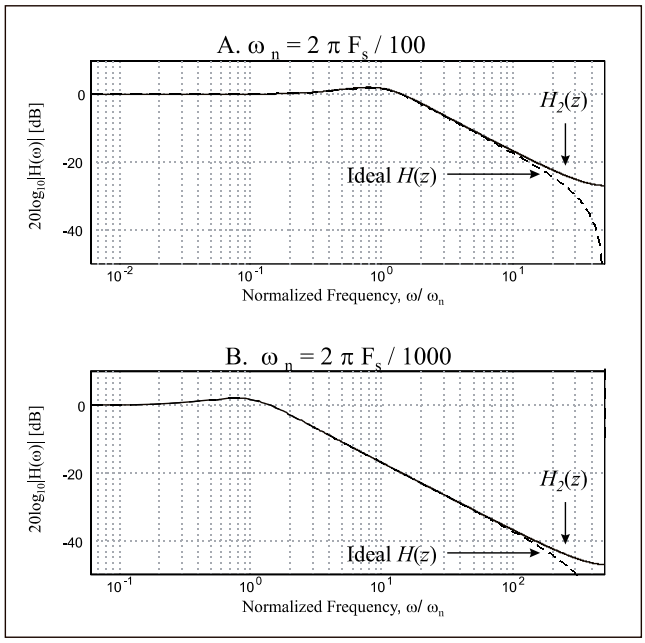

Figure 3.11: Frequency responses of second-order, discrete-time PLLs expressed in equations (3.14) and (3.18) for two choices of ω_n ($\zeta = 2^{-\frac{1}{2}}$)

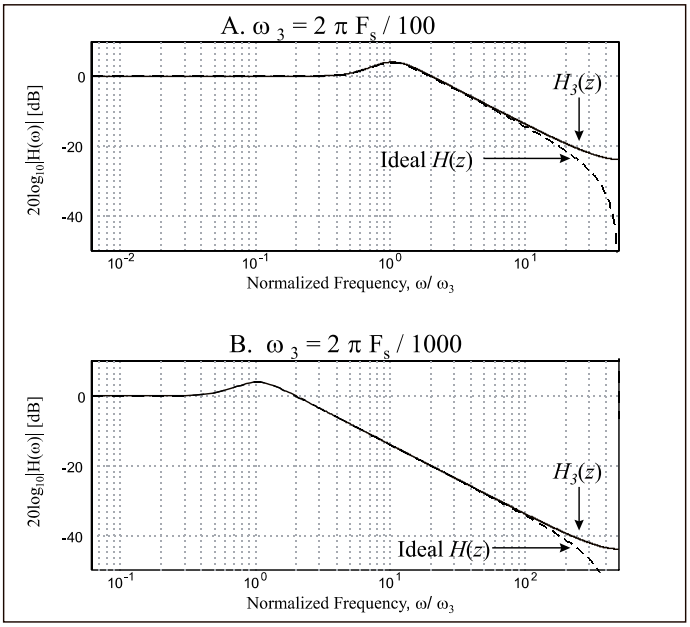

Figure 3.12: Frequency responses of third-order, discrete-time PLLs expressed in equations (3.20) and (3.22) for two choices of ω_3

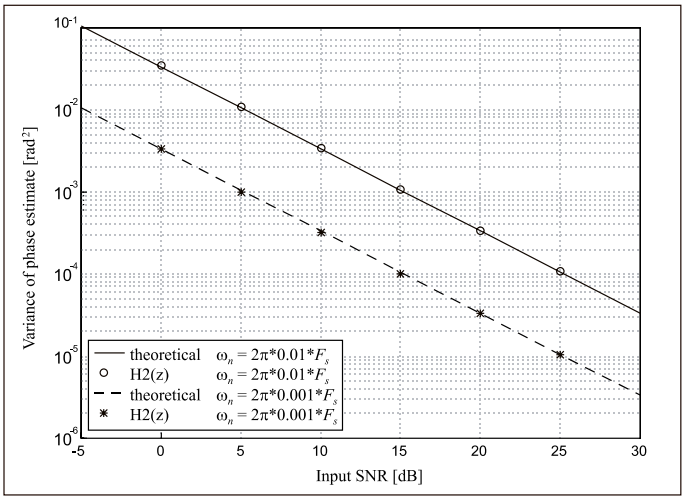

Figure 3.13: Phase output variance (jitter) of derived discrete-time 2nd-order PLL, versus theoretical values, for two values of ω_n

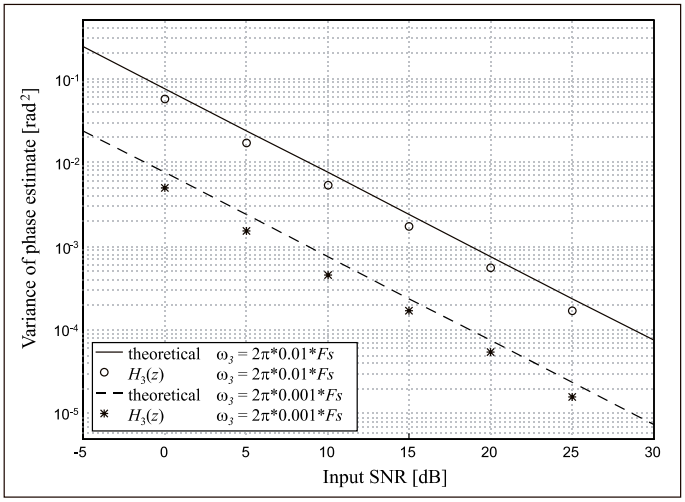

Figure 3.14: Phase output variance (jitter) of derived discrete-time 3rd-order PLL, versus theoretical values, for two values of ω_3

3.6 The Notion of Optimality for a PLL

Loop bandwidth represents the fundamental tradeoff in the design of a PLL. We wish to

1. reduce the output phase jitter due to external noise by making B_L as small as possible, and
2. reduce the acquisition time and transient errors by making B_L as large as possible.

Obviously, we cannot have it both ways. For any particular application, we wish to have some combination of the above two functions, which would make the performance of the PLL "optimal" in some sense.[¶] Optimality has been defined in the mean square sense for an input signal in Gaussian noise by minimizing

$$\Sigma^2 = \overline{\hat{\theta}_n^2} + \lambda^2 E_T^2 \tag{3.45}$$

where $\hat{\theta}_n$ is as defined in (3.37) and E_T^2 is a measure of the total transient error, viz.,

$$E_T^2 = \int_0^\infty e^2(t)dt \; . \tag{3.46}$$

Note that $e(t)$ is as defined in (3.30), and λ is a Lagrangian multiplier used to establish the relative weighting of the transient error. Table 3.1 shows optimal loops for three different input signals in AWGN. The Wiener optimization also specifies the optimal choice of loop natural frequency as a function of input power to noise spectral density ratio, which is related to input SNR by $P/N_o = \mathrm{SNR}_i B_i$, where B_i is the baseband equivalent noise bandwidth.

The canonical second-order loop described by (3.9) with damping factor $\zeta = 1/\sqrt{2}$ is optimal for a frequency step. A frequency offset at loop start up is an important example of a frequency step. This justifies the attention thus far on the second-order loop. The first-order loop while optimal for a phase step shows poor tracking capability for a frequency offset. For this reason, the first-order PLL is virtually ignored in this research. The third-order loop is optimal for a frequency ramp (or "chirp") signal. This is very important in some applications and is of significant interest in mobile communications when a changing doppler frequency might be expected.

The choice of a particular order of PLL can be based on the particular type of signal to which we wish to synchronize. The parameters for the loop may be chosen based on the signal environment in which the loop must operate. In this sense, there are infinitely many

[¶]This brief discussion follows mainly from [6].

Table 3.1: Optimum PLLs for three input signals in AWGN

Input Signal	**Optimum Loop,** $H(s)$	**Optimum Bandwidth**
Phase step: $\theta(t) = \Delta\theta$	$\dfrac{\omega_1}{s+\omega_1}$	$\omega_1 = \Delta\theta\lambda\sqrt{\dfrac{P}{N_o}}$
Frequency step: $\theta(t) = \Delta\omega t$	$\dfrac{\omega_n^2 + \sqrt{2}\omega_n s}{\omega_n^2 + \sqrt{2}\omega_n s + s^2}$	$\omega_n^2 = \Delta\omega\lambda\sqrt{\dfrac{P}{N_o}}$
Frequency ramp: $\theta(t) = \dfrac{\Delta\dot{\omega}t^2}{2}$	$\dfrac{\omega_3^3 + 2\omega_3^2 s + 2\omega_3 s^2}{\omega_3^3 + 2\omega_3^2 s + 2\omega_3 s^2 + s^3}$	$\omega_3^3 = \Delta\dot{\omega}\lambda\sqrt{\dfrac{P}{N_o}}$

Adapted from [6].

optimal loops for infinitely many different applications. Finally, Gardner points out in [6] that an extremum for a PLL tends to be quite broad, which means that there are many values of loop parameters (ζ and ω_n in the second-order loop) that give nearly optimum performance. Given a basic understanding of loop behavior, these nearly optimum solutions may often be found simply by trial and error.

3.7 Chapter Summary

In this chapter, we have endeavored to provide a cursory introduction to phase-lock loop. Special attention has been given to second and third-order PLLs, which are of particular interest here in their application to suppressed-carrier recovery. We began with a continuous-time model, in which linearization and the application of the Laplace transform helped us to understand the behavior of this feedback control loop and aided in the development of canonical equations with intuitively satisfying parameters.

In section 3.3, we applied the BZT to these canonical equations to come up with discrete-time models suitable for implementation with digital components or in software on a DSP or digital computer. The important point in these derivations was that we preserved the classical parameters, ζ, ω_n, and ω_3, which were developed many years ago for analog circuits.

Use of these parameters will hopefully serve as an aid to the digital designer, allowing, at least in first-cut design, rapid development of digital PLLs that closely approximate the classical continuous-time models.

We devoted significant attention in section 3.4 to defining and describing a variety of performance measures for PLLs. Where they exist, theoretical expressions for these measures were stated or referred. The most important measure was steady-state phase jitter, defined as the steady-state variance of the output phase estimate. This led to the definition of loop bandwidth, B_L, for a PLL.

Note again that in PLL design there is a fundamental tradeoff between acquistion time and phase jitter. Large B_L enables rapid acquisition time and thus small transient error but allows large phase jitter, which in the more extreme cases can lead more deleterious effects such as cycle slipping. Narrowing B_L, on the other hand, can lead to exponentially increasing acquisition time and thus large transient errors but can arbitrarily reduce steady-state phase jitter. The tradeoff between these transient versus steady-state error has been examined under the Wiener optimization criterion given in (3.45) to which we devoted only cursory discussion in section 3.6.

We now seek in the following chapters to apply what was learned in this chapter to the task of recovering a suppressed-carrier in digitally phase modulated signal formats. As will be shown, the basic PLL structure is at the core of all closed-loop carrier recovery schemes. Moreover, the performance of both the closed-loop and open-loop schemes presented in Chapter 4 will be shown to bear striking resemblance to those expressions given in this chapter.

Chapter 4

Coherent Carrier Recovery Structures

The fact that the PLL exhibits a transient response given a phase step input makes it an unlikely candidate for carrier recovery of digitally phase modulated signal formats. In fact, the PLL is not generally useful for carrier recovery when the signal of interest has phase discontinuities like those found in PSK. The foregoing coverage of the PLL in Chapter 3 has not been in vain, however. All closed-loop carrier recovery schemes for PSK modulation are based on the same principle as the PLL but simply add a mechanism to remove the modulation. As will be shown, this removal is done either by decision feedback (remodulation) or by an Mth-order nonlinearity, which provides a discrete spectral line* for the PLL to track. The Costas and squaring loops, outlined in section 4.1, each perform this task with theoretically equivalent performance. Each is an extension of the PLL to closed-loop carrier tracking schemes. Open loop schemes operate on the principle of modulation removal, as well. These, however, use feedforward estimation techniques to remove phase and frequency errors. We provide a simple overview of open-loop techniques applicable to the task of carrier recovery in section 4.2. Finally, we conclude the discussion of carrier recovery structures with an exposition of the concept of automatic frequency control (AFC), presented in Chapter 5 as an acquistion aid to phase-coherent techniques.

*In the case of the Costas loop, the discrete spectral line might be said to be from a "phantom" carrier since the discrete spectral line is around 0 Hz.

4.1 Closed-Loop Carrier Recovery Structures

4.1.1 Costas Loop

The Costas loop is by far the most common implementation of closed-loop carrier recovery and as will be shown, provides not only a convenient mechanism for suppressed-carrier tracking but also fully demodulates the received signal. We therefore use the terms, "Costas loop" and "Costas demodulator," interchangably throughout the discussion.

Consider the classical Costas loop structure shown in Figure 4.1 where $s(t) = \sqrt{2P}$ $d(t)\cos(2\pi f_c t + \theta)$ and $d(t) \in \{-1, +1\}$ denotes the transmitted binary signal at time, t. The Q-arm, taken by itself, provides a PLL-like control signal except for the modulation by $d(t)$. After low pass filtering

$$q(t) = \sqrt{\frac{P}{2}}\, d(t)\ \sin\left(\theta - \hat{\theta}\right) \tag{4.1}$$

where, following our previous conventions, θ is the carrier phase in the SOI and $\hat{\theta}$ is the output phase estimate from the loop. Note that the fundamental goal of suppressed-carrier recovery is to provide some mechanism for removing $d(t)$ from a control signal like (4.1). The I-arm control signal is found to be

$$i(t) = \sqrt{\frac{P}{2}}\, d(t)\ \cos\left(\theta - \hat{\theta}\right)\ . \tag{4.2}$$

Note that the arm LPFs will usually be designed with a cutoff around the baud rate if data demodulation is desired. Multiplying (4.1) and (4.2), the error control signal is

$$e(t) = \frac{P}{2}\, d^2(t)\ \sin\left(\theta - \hat{\theta}\right)\cos\left(\theta - \hat{\theta}\right)\ =\ \frac{P}{4}\ \sin(2\phi) \tag{4.3}$$

where $\phi = \theta - \hat{\theta}$ denotes the phase difference between input and reference carriers and $d^2(t)$ $= 1$. Thus we have removed the modulation via squaring the received signal and provided a PLL-like error signal in $e(t)$. For $e(t)$ small, the linearizing approximation, $\sin(2\phi) \approx 2\phi$, can be made and most of our intuition for PLLs can be applied to the Costas loop. Note also that the I-arm signal at steady-state, $2\phi \ll 1$ implying $\cos(2\phi) \approx 1$. This means that $i(t)$ will be proportional to the data signal, $d(t)$, (with additive noise) and will be used for the receiver decision metric.

4.1.2 Squaring Loop

The Costas loop can be shown to have the same noise performance as the *squaring loop* shown in Figure 4.2, and its functionality is simpler to observe. After bandpass filtering for

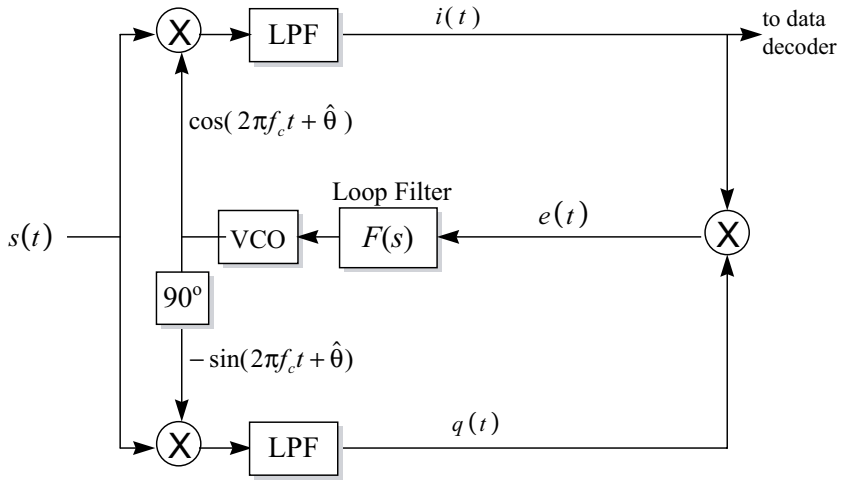

Figure 4.1: Basic structure of analog Costas demodulator

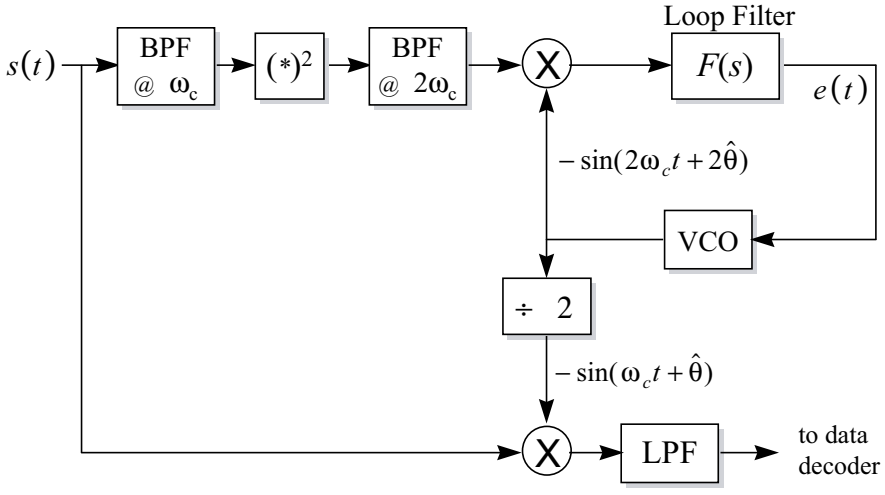

Figure 4.2: Squaring Loop

noise immunity, we apply a direct squaring operation on $s(t) = \sqrt{2P}\, d(t)\cos(\omega_c t + \theta)$.† We obtain at the double frequency,

$$P\, d^2(t)\sin\left(2\omega_c t + 2\theta\right) \quad .$$

Since $d^2(t) = 1$, a discrete spectral line appears at $2\omega_c$, which may be filtered by a bandpass filter (BPF) whose bandwidth need only range over the uncertainty of the value for $2\omega_c$. This is then applied to a PLL tuned to $2\omega_c$ which yields a phase estimate, $2\hat{\theta}$. The local reference may then be divided to provide $-\sin(\omega_c t + \hat{\theta})$ to downconvert $s(t)$ to baseband. Note that the multiplication and division operations have led to a 180^o phase ambiguity, analogous to taking the square root of a squared quantity. This is not a shortcoming of the squaring or Costas loops but a fundamental shortcoming in the detection of phase modulated signals with locally generated references. If purely coherent detection is required, then some means of removing this ambiguity, e.g., a training sequence, must be found. Another very common method is the use of differentially encoded data described in section 1.3.2.

The squaring loop structure may easily be extended to higher-order modulations. For M-ary PSK signal sets, the squarer can be replaced simply with an Mth-law device, and the divide-by-2 can be replaced by a divide-by-M circuit. Note, however, that an Mth-order phase ambiguity, i.e., $360^o/M$, is introduced.

4.1.3 Noise Performance

We would expect the Costas and squaring loops to have noise performance similar that of the PLL. This is true except for an added *squaring loss*, which comes from a noise analysis similar to that found in section 3.4.1. It is shown in [6] that the phase estimate of $2\hat{\theta}$ will have a steady-state variance due to additive white noise of

$$\begin{aligned}\overline{\left(2\hat{\theta}_n\right)^2} &= 4\left(\frac{N_o B_L}{P}\right)\left(1 + \frac{N_o B_i}{2P}\right) \quad [\text{rad}^2] \\ &= 4\left(\frac{B_L}{\text{SNR}_i B_i}\right)\left(1 + \frac{1}{2\text{SNR}_i}\right) \; [\text{rad}^2] \end{aligned} \tag{4.4}$$

where B_L is as defined in (3.37), B_i is the input equivalent noise bandwidth, and SNR_i is the input signal to noise power ratio. Squaring loss arises from the fact that, unlike the PLL, we perform a squaring operation on noise producing intermodulation products with non-zero variance.

†A square-law nonlinearity is used because its analysis proves to be tractable and is in no sense optimal. Other non-linearities can be used to provide better noise performance. The arctangent operation can in fact be shown to be optimal and is briefly discussed in section 4.1.6.

Table 4.1: Intermodulation losses in Mth-order phase synchronizers

M	Loss, $L_n(\mathrm{SNR}_i)$
1	1
2	$1+\frac{1}{2\mathrm{SNR}_i}$
3	$1+\frac{2}{\mathrm{SNR}_i}+\frac{2}{3\mathrm{SNR}_i^2}$
4	$1+\frac{9}{\mathrm{SNR}_i}+\frac{6}{\mathrm{SNR}_i^2}+\frac{3}{2\mathrm{SNR}_i^3}$

Adapted from [6].

The notion of squaring loss is actually a special case of intermodulation losses for Mth-order recovery loops. Reference [6] provides the following result for the generalized M-phase synchronizer:

$$\overline{\left(M\hat{\theta}_n\right)^2} = M^2 \left(\frac{N_o B_L}{P}\right) L_n\left(\mathrm{SNR}_i\right) \quad [\mathrm{rad}^2] \tag{4.5}$$

where $L_n\left(\mathrm{SNR}_i\right)$ is a loss defined as a function of input SNR in its linear representation. Table 4.1 shows the losses in carrier synchronizers for several PSK constellations.[‡] Note that for high input SNR, all such losses are negligible. At low SNR, however, the losses become very significant, and require a severe restriction on Costas loop bandwidth in order to provide sufficient loop SNR.

4.1.4 Discrete-Time Implementation

We can, however, improve the SNR seen by the recovery loop by using I&D filters as shown in the discrete-time structure of Figure 4.3. These filters could easily be taken to be filters matched to a pulse shape depending upon the application. We note that the sine and cosine of the phase difference, $\phi = \theta - \hat{\theta}$, can be averaged over baud periods in the quadrature arms of the digital receiver. This provides the Costas loop with sufficient information about $\sin(2\phi)$ to still acquire the carrier, although it is now operating at the baud rate, $R_b = 1/T_b$, rather than at the sample rate, F_s. We note here that in terms of absolute time, the acquisition process of the Costas loop is slower than a sample rate implementation. In

[‡]Although the result for $M = 3$ seems for the moment to be *purely* academic!

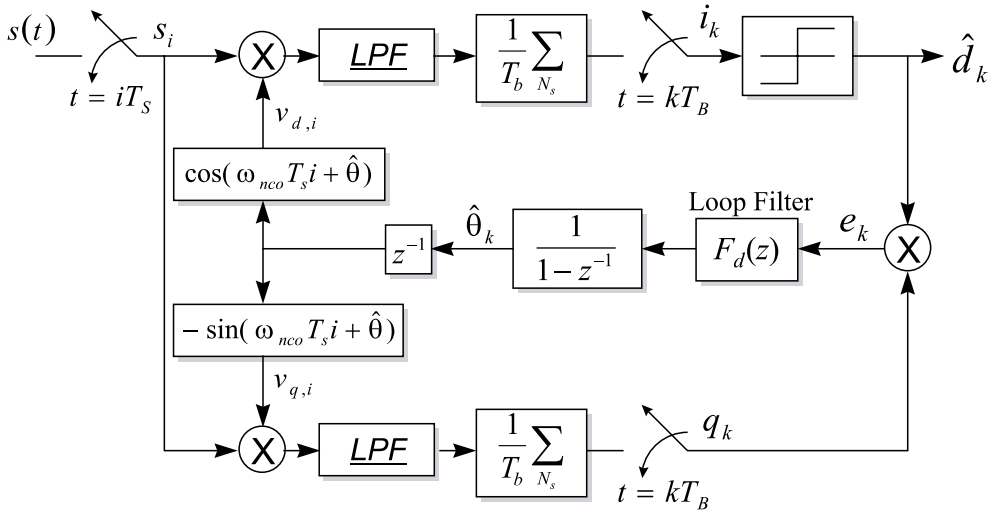

Figure 4.3: Block diagram of Costas demodulator, discrete-time implementation

terms of the number of samples, however, the bit rate implementation aquires more quickly in general. This baud rate implementation strategy can have tremendous reductions in required processing budget.

The integrate and dump (I&D) circuit can be replaced with a matched filter in the case of pulse shaping or baseband equalization. Similarly, in direct-sequence spread spectrum (DSSS) applications, it can be replaced with a matched filter or binary correlator for despreading. In the case of DSSS, the despreader becomes imperative for two reasons. First, input SNRs for spread spectrum are typically quite low. Typical values range from 0 to -50 dB in some applications. These are regimes where the performance of the Costas loop is marginal at best. Despreading in each of the quadrature arms allows a sufficiently high input SNR to be seen by the carrier recovery loop. Secondly, in the case of DSSS code division multiple access (CDMA), there are many interfering signals present in $s(t)$ that are at roughly equal powers to the SOI and at the same nominal carrier frequency. Without prior despreading, there would be no way to ensure that the Costas loop would track the correct carrier.

The structure of Figure 4.3 gives insight into a completely software-based downconversion process. The input signal, $s(t)$, is sampled, creating $\{s_i\}$, where we denote values obtained at the original sample rate with the subscript i and values sampled at the baud rate with subscript k. We then apply direct digital downconversion (DDC) by multiplying with the cosine and negative sine of the NCO output. Arm LPFs can be either finite or infinite impulse response, (FIR) or (IIR), digital filters with corner frequencies set to the

baud rate. These I&D filters can improve the SNR seen by carrier recovery loop by their averaging of the input noise processes.

Symbol timing is assumed and not explicitly shown in Figure 4.3. In fact, symbol or code timing is usually linked to the carrier recovery process in a "bootstrapping" manner, i.e., carrier recovery relies on bit timing and vice-versa. In practice, this means that rough symbol timing can be gained non-coherently; if the carrier offset is not too large, relative to the baud rate, then the phase difference, ϕ, while non-zero, is relatively constant over a baud period. This allows the quadrature I&D circuits to provide correlation information to the symbol timing processor, and a proper sampling time, kT, can be selected. Meanwhile, as i_k and q_k estimates improve, better phase information will be provided for the error control samples, e_k, allowing carrier recovery. This will in turn provide more robust symbol timing information and so on.

Hard limiting of the I-arm is commonly applied in practical Costas demodulators. This practice fundamentally changes how the Costas loop removes the modulation from the SOI. It essentially becomes a *decision feedback*, or *remodulation*, structure. This non-linearity adds to the complexity of the transient behavior of the loop, but in the steady-state where the phase error is expected to be small, it is easy to see why this is done. We wish to show that this practice, common for high SNRs ($\gg$ 0dB), fundamentally changes the steady-state stochastic performance of the Costas loop to that of the PLL.

The quadrature arm signal in (4.1) is quite similar to the error signal of a basic PLL except it is modulated with $d(t)$. In discrete-time, this signal may be expressed by

$$q_k = \sqrt{\frac{P}{2}}\, d_k\, \sin(\phi_k) \tag{4.6}$$

where $\phi_k = \theta_k - \hat{\theta}_k$, the phase error at time, $t = kT$. In the I-arm the sampled output is

$$i_k = \sqrt{\frac{P}{2}}\, d_k\, \cos(\phi_k)\,. \tag{4.7}$$

As ϕ_k becomes small, $i_k \propto d_k$. Hard limiting thus produces an estimate, $\hat{d}_k$, for the transmitted symbol. Except for bit errors then, $e_k = \text{Sgn}\,(i_k)q_k = \sqrt{\frac{P}{2}}\sin(\phi_k)$. Note that now, in this special case, the Costas loop error term, e_k is no longer proportional to 2ϕ but rather to ϕ. Therefore, when examining the variance (jitter) of the phase estimate, (4.4) no longer applies. Rather, this expression reduces to that of (3.37).

After the multiplication, the discrete-time Costas loop model operates in precisely the same fashion as the discrete-time PLL in Figure 3.4. The digital loop filter may be a direct form implementation of either (3.17) or (3.21), depending on the desired order of the

system. We now model the NCO as a simple accumulator with "gain" $K_o = 1$. This, in turn, produces an estimate of the carrier phase, $\hat{\theta}_k$, that will be held constant over the next baud period. The cosine and sine generators operate at the sample rate.

4.1.5 Four-Phase Costas Loop Implementation

Like the squaring loop, the Costas loop can be extended to higher modulations. A four-phase Costas loop, suitable for the detection of QPSK signals, is depicted in Figure 4.4. For convenience, we model the QPSK signal by

$$s(t) = \sqrt{2P}x(t)\cos(\omega_c t + \theta) - \sqrt{2P}y(t)\sin(\omega_c t + \theta) \tag{4.8}$$

where $x(t), y(t) \in \{\pm 1\}$ are the in-phase and quadrature bits at time t. Sampling at time k and multiplying digitally by the references

$$K_o \cos\left(\omega_c k T_s + \hat{\theta}\right) \quad \text{and} \quad -K_o \sin\left(\omega_c k T_s + \hat{\theta}\right)$$

produces quadrature samples, after ideal lowpass filtering, of the form

$$i_k = \sqrt{\frac{P}{2}}K_o x_k \cos\left(\theta - \hat{\theta}\right) - \sqrt{\frac{P}{2}}K_o y_k \sin\left(\theta - \hat{\theta}\right) \tag{4.9}$$

and

$$q_k = \sqrt{\frac{P}{2}}K_o x_k \sin\left(\theta - \hat{\theta}\right) + \sqrt{\frac{P}{2}}K_o y_k \cos\left(\theta - \hat{\theta}\right) . \tag{4.10}$$

For small phase error, $\hat{\theta} \approx \theta$, the outputs of the hardlimiting operations are taken to be $\text{Sgn}\{i_k\} = \hat{x}_k$ and $\text{Sgn}\{q_k\} = \hat{y}_k$. For reasonably high SNRs, assume that these decisions on x_k and y_k are correct, i.e., $\hat{x}_k = x_k$ and $\hat{y}_k = y_k$. Thus the feedback error term is given by

$$\begin{aligned} e_k &= i_k \text{Sgn}\{q_k\} - q_k \text{Sgn}\{i_k\} \\ &= \sqrt{\frac{P}{2}}K_o x_k y_k \cos\left(\theta - \hat{\theta}\right) + \sqrt{\frac{P}{2}}K_o x_k^2 \sin\left(\theta - \hat{\theta}\right) \\ &\quad -\sqrt{\frac{P}{2}}K_o x_k y_k \cos\left(\theta - \hat{\theta}\right) + \sqrt{\frac{P}{2}}K_o y_k^2 \sin\left(\theta - \hat{\theta}\right) \\ &= \sqrt{2P}K_o \sin\left(\theta - \hat{\theta}\right) \end{aligned} \tag{4.11}$$

which is the PLL-like control signal useful for tracking the input carrier.

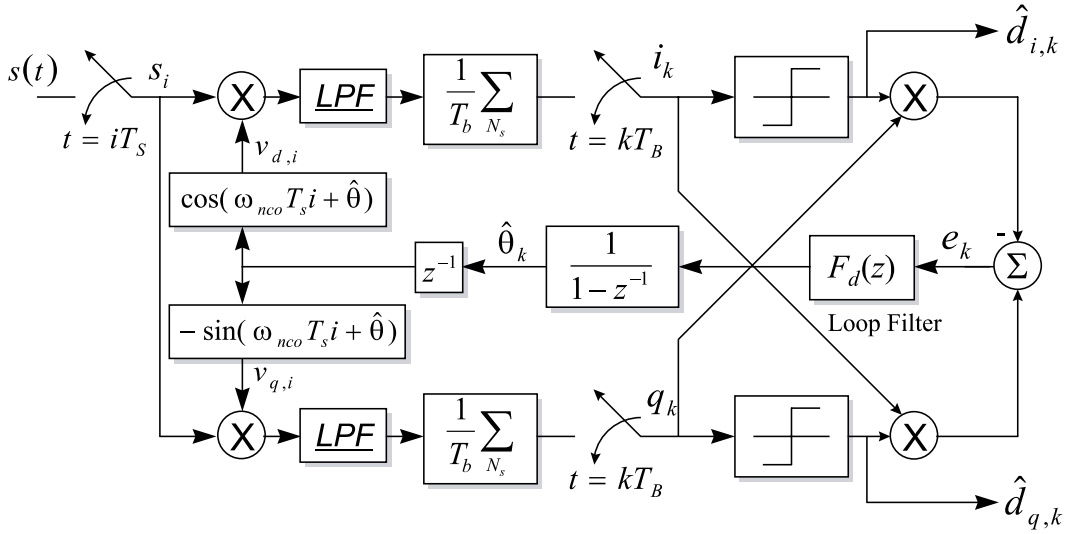

Figure 4.4: Block diagram of four-phase discrete-time Costas demodulator

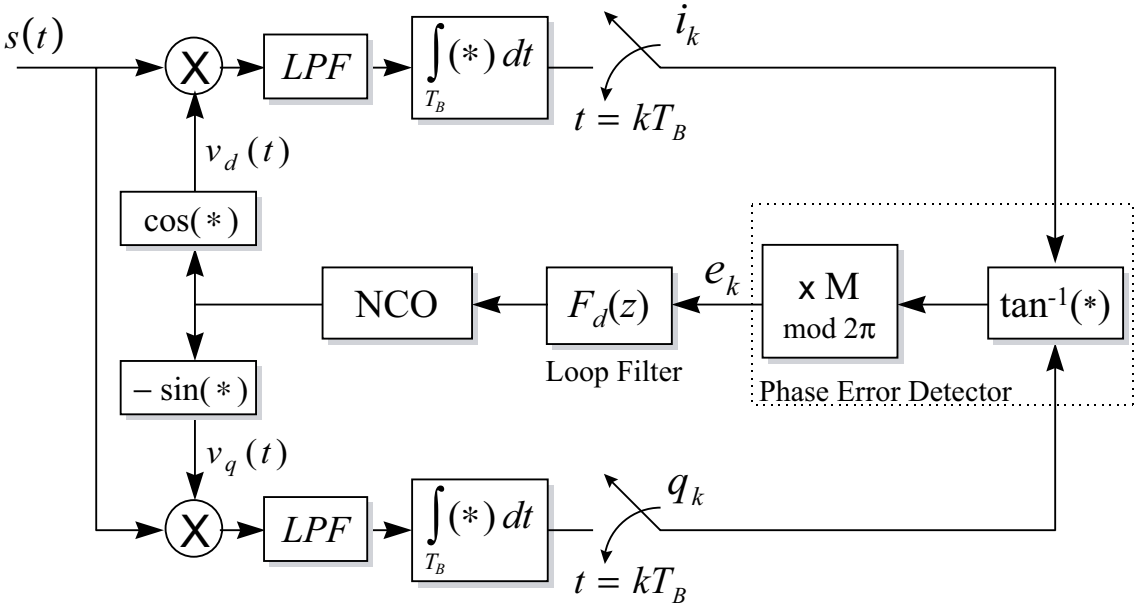

Figure 4.5: Block diagram of digital tanlock loop (DTL)

4.1.6 Digital Tanlock Loop

One noteworthy carrier recovery structure, the digital tanlock loop (DTL) shown in Figure 4.5, has only become feasible since the advent of high-speed digital logic circuits. As its name implies, it relies on an explicit arctangent operation to yield the phase error term. Thus, no approximations, such as $\sin\theta \approx \theta$, need be used. Except for noise and interference, the phase estimate is accurate during acquisition as well as during steady-state operation. The tanlock loop is shown in [50] to have several advantages over traditional closed-loop carrier recovery schemes. Among these is the fact that, since an explicit arctangent operation is used, the DTL is insensitive to amplitude variations and can thus operate without benefit of AGC, or as a demodulator for quadrature amplitude modulation (QAM) signalling formats. Note the multiplication by M, where M is the number of phase dimensions used in the signal set, introduces an M-ary phase ambiguity just as in more traditional carrier recovery circuits.

4.1.7 Discussion

Classical closed-loop carrier recovery structures, such as the squaring and Costas loops, were developed using continuous-time system models and have been implemented for many years with fully analog circuitry. In the past 30 years, as electronics technology has permitted, it has become ever more feasible to implement such loops with digital components. Over the last 15 years, it has become feasible to implement carrier recovery loops *entirely* with digitalcomponents. The DTL is an example of a closed-loop carrier recovery that owes its existence to these new capabilities. In much of the foregoing discussion, therefore, we have emphasized the discrete-time implementation of carrier recovery structures. This ever-increasing ability to now demodulate signals using digital, discrete-time components or software on a DSP leads naturally to the discussion of open-loop parameter estimation for the purpose of carrier recovery since open-loop structures are really only suited only for this type of implementation.

4.2 Open-Loop Carrier Recovery Structures

In this section, we survey a variety of open-loop estimation schemes applied to the problem of carrier recovery. Three open-loop phase estimators proposed in [41] serve well for the purposes of illustration. These are derived from the *maximum likelihood* (ML) principle. In sections 4.2.1, 4.2.4, and 4.2.5, we describe a first-order phase estimator, a modified first-order phase estimator, and a second-order phase estimator. The use of the term “order” is

original to this research as far as is known and is employed because the estimators presented have precise performance analogies to first-order, modified first-order, and second-order PLLs. These analogies will be drawn as the discussion progresses.

The derivation in section 4.2.1 suggests different ML estimation structures depending upon whether low SNR or high SNR conditions are assumed. Sections 4.2.2 and 4.2.3 describe the steady-state noise performance of each of these structures. In section 4.2.2 we derive the first and second-order statistics for the error of the first-order ML phase estimator. In a very useful result, we show that the notion of loop noise bandwidth, developed for PLLs and extended to closed-loop suppressed-carrier recovery structures, can be applied directly to open-loop estimators as well. Then in section 4.2.3, we do the same for the ML estimator derived from a high SNR approximation. Here, we show that the structure amounts to a decision feedback phase estimator, stochastically equivalent to a Costas loop with hard-limiting in the I-arm. We also show that, under the conditions of high SNR, the noise performance of the structure derived using the low SNR assumption converges to that of the optimal estimator. In section 4.2.6, we examine the performance of the phase estimation structures presented and validate the theoretical results given in sections 4.2.2 and 4.2.3. Finally, section 4.2.7 applies the open-loop phase estimation to the problem of carrier recovery for systems in which adaptive equalization is employed.

4.2.1 First-Order ML Phase Estimator

Figure 4.6 outlines the first-order ML phase estimator applied to binary phase modulation. Intuitively, the structure appears to be a simple averager, summing the squared input over N symbol observations. The squaring operation doubles the phase of input sample, which then enters the delay line. This doubling of phase is compensated for later by the square root operation, noting of course that, as with all closed-loop suppressed-carrier recovery schemes, the process produces a 180^o phase ambiguity. In the proceeding discussion, we wish to show rigorously that this structure does indeed provide the ML estimate of the signal phase for binary phase modulation in an AWGN channel.

To derive this structure, we expand the derivation given in [41]. Consider an input to the receiver given by

$$r_k = \sqrt{2P}e^{j(\phi_k+\theta)} + n_k \qquad kT \le t \le (k+1)T \tag{4.12}$$

where ϕ_k is the transmitted symbol such that $e^{j\phi_k} = d_k \in \{-1, +1\}$ at time kT, θ is the carrier phase, and n_k is a sample of a zero-mean, complex Gaussian process with variance $\sigma_n^2 = N_o/T$ in each signal dimension. Assume, for now, that θ does not vary over an

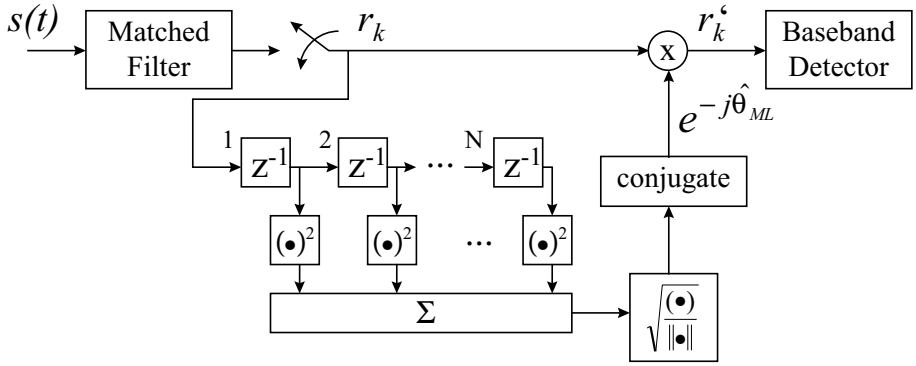

Figure 4.6: "First-order" open-loop ML phase estimation structure proposed in [41]

observation interval of length N samples. The likelihood function is thus given by

$$\begin{aligned} p(\mathbf{r} \mid \boldsymbol{\phi}, \theta) &= \left(\frac{1}{2\pi\sigma_n^2}\right)^N e^{-\frac{1}{2\sigma_n^2}\sum_{i=1}^{N}\left|r_{k-i} - \sqrt{2P}e^{j(\phi_{k-i}+\theta)}\right|^2} \\ &= \left(\frac{1}{2\pi\sigma_n^2}\right)^N e^{\frac{1}{2\sigma_n^2}\sum_{i=1}^{N}|r_{k-i}|^2 - 2\sqrt{2P}\Re\left\{r_{k-i}e^{-j(\phi_{k-i}+\theta)}\right\} + 2P} \\ &= F\ e^{\alpha\sum_{i=1}^{N}\Re\left\{r_{k-i}e^{-j(\phi_{k-i}+\theta)}\right\}} \end{aligned} \tag{4.13}$$

where $\Re(\cdot)$ is the real operator,

$$F = \left(\frac{1}{2\pi\sigma_n^2}\right)^N e^{-\frac{NP}{\sigma_n^2} + \sum_{i=1}^{N}|r_{k-i}|^2} \quad \text{and} \quad \alpha = \frac{\sqrt{2P}}{\sigma_n^2}\,. \tag{4.14}$$

Note that F and α are not dependent upon the data ϕ_k. We would like the ML estimate at time k, $\hat{\theta}_{ML,k}$ to satisfy

$$\ln\left[p(\mathbf{r}, \hat{\theta}_{ML,k})\right] = \underset{\theta}{\text{Max}} \ln\left[p(\mathbf{r}, \theta)\right]\,. \tag{4.15}$$

Now the probability of receiving samples $\mathbf{r}$ conditioned upon the carrier phase θ is given as

$$\begin{aligned} p(\mathbf{r} \mid \theta) &= E\left\{p(\mathbf{r} \mid \boldsymbol{\phi}, \theta)\right\} \\ &= F\prod_{i=1}^{N}\left(\frac{1}{2}\sum_{\phi_{k-i}} e^{\alpha\Re\left\{r_{k-i}e^{-j(\phi_{k-i}+\theta)}\right\}}\right) \\ &= F\prod_{i=1}^{N}\cosh\left(\alpha\Re\left\{r_{k-i}e^{-j\theta}\right\}\right) \end{aligned} \tag{4.16}$$

where $E(\cdot)$ denotes the expectation operator. Taking natural logarithms, we have

$$\ln\left[p(\mathbf{r},\theta)\right] = \ln F + \sum_{i=1}^{N} \ln\left[\cosh\left(\alpha \Re\left\{r_{k-i}e^{-j\theta}\right\}\right)\right] . \tag{4.17}$$

Now differentiating with respect to θ and setting equal to zero, we obtain

$$\sum_{i=1}^{N} \tanh\left(\alpha \Re\left\{r_{k-i}e^{-j\theta}\right\}\right) \cdot \Re\left\{jr_{k-i}e^{-j\theta}\right\} = 0 . \tag{4.18}$$

At this point, a solution for θ yields $\hat{\theta}_{ML}$. Unfortunately, no closed form solution yet exists for (4.18), and more importantly, it gives us no intuitive knowledge about constructing a receiver based upon it. We now proceed to derive the structure shown in Figure 4.6 by assuming $\alpha < 1$, i.e., under low input SNR conditions. Under these assumtions we use $\tanh x \approx x$. Then $\hat{\theta}_{ML,k}$ ought satisfy

$$\sum_{i=1}^{N} \Re\left\{r_{k-i}e^{-j\hat{\theta}_{ML,k}}\right\} \Re\left\{jr_{k-i}e^{-j\hat{\theta}_{ML,k}}\right\} = 0 . \tag{4.19}$$

Solving directly for $e^{j\hat{\theta}_{ML,k}}$ yields

$$e^{j\hat{\theta}_{ML,k}} = \sqrt{\frac{\sum_{i=1}^{N} r_{k-i}^2}{\left|\sum_{i=1}^{N} r_{k-i}^2\right|}} \tag{4.20}$$

which is precisely the functionality shown in Figure 4.6.

Now, what about high SNR conditions? After all, if our estimation structure is the best estimator we can hope for in low SNR, we would surely like it to be optimal or at least nearly so in the far more common high SNR condition. High SNR allows us to assume $\alpha \gg 1$ and $\Re\{r_k e^{-j\theta}\} \approx Ae^{j\phi_k} = Ad_k$. Thus we may use $\tanh(Ad_k) \approx \mathrm{Sgn}\,(Ad_k) = d_k$ in (4.18). Under these conditions then, $\hat{\theta}'_{ML}$ ought satisfy

$$\sum_{i=1}^{N} d_{k-i} \Re\left\{jr_{k-i}e^{-j\hat{\theta}'_{ML,k}}\right\} = 0 . \tag{4.21}$$

Solving for $e^{j\hat{\theta}'_{ML,k}}$ now yields

$$e^{j\hat{\theta}'_{ML,k}} = \frac{\sum_{i=1}^{N} d_{k-i} r_{k-i}}{\left|\sum_{i=1}^{N} d_{k-i} r_{k-i}\right|} \tag{4.22}$$

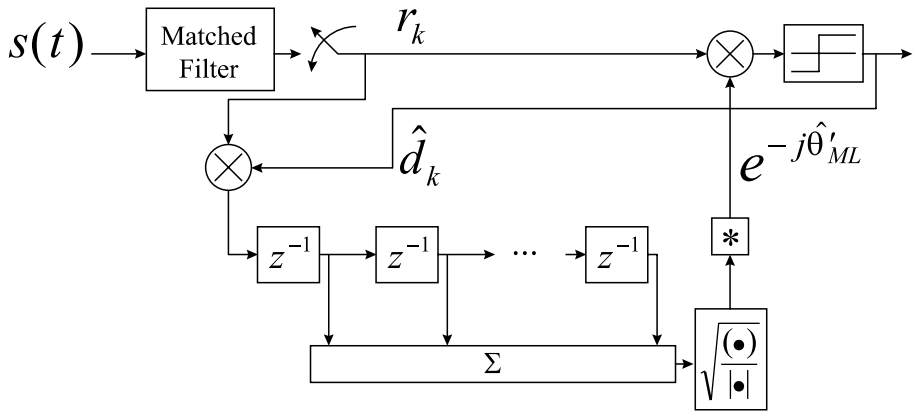

Figure 4.7: Decision feedback open-loop phase estimation structure derived from the ML principle under "high" SNR assumptions

which suggests a decision feedback carrier recovery structure shown in Figure 4.7. This structure *seems* analogous to the practice of hard limiting the I-arm in a Costas loop in high SNR conditions.

While this is intuitively satisfying, it nevertheless is not the estimate given by (4.20). In sections 4.2.2 and 4.2.3, we derive the first and second-order statistics for estimators (4.20) and (4.22) respectively. Our goal is to show that these converge to the same values under high SNR assumptions. We further note that the differences between (4.22) and (4.20) are precisely analogous to the differences between hard-limiting and not limiting the I-arm in a Costas loop. Moreover, we show that in both cases, a precise analogy exists between the loop bandwidth of a Costas loop or PLL and the structures suggested by (4.20) and (4.22).

4.2.2 Noise Performance of Low SNR ML Phase Estimator

Consider now the error of the estimator given in (4.20), namely $\hat{\theta}_{e,k} \triangleq \hat{\theta}_{ML,k} - \theta$. Squaring (4.20) and taking natural logarithms yields

$$\hat{\theta}_{ML,k} = \frac{1}{2} \arg \left(\sum_{i=1}^{N} r_{k-i}^2 \right) \tag{4.23}$$

where $\arg(\cdot) \triangleq \tan^{-1}\left(\frac{\Im(\cdot)}{\Re(\cdot)}\right)$ and $\Re(\cdot)$ and $\Im(\cdot)$ are the real and imaginary operators. We note that $-\theta = \arg\left(e^{-j\theta}\right) = \frac{1}{2}\arg\left(e^{-j2\theta}\right)$. Therefore

$$\hat{\theta}_{e,k} = \frac{1}{2} \arg \left(e^{-j2\theta} \sum_{i=1}^{N} r_{k-i}^2 \right) \ . \tag{4.24}$$

Now

$$r_k = Ad_k e^{j\theta} + \tilde{n}_k \tag{4.25}$$

where $A = \sqrt{2P}$, $d_k = e^{j\phi_k} \in \{-1, +1\}$ is the transmitted BPSK symbol at time k and $\tilde{n}_k = n_{d,k} + jn_{q,k}$, $n_d, n_q \sim \text{Normal}(0, \sigma_n^2)$. It is convenient to define

$$\begin{aligned} z_{2\theta,k} &\triangleq \sum_{i=1}^{N} r_{k-i}^2 \\ &= NA^2 e^{j2\theta} + 2Ad_k e^{j\theta} \sum_{i=1}^{N} (n_{d,i} + jn_{q,i}) \\ &\quad + \sum_{i=1}^{N} \left(\left(n_{d,i}^2 - n_{q,i}^2 \right) + j2n_{d,i}n_{q,i} \right) . \end{aligned} \tag{4.26}$$

Further, we define

$$\begin{aligned} z_k &\triangleq e^{-j2\theta} \cdot z_{2\theta,k} \\ &= NA^2 + 2Ad_k e^{-j\theta} \sum_{i=1}^{N} (n_{d,i} + jn_{q,i}) \\ &\quad + e^{-j2\theta} \sum_{i=1}^{N} \left(\left(n_{d,i}^2 - n_{q,i}^2 \right) + j2n_{d,i}n_{q,i} \right) . \end{aligned} \tag{4.27}$$

For convenience we also wish to define auxilliary noise variables $n'_d = n_d + n_q$ and $n'_q = n_d - n_q$ such that $n_d^2 - n_q^2 = n'_d n'_q$. We note that $n'_d, n'_q \sim \text{Normal}(0, 2\sigma_n^2)$ and can be shown to be mutually independent as well as independent of n_d and n_q. Thus (4.27) may be rewritten as

$$z_k = NA^2 + 2Ad_k e^{-j\theta} \sum_{i=1}^{N} (n_{d,i} + jn_{q,i}) + e^{-j \sum_{i=1}^{N} \left(\left(n'_{d,i} n'_{q,i} \right) + j2n_{d,i}n_{q,i} \right)} . \tag{4.28}$$

Thus the error of the phase estimate may now be given by

$$\hat{\theta}_{e,k} = \frac{1}{2} \arg(z_k) = \frac{1}{2} \tan^{-1} \left(\frac{\Im(z_k)}{\Re(z_k)} \right) . \tag{4.29}$$

We now define auxilliary random noise variables λ_1 and λ_2 by

$$\begin{aligned} \lambda_{1,k} &\triangleq \Im(z_k) \\ &= 2Ad_k \left(\cos\theta \sum_{i=1}^{N} n_{q,i} - \sin\theta \sum_{i} n_{d,i} \right) \\ &\quad + 2\cos 2\theta \sum_{i=1}^{N} n_{d,i}n_{q,i} - \sin 2\theta \sum_{i} n'_{d,i}n'_{q,i} \end{aligned} \tag{4.30}$$

and

$$\begin{aligned}\lambda_{2,k} &\stackrel{\triangle}{=} \Re(z_k) - NA^2 \\ &= 2Ad_k\left(\cos\theta\sum_{i=1}^{N} n_{d,i} + \sin\theta\sum_{i=1}^{N} n_{q,i}\right) \\ &\quad +2\sin 2\theta\sum_{i=1}^{N} n_{d,i}n_{q,i} + \cos 2\theta\sum_{i=1}^{N} n'_{d,i}n'_{q,i} \end{aligned} \tag{4.31}$$

which allow us to express the estimation error as

$$\hat{\theta}_{e,k} = \frac{1}{2}\tan^{-1}\left(\frac{\lambda_{1,k}}{NA^2+\lambda_{2,k}}\right) . \tag{4.32}$$

Before proceeding any further, let us consider the first- and second-order statistics of the noise variables λ_1 and λ_2. Considering the first of these, we may write

$$\begin{aligned} E[\lambda_{1,k}] &= 2AE[d_k]\cos\theta E\left[\sum_{i=1}^{N} n_{q,i}\right] - 2AE[d_k]\sin\theta E\left[\sum_{i=1}^{N} n_{d,i}\right] + 2\cos 2\theta E\left[\sum_{i=1}^{N} n_{d,i}n_{q,i}\right] \\ &\quad - \sin 2\theta E\left[\sum_{i=1}^{N} n'_{d,i}n'_{q,i}\right] \\ &= 0 . \end{aligned} \tag{4.33}$$

Analogously, it can be shown that $E[\lambda_{2,k}] = 0$. So the expected value of each of the noise variables is zero. We now consider the variance of λ_1. First of all,

$$\begin{aligned} \lambda_{1,k}^2 &= \left[2Ad_k\left(\cos\theta\sum_{i=1}^{N} n_{q,i} - \sin\theta\sum_{i=1}^{N} n_{d,i}\right) + 2\cos 2\theta\sum_{i=1}^{N} n_{d,i}n_{q,i} - \sin 2\theta\sum_{i=1}^{N} n'_{d,i}n'_{q,i}\right]^2 \\ &= 4A^2\left(\cos^2\theta\left(\sum_{i=1}^{N} n_{q,i}\right)^2 + \sin^2\theta\left(\sum_{i=1}^{N} n_{d,i}\right)^2 - 2\cos\theta\sin\theta\sum_{i=1}^{N} n_{q,i}\sum_{i} n_{d,i}\right) \\ &\quad +4\cos^2 2\theta\left(\sum_{i=1}^{N} n_{d,i}n_{q,i}\right)^2 + \sin^2 2\theta\left(\sum_{i=1}^{N} n'_{d,i}n'_{q,i}\right)^2 \\ &\quad +4Ad_k\,(\text{four noise terms}) - 4\cos 2\theta\sin\theta\sum_{i=1}^{N} n_{d,i}n_{q,i}\sum_{i=1}^{N} n'_{d,i}n'_{q,i} . \end{aligned} \tag{4.34}$$

Examining the expectations of the various noise terms in (4.34), we find

$$E\ [d_k] = 0 \tag{4.35}$$

$$E\left[\sum_{i=1}^{N} n_{q,i}\sum_{i} n_{d,i}\right] = 0 \tag{4.36}$$

$$E\left[\left(\sum_{i=1}^{N} n_{q,i}\right)^2\right] = E\left[\left(\sum_{i=1}^{N} n_{d,i}\right)^2\right] = N\sigma_n^2 \tag{4.37}$$

$$E\left[\left(\sum_{i=1}^{N} n_{d,i}n_{q,i}\right)^2\right] = N\sigma_n^4 \tag{4.38}$$

$$E\left[\left(\sum_{i=1}^{N} n'_{d,i}n'_{q,i}\right)^2\right] = 4N\sigma_n^4 \tag{4.39}$$

$$\text{and} \qquad E\left[\sum_{i=1}^{N} n_{d,i}n_{q,i}\sum_{i=1}^{N} n'_{d,i}n'_{q,i}\right] = 0\,. \tag{4.40}$$

Using (4.35) through (4.40) in (4.34) and taking the expectation, we obtain

$$\begin{aligned} E\left[\lambda_{1,k}^2\right] &= 4A^2\left(\cos^2\theta N\sigma_n^2 + \sin^2\theta N\sigma_n^2\right) + 4\cos^2 2\theta N\sigma_n^4 + \sin^2 2\theta \cdot 4N\sigma_n^4 \\ &= 4NA^2\sigma_n^2 + 4N\sigma_n^4\,. \end{aligned} \tag{4.41}$$

It can be shown that $E\left[\lambda_{2,k}^2\right] = E\left[\lambda_{1,k}^2\right]$.

Now let us reconsider the error or the ML phase estimator given in (4.32). Let us examine this error for a limited subset of all k, denoted by κ, where the realizations of the noise processes λ_1 and λ_2 at times κ produce an argument to the arctangent operation that is smaller than one. For the assumption of high SNR which is being made, the constant NA^2 in the denominator of (4.32) is much larger than the variance of either λ_1 or λ_2. This leads the useful conclusion that the occurrences κ are highly probable within the set of all k. In fact, in the limit as SNR $\to \infty$, the set of all κ is approaches the set of all k. For the realizations at time κ, we therefore allow $\tan^{-1}(x) \approx x$. Thus[§]

$$\hat{\theta}_{e,\kappa} \approx \frac{1}{2}\cdot\frac{\lambda_{1,\kappa}}{NA^2 + \lambda_{2,\kappa}}\,. \tag{4.42}$$

In order to make use of expectation operators, we now make the assumption that the output random process is independent of the input noise processes. This is precisely analogous to the assumption of independence of the steady-state phase error in a PLL to the additive input noise made in section 3.4.1. As noted in that section, this type of assumption is made in all known PLL treatments, and further yields results consistent with those observed in practical systems. The independence assuption allows

$$\begin{aligned} & \hat{\theta}_{e,\kappa}\left(NA^2 + \lambda_{2,\kappa}\right) \approx \frac{1}{2}\lambda_{1,\kappa} \\ \Longrightarrow \quad & E\left[\hat{\theta}_{e,\kappa}\right]\left(NA^2 + E\left[\lambda_{2,\kappa}\right]\right) \approx \frac{1}{2}E\left[\lambda_{1,\kappa}\right] \\ \Longrightarrow \quad & E\left[\hat{\theta}_{e,\kappa}\right] \approx \frac{1}{2}\cdot\frac{E\left[\lambda_{1,\kappa}\right]}{NA^2 + E\left[\lambda_{2,\kappa}\right]} \end{aligned} \tag{4.43}$$

[§]The Taylor series expansion of arctangent takes three forms. For the region between ± 1 the first term of the approximation produces (4.42), and higher-order terms become neglible based on the assumptions used here. Use of this expansion, however, still requires the assumption that the argument to the arctangent, itself a function of random variables, lies between ± 1. Our approach does not explicitly rely on such an assumption, and is therefore presented as an alternative to the Taylor series expansion.

as an approximation of the mean of the ML estimator given in Figure 4.6 for times κ. Similarly,

$$E\left[\hat{\theta}_{e,\kappa}^2\right] \approx \frac{1}{4} \cdot \frac{E\left[\lambda_{1,\kappa}^2\right]}{N^2A^4 + E\left[\lambda_{2,\kappa}^2\right] + 2NA^2E\left[\lambda_{2,\kappa}\right]} \tag{4.44}$$

approximates the error variance at times κ. But the noise processes λ_1 and λ_2 are clearly stationary upon inspection of (4.30) and (4.31). So we may state with equivalent certainty that at times κ,

$$E\left[\hat{\theta}_{e,\kappa}\right] \approx \frac{1}{2} \cdot \frac{E\left[\lambda_{1,k}\right]}{NA^2 + E\left[\lambda_{2,k}\right]} \tag{4.45}$$

and

$$E\left[\hat{\theta}_{e,\kappa}^2\right] \approx \frac{1}{4} \cdot \frac{E\left[\lambda_{1,k}^2\right]}{N^2A^4 + E\left[\lambda_{2,k}^2\right] + 2NA^2E\left[\lambda_{2,k}\right]} \,. \tag{4.46}$$

Now the first- and second-order statistics of the estimation error are no longer dependent upon κ. So we may finally state

$$E\left[\hat{\theta}_{e,k}\right] \approx \frac{1}{2} \cdot \frac{E\left[\lambda_{1,k}\right]}{NA^2 + E\left[\lambda_{2,k}\right]} \tag{4.47}$$

and

$$E\left[\hat{\theta}_{e,k}^2\right] \approx \frac{1}{4} \cdot \frac{E\left[\lambda_{1,k}^2\right]}{N^2A^4 + E\left[\lambda_{2,k}^2\right] + 2NA^2E\left[\lambda_{2,k}\right]} \,. \tag{4.48}$$

Given the values for $E\left[\lambda_{1,k}\right] = E\left[\lambda_{2,k}\right]$ and $E\left[\lambda_{1,k}^2\right] = E\left[\lambda_{2,k}^2\right]$ in (4.33) and (4.41), we may now solve (4.43) and (4.44). The first- and second-order statistics for the ML estimator derived from a low SNR assumption are given by

$$E\left[\hat{\theta}_{e,k}\right] \approx 0 \tag{4.49}$$

which is not terribly surprising, and

$$E\left[\hat{\theta}_{e,k}^2\right] \approx \frac{A^2\sigma_n^2 + \sigma_n^4}{NA^4 + 4A^2\sigma_n^2 + 4\sigma_n^4} \tag{4.50}$$

which proves to be an interesting result indeed. Let $\rho = \dfrac{A^2}{2\sigma_n^2} = E_b/N_o$ be the symbol SNR. We may then express (4.50) as

$$E\left[\hat{\theta}_{e,k}\right] \approx \frac{2\rho + 1}{4N\rho^2 + 4\rho + 4} \,. \tag{4.51}$$

Maintaining the high SNR assumption and reasonably large N, we may legitimately assume $N\rho^2 \gg \rho + 1$. Therefore

$$E\left[\hat{\theta}_{e,k}^2\right] \approx \frac{2\rho + 1}{4N\rho^2} = \frac{1}{2N\rho}\left(1 + \frac{1}{2\rho}\right) \,. \tag{4.52}$$

This is a most intuitively satisfying result since it is an exact analogy to the steady-state noise variance obtained for a Costas loop in (4.4), *including* squaring loss. Furthermore, the notion of *loop noise bandwidth*, developed in Chapter 3 for the PLL has a direct application to this open-loop estimator. Simply by equating (4.52) with (4.4), we find an *equivalent loop bandwidth* for the open-loop estimator, which is given by

$$B_{L,\hat{\theta}} = \frac{B_i}{2N} \tag{4.53}$$

where $B_i = R_b = 1/T_b$ for the estimator of Figure 4.6.¶

4.2.3 Noise Performance of High SNR ML Phase Estimator

Taking natural logarithms and rearranging (4.22), we write

$$\hat{\theta}'_{ML,k} = \arg\left(\sum_{i=1}^{N} d_{k-i} r_{k-i}\right) . \tag{4.54}$$

It is convenient to define z'_θ as

$$\begin{aligned} z'_{\theta,k} &\triangleq \sum_{i=1}^{N} d_{k-i} r_{k-i} \\ &= \sum_{i=1}^{N} A e^{j\theta} + \tilde{n}_i \end{aligned} \tag{4.55}$$

where $\tilde{n}_i$ and A are as defined in 4.25. Note that the modulation is simply removed in the sum. We further define

$$\begin{aligned} z'_k &\triangleq e^{-j\theta} \cdot z'_{\theta,k} \\ &= AN + \cos\theta \sum_{i=1}^{N} n_{d,i} + \sin\theta \sum_{i=1}^{N} n_{q,i} + j\left(\cos\theta \sum_{i=1}^{N} n_{q,i} - \sin\theta \sum_{i=1}^{N} n_{d,i}\right) . \end{aligned} \tag{4.56}$$

Let

$$\begin{aligned} \lambda'_{1,k} &\triangleq \Im(z'_k) \\ &= \cos\theta \sum_{i=1}^{N} n_{q,i} - \sin\theta \sum_{i=1}^{N} n_{d,i} \end{aligned} \tag{4.57}$$

$$\begin{aligned} \text{and} \quad \lambda'_{2,k} &\triangleq \Re(z'_k) - AN \\ &= \cos\theta \sum_{i=1}^{N} n_{d,i} + \sin\theta \sum_{i=1}^{N} n_{q,i} . \end{aligned} \tag{4.58}$$

¶As far as is known, the expression of the stochastic steady-state performance of open-loop phase estimators in terms of "loop bandwidth" is original to this research.

Then the random variable $\hat{\theta}'_{e,k}$, which is the error of the estimator given in (4.22), may be given by

$$\hat{\theta}'_{e,k} = \arg\left(z'_k\right) = \tan^{-1}\left(\frac{\lambda'_{1,k}}{AN + \lambda'_{2,k}}\right) . \tag{4.59}$$

Following precisely the same arguments posited in section 4.2.2, we jump to the approximation

$$\hat{\theta}'_{e,k} \approx \frac{\lambda'_{1,k}}{AN + \lambda'_{2,k}} . \tag{4.60}$$

Again, we now make the assumption of independence between $\hat{\theta}'_{e,k}$ and the input noise and write

$$E\left[\hat{\theta}'_{e,k}\right] \approx \frac{E\left[\lambda'_{1,k}\right]}{AN + E\left[\lambda'_{2,k}\right]} . \tag{4.61}$$

Clearly, from observation of (4.57) and (4.58), the expected values of $\lambda'_{1,k}$ and $\lambda'_{2,k}$ are zero. So, as expected, the error is zero mean.

Concerning the variance of the high SNR estimator, we may write

$$\hat{\theta}'^2_{e,k} \approx \frac{\lambda'^2_{1,k}}{A^2N^2 + \lambda'^2_{2,k} + 2AN\lambda'_{2,k}} . \tag{4.62}$$

Again, assumed independence allows

$$E\left[\hat{\theta}'^2_{e,k}\right] \approx \frac{E\left[\lambda'^2_{1,k}\right]}{A^2N^2 + E\left[\lambda'^2_{2,k}\right] + E\left[2AN\lambda'_{2,k}\right]} = \frac{E\left[\lambda'^2_{1,k}\right]}{A^2N^2 + E\left[\lambda'^2_{2,k}\right]} . \tag{4.63}$$

We note that

$$\begin{aligned} \lambda'^2_{1,k} &= \cos^2\theta\left(\sum_{i=1}^{N} n_{q,i}\right)^2 + \sin^2\theta\left(\sum_{i=1}^{N} n_{d,i}\right)^2 - \sin\theta\cos\theta\sum_{i=1}^{N} n_{d,i}\sum_{i=1}^{N} n_{q,i} \\ \Longrightarrow E\left[\lambda'^2_1\right] &= N\sigma_n^2 \end{aligned} \tag{4.64}$$

$$\begin{aligned} \text{and} \quad \lambda'^2_2 &= \cos^2\theta\left(\sum_{i=1}^{N} n_{d,i}\right)^2 + \sin^2\theta\left(\sum_{i=1}^{N} n_{q,i}\right)^2 + \sin\theta\cos\theta\sum_{i=1}^{N} n_{d,i}\sum_{i=1}^{N} n_{q,i} \\ \Longrightarrow E\left[\lambda'^2_2\right] &= N\sigma_n^2 . \end{aligned} \tag{4.65}$$

Thus

$$E\left[\hat{\theta}'^2_{e,k}\right] \approx \frac{N\sigma_n^2}{A^2N^2 + N\sigma_n^2} . \tag{4.66}$$

As in section 4.2.2, letting $\rho = \dfrac{A^2}{2\sigma_n^2} = E_b/N_o$ yields

$$E\left[\hat{\theta}'^2_{e,k}\right] \approx \frac{1}{2N\rho + 1} . \tag{4.67}$$

Finally, since under high SNR we may assume $2N\rho \gg 1$, we write

$$E\left[\hat{\theta}'^2_{e,k}\right] \approx \frac{1}{2N\rho} \,. \tag{4.68}$$

We note that this variance could be obtained by considering an *efficient*[‖] estimator's equality with the Cramer-Rao bound [33], an aspect of estimation theory not explored in this research. Comparing (4.68) with (4.52), we see that the only difference between them comes from squaring loss.

So the controversy that arose in section 4.2.1, that a high SNR assumption leads to a different ML estimation structure than a low SNR assumption, has been solved. First, the errors of both are shown to be zero mean. Further, by allowing $\rho \to \infty$ in (4.52), it is clear that the second-order statistics also converge to the same values. Clearly then the estimation structure suggested by (4.20) and implemented in Figure 4.6, which was derived from a low SNR approximation, is still nearly optimal under high SNR conditions. Moreover, we have shown that the only way to improve upon the squaring structure is to implement decision feedback as shown in Figure 4.7 where, under low noise assumptions $\hat{d}_k = d_k$. In addition, we have shown that the squaring estimation structure suggested by (4.20) is stochastically equivalent to the generalized Costas loop and that the decision feedback structure suggested by (4.22) is stochastically equivalent to a Costas loop with hard-limiting in the I-arm. Finally, we have shown that there is an analogous *loop bandwidth* for this class of estimators given by (4.53).

4.2.4 Modified First-Order ML Phase Estimator

Consider now the situation where the carrier phase θ is *not* constant for the length of time over which N observations of r_k are taken. Assume rather that there is a residual carrier frequency offset in the received symbols r_k, which corresponds to imperfect downconversion. This condition is almost certain to be the case in any realistic radio receiver. Intuitively, we would now no longer expect either of the structures proposed in section 4.2.1 to track the incoming phase with zero error. For this reason alone, we choose to call these *first-order* carrier recovery structures since a first-order PLL has precisely this same property. That is, a first-order PLL cannot track a frequency step, or equivalently a phase ramp, with a zero mean steady-state error. As with the first-order PLL, then, we do not consider the first-order estimation structures suggested and analyzed in the preceding three sections to be

[‖] A ML estimate, when obtainable, is considered to be efficient. Put very simply, the estimator structure suggested by (4.22) is a simple averager of Gaussian random variables, i.e., receiver decision statistics, with variance $\frac{1}{2}N_o/E_b$. We would intuitively expect this variance to thus decrease by N, the number of statistics averaged.

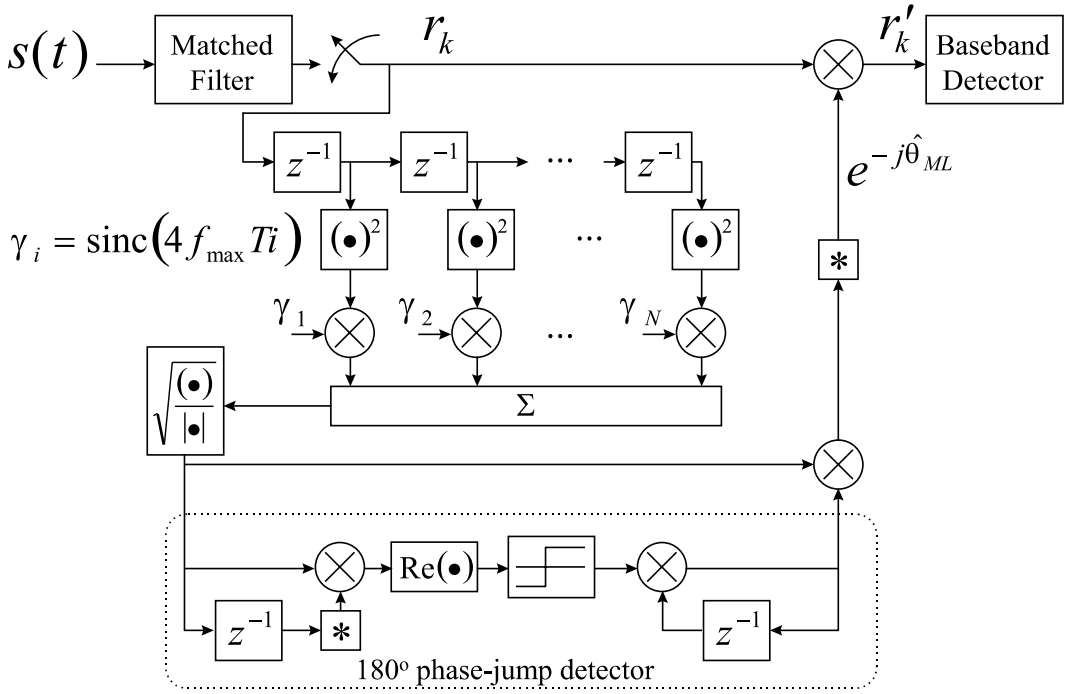

Figure 4.8: Modified first-order ML phase estimation structure, suitable for the conditions of "small" residual frequency offset

applicable to the general task of suppressed-carrier recovery. Alas, the foregoing discussion has not been in vain, however. In sections 4.2.4 and 4.2.5 we undertake a discussion of modifications to the preceding basic estimation structures that allow them to operate in the realistic conditions of residual frequency offset.

Assume now that the carrier phase at time kT may be represented by

$$\theta_k = \theta_o + 2\pi f k T \tag{4.69}$$

where f denotes the frequency offset and θ_o is some initial carrier phase. Similarly, the phase at time $(k-i)T$ is related to the phase at time kT by

$$\theta_{k-i} = \theta_k - 2\pi f i T \ . \tag{4.70}$$

As in section 4.2.1, we are still interested in estimating the phase using N past observations of received samples, $\mathbf{r} = \{r_{k-1}, r_{k-2}, ..., r_{k-N}\}^T$ where ^{T} denotes the transpose operator. Now however, θ is not constant, and we must therefore attempt to come up with an estimate of θ_k. Specifically, we wish to find

$$p\left(\mathbf{r} \mid \hat{\theta}_{k,ML}\right) = \underset{\theta_k}{\text{Max}}\, p\left(\mathbf{r} \mid \theta_k\right) \ . \tag{4.71}$$

Divsalar and Simon in [41] show that by averaging out equiprobable data and averaging over a uniform frequency shift distribution from $-f_{max}$ to f_{max}, where f_{max} corresonds to maximum expected value of doppler shift, we may express the argument to the max function in 4.71 as

$$\begin{aligned} p\left(\mathbf{r} \mid \theta_k\right) &\triangleq E\left[p\left(\mathbf{r} \mid \boldsymbol{\phi}, \theta_k, f\right)\right] \\ &= \frac{F}{2f_{max}} \int_{-f_{max}}^{f_{max}} df \prod_{i=1}^{N} \cosh\left(\alpha \Re\left\{R_{k-i} e^{-j\theta_k}\right\}\right) \end{aligned} \tag{4.72}$$

where F and α are as defined in 4.13 and $R_{k-i} \triangleq r_{k-i} e^{j2\pi f i T}$. Thus, to obtain, $\hat{\theta}_{k,ML}$ we must find

$$\left.\frac{\partial p\left(\mathbf{r} \mid \theta_k\right)}{\partial \theta_k}\right|_{\theta_k = \hat{\theta}_{k,ML}} = 0\,. \tag{4.73}$$

Using a low SNR assumption, the solution to 4.73 is given in [41] as

$$e^{j\hat{\theta}_{ML,k}} = \sqrt{\frac{\sum_{i=1}^{N} r_{k-i}^2 \mathrm{sinc}\left(4 f_{max} i T\right)}{\left|\sum_{i=1}^{N} r_{k-i}^2 \mathrm{sinc}\left(4 f_{max} i T\right)\right|}} \tag{4.74}$$

where $\mathrm{sinc}(x) \triangleq \frac{\sin \pi x}{\pi x}$, which suggests the receiver structure outlined in Figure 4.8. Note the addition of the 180^o phase jump detector.** Without this, the detector will make an error each time the input signal constellation crosses the imaginary axis. This is due the fact that the combination of the square root and squaring operations limits the range of the phase estimate to $(-\pi, \pi]$, whereas the actual phase is continuous around the unit circle in the complex plain. This phase jump detector alleviates this problem (with a small amount of degradation due to noise) by detecting crossings of the imaginary axis and multiplying the phase estimator by ± 1 appropriately.

We denote the structure suggested by (4.74) as the *modified first-order* ML phase estimator since it contains no explicit frequency estimation. A range of possible frequency offset must be known *a priori*, and therefore, in an arbitrary frequency offset, this estimation structure would clearly be suboptimal. In addition, those who proposed this scheme in [41] do so only with the caveat that it will work when the residual frequency offset is fairly "small." We therefore liken this structure to the second-order PLL, built with a loop filter

**The feedback structure seen at the output of the phase jump detector is depicted as a feed forward structure in [41]. The feed forward structure was clearly the result of an editing error in this excellent source, and was discovered and corrected as part of this research. Figures 4.8 and 4.9 depict the jump detector correctly.

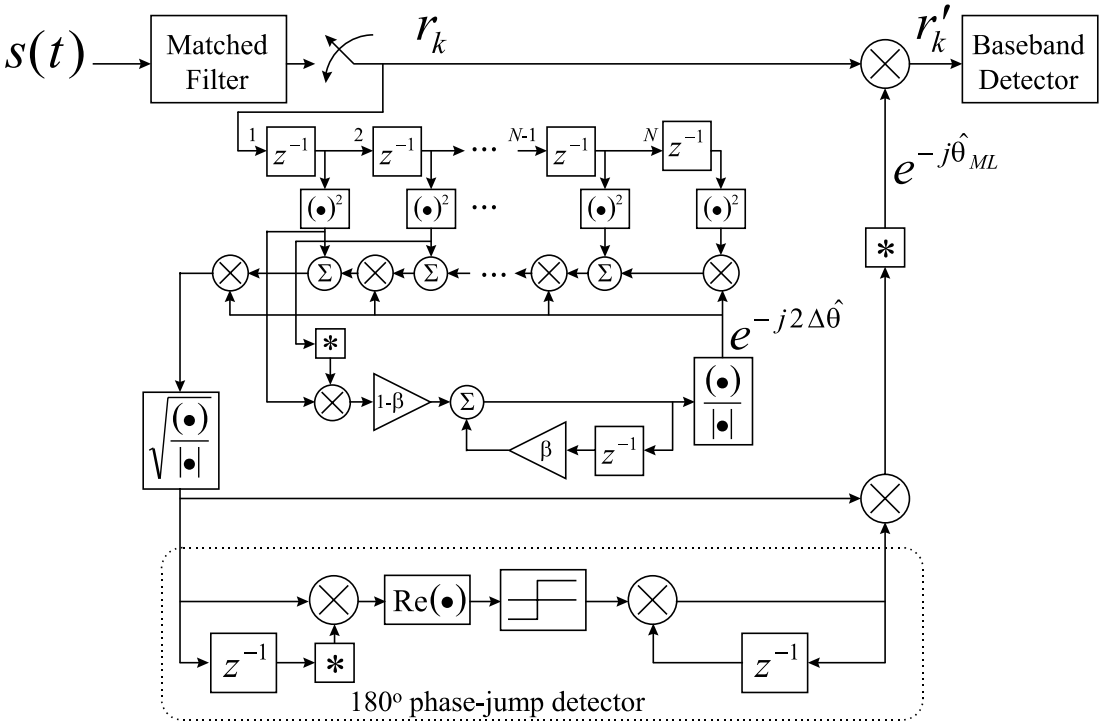

Figure 4.9: Second-order ML phase estimation structure with dedicated frequency estimation, suitable for the conditions of "large" residual frequency offset

without infinite DC gain. As noted in Chapter 3, such a second-order PLL is better described as a modified first-order PLL since it cannot completely compensate for a frequency offset with a non-zero steady-state error as can the canonical second-order PLL defined by (3.9). A better match to this canonical second-order PLL is presented in section 4.2.5.

4.2.5 Second-Order ML Phase Estimator

In the final open-loop structure examined in this work, shown in Figure 4.9, we add an open-loop frequency estimation scheme to the structure outlined originally in Figure 4.6. Note that this too has the 180^o phase jump detector to reconcile the periodic phase ambiguities arising from a constant rotation in the input constellation. The functionality of Figure 4.9 precisely parallels that of the ML estimator in 4.6 except that a structure that attempts to estimate the *change* in the (squared) phase, $2\Delta\theta$, is added in parallel. The estimates of $2\Delta\theta$ are filtered by a lag filter with the transfer function

$$F(z) = \frac{1-\beta}{1-\beta z^{-1}} \tag{4.75}$$

where β, though not explicitly defined in [41], is assumed to be a constant relatively close to but less than one and controls the "memory" of the estimate integration. Finally, note that for high SNR operating conditions, the squaring operations in both the modified first-order and second-order phase estimators can be replaced by a decision feedback scheme as suggested in Figure 4.7.

4.2.6 Simulation Study of Open-Loop Phase Estimators

Before considering a crucial application of open-loop ML estimation, namely adaptive equalization, we present a few results from a simulation study on the performance of the estimation structures derived in the preceding sections. Most importantly, this validates the theoretical results predicted in sections 4.2.2 and 4.2.3. In addition, it gives a high level view of the type of conditions under which the proposed estimation schemes can be expected to work.

Figures 4.10 and 4.11 completely validate, via simulation, the expected noise performance of both first-order estimators as given in (4.52) and (4.68). Figure 4.10 shows the simulation results of the variance in the phase estimator given by (4.20), in which a squaring operation is used to remove the modulation. Results are plotted versus N, the number of symbols averaged over, and for E_b/N_o ranging from 0 to 24 dB. The solid lines show the variance predicted for this estimator under the high SNR assumption given by (4.52), which includes squaring loss. Note that the match is almost perfect down to about 0 dB where, as expected, the high SNR approximation is no longer valid and the estimator's performance degrades.

Figure 4.11 shows similar results obtained for the decision feedback phase estimator suggested by (4.22). Again, results are plotted versus N and for a range of E_b/N_o from 8 to 24 dB. Simulations were run for 0 and 4 dB, but the high SNR assumption in these cases was violated and the estimator failed catastrophically. This makes perfect sense since the estimation structure of Figure 4.7 is based upon making *correct* decisions of the transmitted bits, i.e., $\hat{d}_k$ is assumed to be equal to d_k. Clearly under low SNR conditions, this assumption fails with ever higher probability.

4.2.7 Application of Open-Loop Estimation to Receivers Employing Adaptive Equalization

Many receiver architectures that employ adaptive equalization require coherent demodulation. Many equalization strategies employ the principle of rapid adaptation in the attempt to create the optimal filter for an arbitrary and rapidly changing channel environment. It

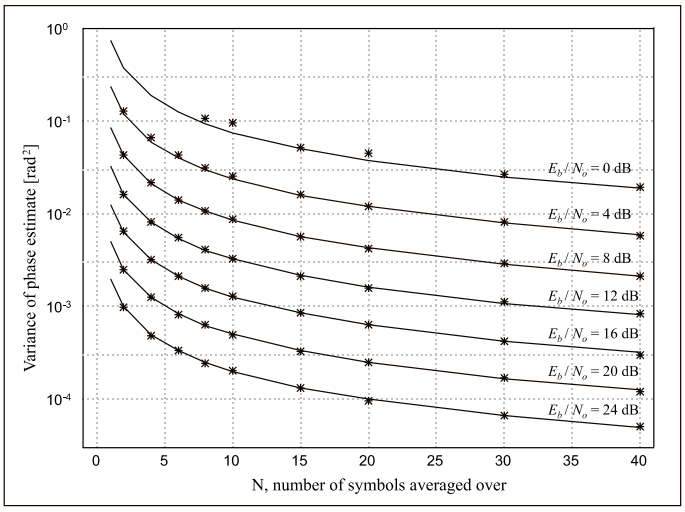

Figure 4.10: Variance of output phase estimate of first-order phase estimator, using squaring operation, for a variety of E_b/N_o. Lines denote theoretical performance predicted by (4.52), asterisks denote simulation points

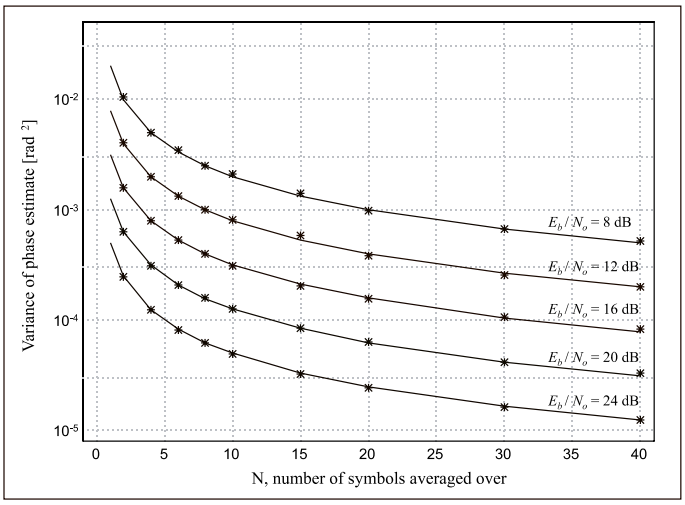

Figure 4.11: Variance of output phase estimate of first-order phase estimator, using decision feedback, for a variety of E_b/N_o. Lines denote theoretical performance predicted by (4.68), asterisks denote simulation points

is as yet quite unclear how equalization schemes interact with closed-loop carrier recovery.

Consider, for example, the steepest descent algorithm defined in the normalized least mean squares (NLMS) update equation

$$\mathbf{w}_{k+1} = \mathbf{w}_k + \frac{\mu e_k^*}{\mathbf{x}_k^H \mathbf{x}_k + \delta}\mathbf{x}_k \tag{4.76}$$

where $\mathbf{x}_k = (x_k, x_{k-1}, \cdots, x_{k-N+1})^T$ is a vector of current and previous input samples to the filter $\mathbf{w}$ of length N, $e_k = d_k - r_k$ is the filter error at time k, $r_k = \mathbf{w}_k^H \mathbf{x}_k$ and d_k is the desired symbol or an estimate thereof, μ is an update constant between 0 and 2.0, δ is a small constant to avoid division by zero, ^{H} is the Hermitian transpose operator, and $\mathbf{w}_k$ is an iterative solution to the well-known Wiener-Hopf equation

$$\mathbf{w}_{opt} = \mathbf{R}_{xx,k}^{-1}\mathbf{p}_k \tag{4.77}$$

where $\mathbf{R}_{xx,k}$ is the autocorrelation matrix of the input samples, $\mathbf{x}_k$, and $\mathbf{p}_k$ represents the correlation of the input vector to the desired symbol.

The NLMS update is sensitive to the phase of the error e_k and therefore will, as we might expect, attempt to correct for a residual phase offset in the input signal constellation. In fact, assuming *perfect frequency* coherence, i.e., zero residual frequency offset, the performance of the equalizer updated with (4.76) will perform as well (in AWGN) with or without a coherent *phase* estimate. The performance quickly degrades, however, in the presence of even small frequency residuals. We would therefore be inclined to include coherent carrier recovery when implementing this type of receiver. The problem is that coherent carrier recovery will also attempt to correct for the instantaneous phase seen by the receiver. The interaction between these two feedback mechanisms is, at best, unclear and has been observed in simulation to produce catastrophic failure of the equalization system, and in bit error performance thereby.

One solution to this problem is to employ adaptive equalization with open-loop carrier recovery, thereby avoiding this possibly pathological dual feedback effect. Figure 4.12 is a special case of the structure proposed by [51] where we consider coherent demodulation of BPSK with updates supplied to the filter weights at the symbol rate. This structure, however, imposes a vitally important change on the update equation. The input vector, used as a reference for the update, must also be *rotated* by the phase estimate. Specifically we require

$$\mathbf{w}_{k+1} = \mathbf{w}_k + \frac{\mu e_k}{\mathbf{x}_k^H \mathbf{x}_k + \delta} \cdot e^{-j\hat{\theta}_{ML}} \cdot \mathbf{x}_k \tag{4.78}$$

for the update. Note that for the case of BPSK signalling the error term is no longer considered to be complex because the expected phase of the rotated decision statistic is

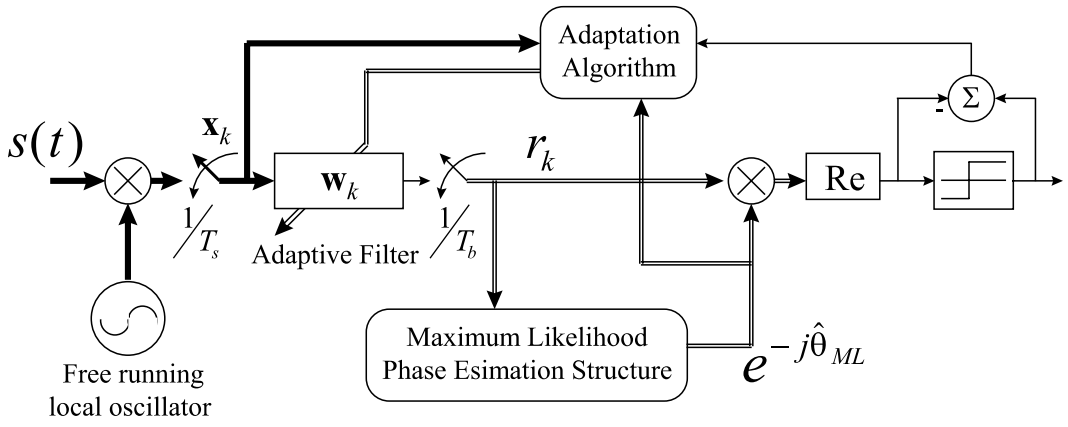

Figure 4.12: Open loop carrier estimation applied to an adaptive equalization receiver, shown here employing decision direction only. This structure was adapted from [51] for this research

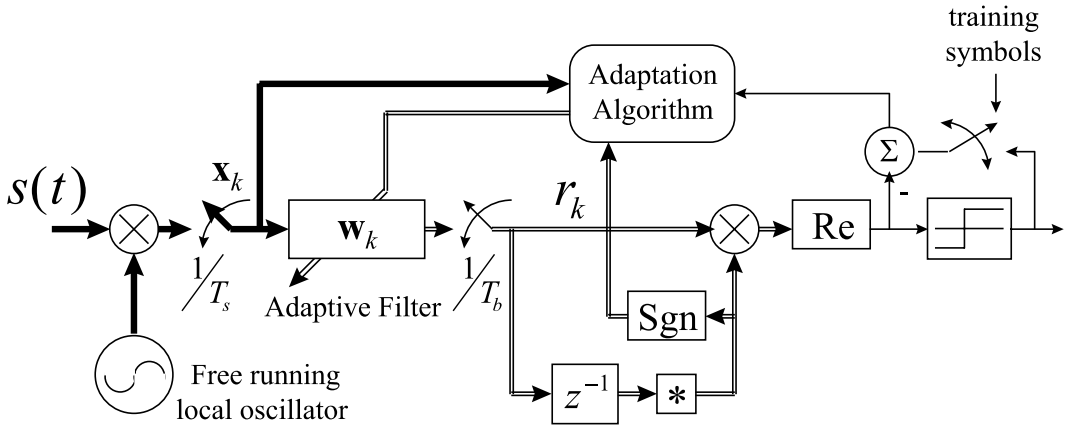

Figure 4.13: Differentially coherent receiver employing adaptive interference suppression for BPSK—a limiting condition of ML phase estimation

zero. Therefore, we no longer expect any useful information in the imaginary part of the error. In fact, simulation studies have shown a marked performance improvement gained by using only the real part of the error versus the complex error. This makes sense since we are effectively eliminating one-half of the noise in the error statistic that is fed back into the adaptation equation. This naturally improves the performance of the adaptive filter. Simulations have shown this structure of Figure 4.12 to work well when combined with fractionally-spaced, adaptive equalization routines for CDMA systems. These results are discussed later in Chapters 6 through 8.

A very important extension of the application discussed in this section is toward utilizing equalization within a differentially coherent receiver. In fact, a differentially coherent receiver may be viewed as a limiting case of the ML phase estimator, namely that of $N = 1$, wherein the previous symbol is used as the phase reference for the current one. This suggests the demodulator structure given in Figure 4.13, which was developed independently as part of this research effort. Note that now, the estimated phase present in (4.78) is replaced with the complex sign of the previous symbol so that the update equation becomes

$$\mathbf{w}_{k+1} = \mathbf{w}_k + \frac{\mu e_k}{\mathbf{x}_k^H \mathbf{x}_k + \delta} \cdot \text{Sgn}\,(r_{k-1}^*) \cdot \mathbf{x}_k \; . \tag{4.79}$$

Note that the use of the sign function eliminates the one-half of noise power present in the previous symbol estimate.

4.3 Chapter Summary

Thus concludes the discussion of phase-coherent carrier recovery techniques. Again the interested reader is urged to consult the many references cited in this chapter as well as in Chapter 3. Some of the relative merits of the carrier recovery schemes presented in this chapter are explored later in Chapter 6. One additional portion of background material is yet to be explored, the concept of automatic frequency control (AFC), which, for the purposes of this research concerning PSK signalling, will be viewed as an acquisition aid to phase-coherent structures. As such, this serves as a motivation for the topic of the next chapter.

Chapter 5

Automatic Frequency Control

Automatic frequency control* may be applied to carrier recovery either as an acquisition aid to phase coherent loops, such as a Costas loop for coherent PSK demodulation, or as a non-coherent carrier tracker for differentially coherent PSK. In the former class of receivers, AFC becomes especially important in time division multiple access (TDMA) schemes, where the communication is of a bursty nature and quick synchronization is required to preserve bandwidth.

We note that the theory surrounding AFC loops, especially pertaining to their performance in noise, is much less mature than that for PLLs. Further, since an AFC loop is a non-coherent device, the notion of phase jitter, applied universally as a figure of merit to phase-coherent tracking loops, has no meaning whatsoever in the discussion of AFC. In fact, an AFC loop will not in general settle to any particular phase relationship with the input carrier but will randomly "walk" in phase, as it is perturbed by noise, with reference to the input carrier. This behavior may be seen, for example, in Figure 5.7(A). A notion of *frequency jitter* can be applied to AFC as a figure of merit, but the relationship of frequency jitter and phase jitter is, at best, unclear. We therefore find it difficult to compare AFC loops with the coherent tracking loops on the steady-state figures of merit established in Chapter 3. Therefore, only acquisition time will be of primary interest. In section 5.4, where we directly incorporate AFC as an aid to a Costas loop, we consider only the *degradation* of the steady-state phase variance over that which was expected due the presence of the AFC in the loop. Since no theory presently exists to predict this degradation, we appeal primarily to simulation results as well as heuristic arguments in the discussion.

*Gardner in [27] makes a distinction between frequency-tracking loops (FTLs) and automatic frequency control (AFC), stating that an AFC loop employs a "conventional" frequency discriminator. While this reference is one of the very best and most commonly cited on the subject, this distinction is not employed by other authors, nor aparently is this limited definition of AFC widely subscribed. We therefore make no such distinction in this work.

5.1 Introduction to AFC

AFC loops bear striking similarities to PLLs. The only major difference between them and the variety of control loops discussed thus far in Chapters 3 and 4 is the exchange of a phase detector (PD) with a *frequency difference detector* (FDD). In section 5.2, we devote some attention to the design of an FDD for the purposes of carrier recovery. Consider it for the moment, however, to be simply a "black box" whose output is proportional to the frequency difference, $\Delta\omega = \omega_i - \omega_o$, between the input carrier and the locally generated reference. We then may view the AFC in the frequency domain as the linearized structure shown in Figure 5.1. Note that the VCO, modeled as an integrator in the phase domain, is now modeled simply as a gain in the frequency domain. The closed-loop transfer function of the AFC loop, relating the input frequency, ω_i, to the estimated frequency, ω_o, is thus given by

$$H_{AFC}(s) = \frac{\Omega_o(s)}{\Omega_i(s)} = \frac{K_f K_o H_f(s)}{1 + K_f K_o H_f(s)} \tag{5.1}$$

where K_f is the gain of the FDD, analgous to K_d the gain of a phase detector, K_o is, as defined before, the gain of the VCO, $\Omega_i(s) = \mathcal{L}\{\omega_i(t)\}$, $\Omega_o(s) = \mathcal{L}\{\omega_i(t)\}$, the Laplace transforms of the instantaneous input and output frequencies respectively, and $H_f(s)$ is the transfer function of the loop filter.

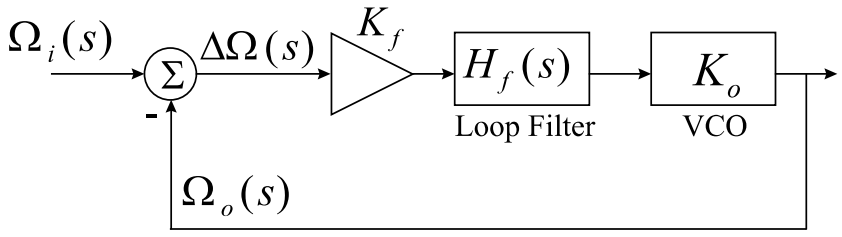

Figure 5.1: Linearized, frequency domain model of AFC loop.

In order to simplify the on-going discussion, we utilize the second-order loop filter proposed in [27] defined by

$$H_f(s) = \frac{1}{s\tau_1\,(s\tau_2 + 1)} \tag{5.2}$$

where time constants τ_1 and τ_2 are carefully chosen to cause the poles of the loop filter, $H_f(s)$, to coincide with the poles of the closed-loop transfer function, $H_{AFC}(s)$. Note that this filter is not shown to be optimal in any sense but is simply suggested to be more effective in supressing noise than one with a single pole. Specifically, define τ_L to be the

time constant of the loop. Then choose

$$\tau_1 = K_f K_o \tau_L \quad \text{and} \quad \tau_2 = \frac{1}{4}\tau_L \, . \tag{5.3}$$

These convenient definitions lead to a closed-loop transfer function of

$$H_{AFC}(s) = \frac{1}{\left(\frac{1}{2}\tau_L s + 1\right)^2} \, . \tag{5.4}$$

It is further shown in [27] that the loop noise bandwidth, B_L, for a loop so constructed, is $B_L = \dfrac{1}{4\tau_L}$, which allows us to conveniently rewrite the transfer function in terms of that single design parameter

$$H_{AFC}(s) = \frac{1}{\left(\frac{1}{8B_L} s + 1\right)^2} \, . \tag{5.5}$$

Relatively complicated theoretical results for the frequency estimate variance due to AWGN, given the transfer function in (5.5) and the balanced quadricorrelator (BQ) frequency difference detector (FDD), introduced in section 5.2, are given in [27]. We point the interested reader to this excellent reference, and do not repeat the results here in the interests of brevity.

To continue our emphasis on discrete-time implementation, which began in Chapter 3, we wish to find the digital loop filter, which, when implemented using digital devices or in software on a digital computer, will obtain equivalent loop performance to the continuous-time model. Direct application of the BZT to (5.5) yields,

$$H_{AFC}(z) = \frac{1 + 2z^{-1} + z^{-2}}{\left[\left(\frac{1}{4B_L T}\right)^2 + \frac{1}{2B_L T} + 1\right] + \left[-2\left(\frac{1}{4B_L T}\right)^2 + 2\right] z^{-1} + \left[\left(\frac{1}{4B_L T}\right)^2 - \frac{1}{2B_L T} + 1\right] z^{-2}} \tag{5.6}$$

where T is the sampling interval in [sec]. The discrete-time loop filter is thus found by

$$H_f(z) = \frac{1}{K_f K_o} \cdot \frac{H_{AFC}(z)}{1 - H_{AFC}(z)} = \frac{b_{f,0} + b_{f,1} z^{-1} + b_{f,3} z^{-2}}{1 + a_{f,1} z^{-1} + a_{f,3} z^{-2}} \tag{5.7}$$

where, defining $\alpha_o = \left(\dfrac{1}{4B_L T}\right)^2 + \dfrac{1}{2B_L T}$,

$$\begin{aligned} b_{f,0} &= \frac{1}{\alpha_o K_f K_o} & \qquad a_{f,1} &= \frac{1}{\alpha_o}\left[-2\left(\frac{1}{4B_L T}\right)^2\right] \\ b_{f,1} &= \frac{2}{\alpha_o K_f K_o} & & \\ b_{f,2} &= \frac{1}{\alpha_o K_f K_o} & a_{f,2} &= \frac{1}{\alpha_o}\left[\left(\frac{1}{4B_L T}\right)^2 - \frac{1}{2B_L T}\right] \, . \end{aligned}$$

So the modeling of the loop filter for AFC is complete. Now what remains is determination of the structure required to produce $\Delta\Omega(s)$ shown in Figure 5.1. This motivates a discussion of the design and implementation of FDDs.

5.2 Frequency Difference Detectors

Several discussions in the relevant literature concerning FDDs begin with the *quadricorrelator*. Such a device is basically a simple Costas loop with a differentiator in the I-arm. These produce an error term that is proportional to the frequency difference between the input carrier and the local reference. The interested reader is urged to review [28], [29], and [27] for introductory material regarding this type of FDD. Due to the ripple voltage created, simple quadricorrelators are not suitable for FM demodulation, nor are they advantageous for PSK demodulation. For this reason, we skip directly to a discussion of the *balanced quadricorrelator* (BQ) as a starting place for the discussion of FDDs.

5.2.1 The Balanced Quadricorrelator

Consider, for the moment, an unmodulated, noiseless carrier $s(t)$ applied to the input of the BQ shown in Figure 5.2,

$$s(t) = A\cos(\omega_i t + \theta_i) \tag{5.8}$$

where $A = \sqrt{2P}$ is the amplitude, ω_i is the carrier frequency, and θ_i is a random phase shift induced to the carrier. Note that now we take the phase of the carrier, relative to the reference, to be constant and allow the frequency difference to be time varying, whereas in the discussion of phase-coherent tracking, we assumed just the opposite. This signal is then downconverted in quadrature by the reference signals as shown with frequencies equal to ω_o and amplitudes defined for convenience to be $2K_o$. Assume further that the low pass filters of Figure 5.2 are ideal, completely supressing the double frequency terms. Then

$$v_i(t) = AK_o\cos(\Delta\omega t + \theta_i) \quad \text{and} \quad v_q(t) = AK_o\sin(\Delta\omega t + \theta_i) \tag{5.9}$$

where $\Delta\omega = \omega_i - \omega_o$ is the frequency difference between the input and reference carriers. Differentiators are used in both arms with gains equal to τ_d, yielding

$$\dot{v}_i(t) = -AK_o\Delta\omega\tau_d\sin(\Delta\omega t + \theta_i) \quad \text{and} \quad \dot{v}_q(t) = AK_o\Delta\omega\tau_d\cos(\Delta\omega t + \theta_i)\ . \tag{5.10}$$

The difference, the error signal for the AFC loop, is thus given by

$$v_d(t) = -A^2K_o^2\Delta\omega\tau_d \tag{5.11}$$

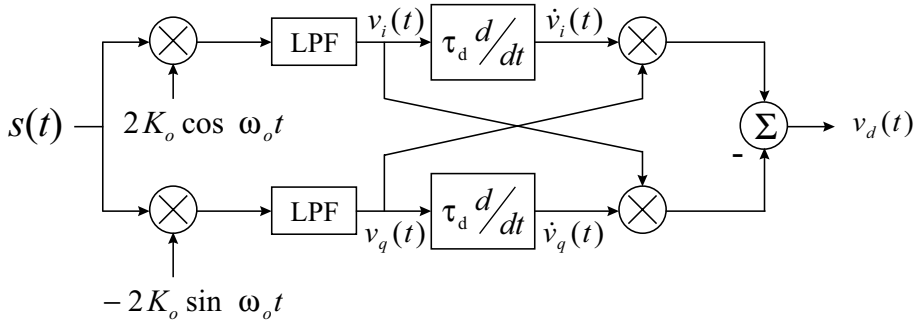

Figure 5.2: Block digram of continuous-time balanced quadricorrelator (BQ).

which is directly proportional to the frequency difference.

Now consider an arbitrary bandpass signal $s(t)$ of the form

$$s(t) = x(t)\cos\omega_i t - y(t)\sin\omega_i t \, . \tag{5.12}$$

The error control signal $v_d(t)$ is now given by

$$v_d(t) = -K_o^2 \tau_d \left[\Delta\omega \left(x^2 + y^2\right) + x\dot{y} - y\dot{x}\right] \tag{5.13}$$

where now an implicit dependence upon time is assumed for $x(t)$, $y(t)$, $\dot{x}(t)$, and $\dot{y}(t)$. Insight into (5.13) may be gained by considering a noiseless BPSK signal in which $x(t) = Ad(t)\cos\theta$ and $y(t) = Ad(t)\sin\theta$ where $d(t) \in \{\pm 1\}$. In this case, (5.13) simplifies back down to (5.11), yielding a time averaged value for $v_d(t)$ of

$$\overline{v_d(t)} = -A^2 K_o^2 \tau_d \sigma_d^2 \Delta\omega \tag{5.14}$$

where $\sigma_d^2 \triangleq E\left[d^2(t)\right] = 1$. This suggests that, unlike the PLL fitted with a conventional multiplier phase detector, the AFC loop fitted with a BQ does in fact form a suitable *tracking device* for BPSK signals, granting, of course, that it cannot provide a coherent phase reference. Further consider the signal in which $E\left[x(t)y(t)\right] = 0$, which is true of all PSK waveforms modulated with uncorrelated input data bits. The BQ output signal can be shown to be

$$\overline{v_d(t)} = -K_o^2 \tau_d \Delta\omega \left(\sigma_x^2 + \sigma_y^2\right) \, . \tag{5.15}$$

We note that while the BQ is a suitable FDD for MPSK signalling, it cannot, like the discrete-time PLL proposed in Chapter 3 or the Costas loop proposed in section 4.1.4, be implemented digitally via baud rate sampling. The $360^o/M$ discontinuities from sample to sample in such a system cause simply too much jitter for the loop to acquire properly.

Due to this, we restrict the application of the BQ to analog FDD implementations only. Therefore we look for an alternative FDD structure suitable for baud rate implementation. A robust and simple to understand example of such a structure is angle-doubling AFC.

5.2.2 Angle Doubling AFC

It is worth noting that many FDDs can be proposed that are suitable for baud rate digital implementation—the only absolute requirement being the necessity for an odd symmetry of the error response to a frequency difference and the ability of the loop to remove the modulation in the signal. The richest known coverage of digital FDDs may be found in [26], which, though in our opinion it lacks sufficient justification for many of the results presented, is still widely regarded as an important seminal paper on the topic of AFC, especially as it relates to carrier recovery for digitally modulated signals and digital components. We mention one structure proposed therein, viz., angle doubling AFC (ADAFC), particularly as it serves to provide 1) an example of an FDD structure suitable for baud rate implementation and 2) a motivation for the application of the AFC loop for an acquisition aid to a Costas loop.

Consider the BPSK signal defined by

$$s(t) = Ad_k \cos(\omega_i t + \theta_i) \tag{5.16}$$

where A, ω_i, and θ_i are as defined in (5.8) and d_k is the data bit at time $t = kT_b, d_k \in \{\pm 1\}$. Once again, assume the down conversion process and lowpass filters are ideal. Thus the quadrature samples may be represented as

$$i_k = AK_o d_k \cos(\Delta\omega k T_b + \theta_i) \quad \text{and} \quad q_k = AK_o d_k \sin(\Delta\omega k T_b + \theta_i) \tag{5.17}$$

where, as before, $\Delta\omega = \omega_i - \omega_o$, the frequency difference between the input and local reference carriers. Then

$$x_k = i_k^2 - q_k^2 = A^2 K_o^2 \cos(2\Delta\omega k T_b + 2\theta_i) \tag{5.18}$$

and

$$y_k = i_k \cdot q_k = \frac{1}{2} A^2 K_o^2 \sin(2\Delta\omega k T_b + 2\theta_i) \tag{5.19}$$

where, as expected, the modulation had been removed in these control signals. It is important to point out here that, with the exception of hard-limiting in the I-arm, y_k precisely represents the phase error signal for a Costas loop. To emphasize this fact, y_k is also denoted $e_{\phi,k}$ in Figure 5.3.

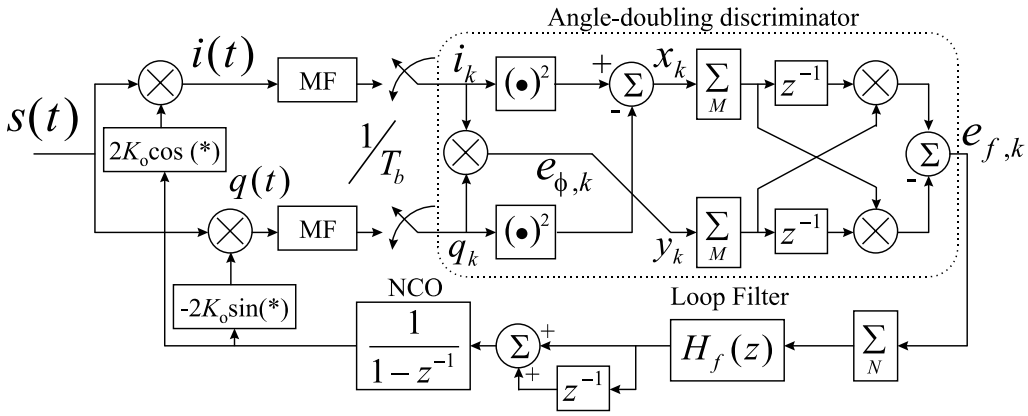

Figure 5.3: Block digram of discrete-time implementation of Angle-doubling AFC (ADAFC) proposed in [26].

Now the generalized structure of Figure 5.3 as proposed by [26] includes summers both for the inputs to the discriminator and to the input of the loop filter $H_f(z)$. Clearly these summers could be used to perform some sort of short term averaging for the purpose of noise supression. We choose, for the purposes of this discussion, to move noise suppression considerations into the design of the quadrature matched filters as well as that of the loop filter and take, for the sake of simlicity, $M = N = 1$. Then the error signal out of the discriminator becomes

$$e_{f,k} = x_{k-1} \cdot y_k - x_k \cdot y_{k-1} = \frac{1}{2} A^4 K_o^4 \sin(2\Delta\omega T_b) \ . \tag{5.20}$$

Thus ADAFC provides a sinusoidal frequency error characteristic, similar to the phase error characteristic of a PLL or Costas loop. This is a fundamentally different result than obtained from the BQ, which was completely linear. Nevertheless, under the fairly easy assumption that $\Delta\omega$ is less than about $\frac{1}{10}$ of the baud rate, i.e., $\Delta\omega < 0.1/T_b$, we may approximate this error as

$$e_{f,k} \approx A^4 K_o^4 2\Delta\omega T_b \tag{5.21}$$

which, with the exception of a sign difference which must be taken into account, bears striking similarity to the frequency error produced by the BQ in (5.11) for an unmodulated input signal.

Finally, to complete the design of the loop shown in Figure 5.3, we include the loop filter, $H_f(z)$, for which the design proposed in section 5.1 would be appropriate. We include also the NCO, modeled once again as a simple phase accumulator. Note the addition of a two sample summation at the input of the NCO. This is used simply to place a zero at

$z = -1$, which is lost upon modeling the NCO as an accumulator versus a strict integrator. Obviously, the presence of this zero at $f = R_b/2$[Hz] would provide some additional noise immunity for the loop.

5.3 Acquisition Time of AFC loops

As mentioned at the beginning of this chapter, no theory presently exists to predict the aquisition behavior of AFC loops, much less the acquisition time. Before moving on to a singularly important application of AFC loops in section 5.4, we believe it is appropriate to show the type of behavior that might be expected from them. To do this, we appeal strictly to simulation results to suggest *typical* performance in this all-important matter of acquisition time.

Figure 5.4 is our attempt at showing the type of acquisition times to be expected relative to a conventional phase-coherent tracking loop. Here acquistion time, in samples, is plotted versus the normalized loop bandwidth of the respective loops. Normalization is with respect to the initial frequency offset, $f_{off} = \frac{1}{2\pi}\Delta\omega(0)$, of an unmodulated, noiseless carrier, which served as the input to the systems in this example. It is important to note that two different initial offsets were used, however. The initial offset for the AFC loop was set to be $10^{-1}R_b$, whereas for the Costas loop, it was set to be $10^{-2}R_b$ because the Costas loop literally could not capture the carrier at $10^{-1}R_b$ offset. Also note that the AFC loop fails utterly for sufficiently large loop bandwidths, denoted $B_{L,f}$. We could not obtain a result for acquisition when $B_{L,f}$ was greater than $10^{-1}R_b$. We believe this behavior would not necessarily be true for analog implementations of AFC loops. Nevertheless, we felt that acquisition times approaching 10 samples were sufficient for this illustration. Acquisition time in each case was defined as the sample beyond which the frequency error of the respective loop was less than $10^{-3}R_b$.

The most notable aspect of Figure 5.4 is that acquisition time appears to be log-linear for both types of loops. For the AFC loop, the slope is negative one except as the acquisition time begins to get quite small. From this we may postulate, in the absense of theory, that acquisition time is inversely proportional to AFC loop bandwidth for frequency offsets larger than the said bandwidth. For the Costas loop, on the other hand, the slope is steeper than -3 for all of the obtainable points. This suggests that for a phase-coherent loop, the frequency acquisition period is inversely proportional to the *cube* of loop bandwidth.

These intuitive results allow us to further suggest overarching principles in the design of the receiver for digitally phase modulated signals. For a fixed Costas demodulator loop bandwidth, $B_{L,c}$, (fixed perhaps by the constraint of allowable phase jitter), we expect

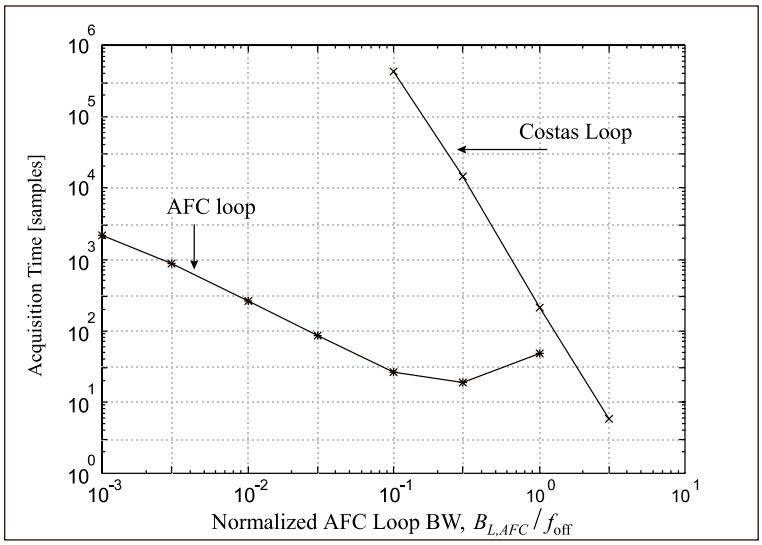

Figure 5.4: Simulated acquisition time in samples for BQ-AFC and Costas loops versus normalized loop bandwidth of respective loops; $*$ mark simulation points for AFC loop; $\times$ mark simulation points for Costas loop.

rapid frequency acquisition when the frequency uncertainty (initial offset) is less than or approximately equal to $B_{L,c}$. Under such conditions, there is little or no motivation to implement AFC. If the uncertainty is larger than this, however, the Costas loop runs the risk of requiring an exponentially increasing length of time to acquire the input frequency, and an AFC loop or some other acquisition aid ought to be employed to assist the Costas demodulator. This is the subject of the next section.

5.4 Costas Loops with AFC-Aided Acquisition

There are a variety of methods to aid a Costas loop with frequency acquisition when the uncertainty is large. One way is to perform a "slow" frequency sweep of the local oscillator until the Costas loop acquires. The implementation of such a scheme is highly dependent upon the design constraints of a particular receiver, and, since a mobile receiver might not be constructed with such a mechanism, we do not give attention to this scheme in this work. Another notion might be to utilize two different loop filters, one with a wide bandwidth and the other one narrow. At initial start up, utilize the wider bandwidth filter and then, upon detection of course acquistion, switch to the narrower bandwidth filter for tracking mode. It might be added that an AFC loop could also be utilized in place of the wider bandwidth Costas loop in this scheme. The notion of switching between two loops is a rather simple

one. Gauging the performance of such a scheme amounts quite simply to examining the performance of two different loops, which has already been accomplished in this chapter and in Chapter 4. For this reason, we do not give additional attention to this strategy in this work. A final approach, however, might be to combine the AFC and Costas loop into one single feedback structure. This is an interesting approach and one that we explore in some depth in this section. In section 5.4.1, we first describe the proposed combined carrier recovery structure. Then in section 5.4.2, we examine the very crucial impact of the combined structure on phase jitter, which is *the* important figure of merit for coherent carrier recovery.

5.4.1 Description of Combined Costas Demodulator with AFC for Acquistion Aiding

Consider, for the moment, the heuristically motivated system in which a PD and an FDD are both incorporated into a carrier recovery loop as shown in Figure 5.5. Such a scheme was proposed as early as 1977 in [28], wherein we merely sum the filtered error outputs of the two detectors. Intuitively this ought to work. During acquisition under the conditions of a large frequency uncertainty, the Costas loop portion will produce a wildly oscillating phase error, $e_\phi(t)$. Upon filtering with the quite narrow Costas loop filter, $F(s)$, this error will not contribute significantly to the integration performed by the VCO. The frequency error, $e_f(t)$, on the other hand, will start out large and have a strong DC component, assuming the FDD is constructed properly. Thus this error signal will dominate during the acquisition period and, as the AFC portion was designed to do, bring the frequency error down close to zero very rapidly. As the frequency error gets small, say less than the closed loop bandwidth of the Costas portion, $e_f(t)$ will become small, $e_\phi(t)$ will begin to dominate, thus acquiring the phase, and VCO output will coherently track the input signal $s(t)$.

Extending this intuitively satisfying structure to discrete-time, baud rate implementation is outlined in Figure 5.6. Here we utilize the basic Costas loop structure with hardlimited I-arm as the PD. The digital loop filter, $F_2(z)$, defined for instance by (3.17), would be an appropriate choice. For the FDD, we choose to implement ADAFC as discussed in section 5.2.2. A loop filter, $H_f(z)$ as defined by (5.7) would form another appropriate choice. Note, once again, that we keep the two-term summation at the output of the AFC loop filter to preserve that high frequency zero at $z = -1$, which was lost in modeling the NCO as an ideal accumulator instead of an ideal integrator.

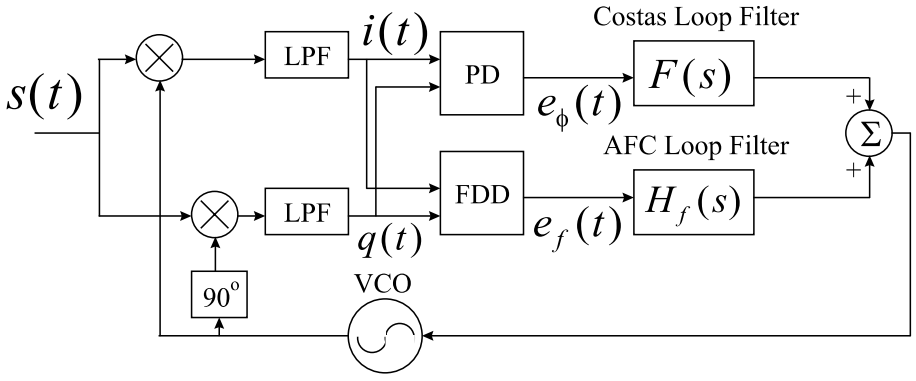

Figure 5.5: Receiver block diagram suggesting the combination of AFC with a Costas Loop.

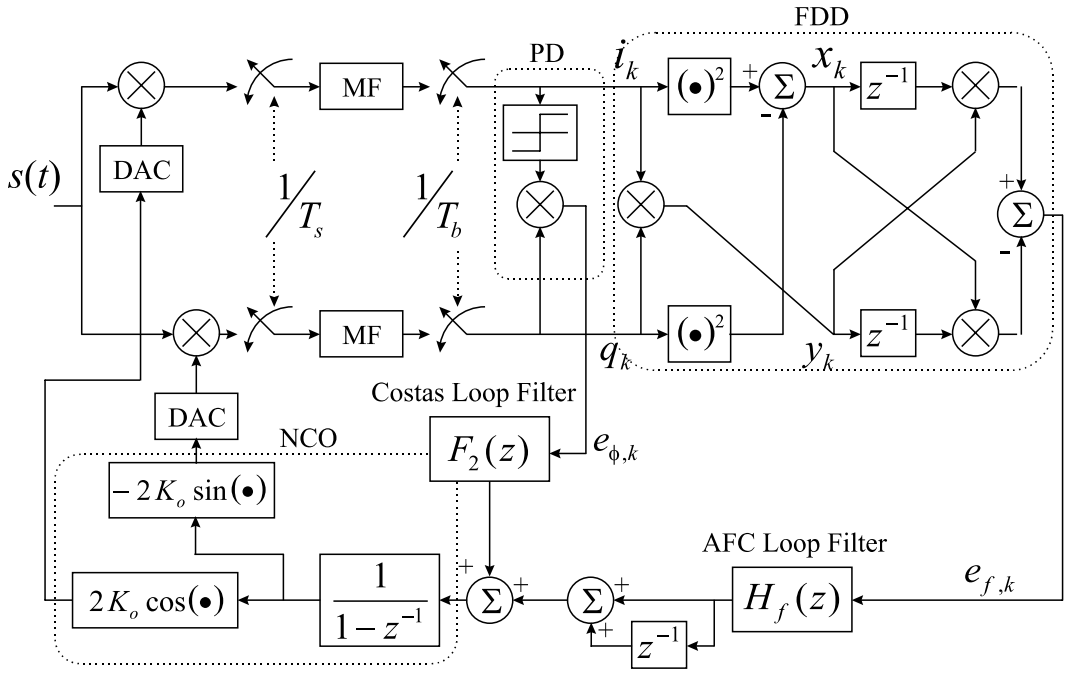

Figure 5.6: Block diagram of discrete-time implementation of second-order Costas demodulator with a ADAFC loop for acquisition aiding.

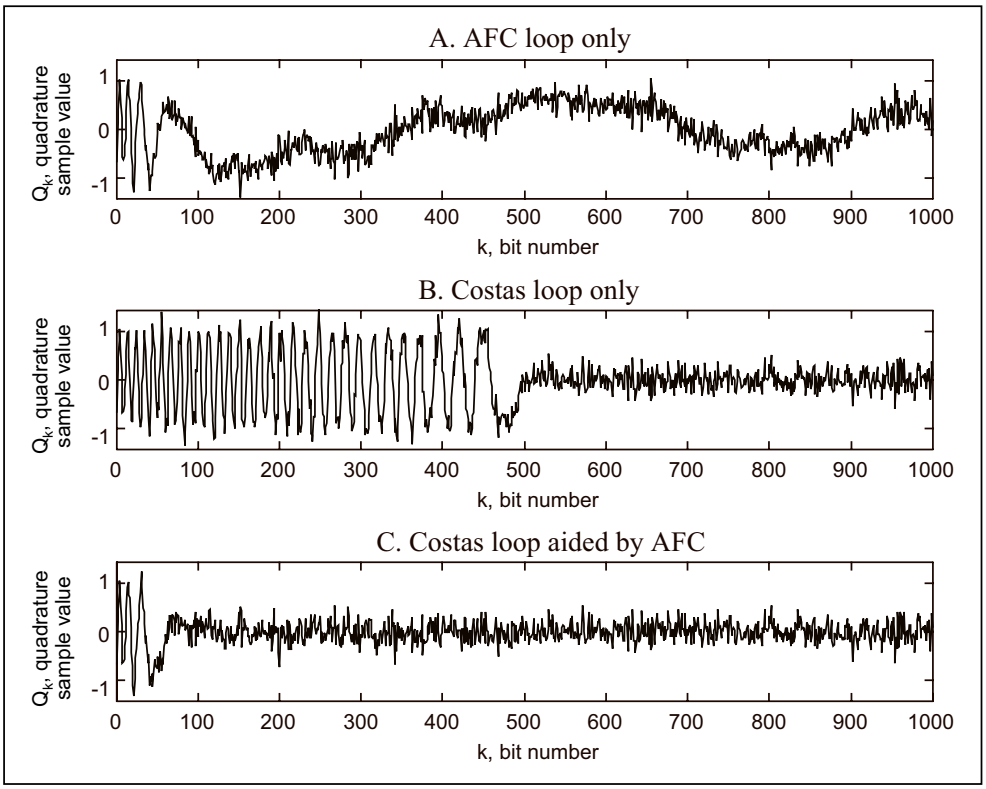

Figure 5.7: Typical acquisition behavior for three styles of carrier trackers: (A) An non-coherent AFC loop; (B) An unaided Costas loop; C. The same Costas and AFC loops combined; Input is BPSK signal with $E_b/N_o = 12$ dB.

5.4.2 Performance Issues for Combined Costas Demodulators with AFC

To give an impression of just how this type of scheme might work under realistic working conditions, we show an example of the acquistion behavior of three different types of loops in Figure 5.7. These are A) an AFC loop acting alone; B) a Costas loop acting alone; and C) the same AFC loop and Costas loop acting together as outlined in Figure 5.6. In each case, the values for the quadrature samples, q_k, are shown versus sample number, k. A BPSK modulated signal with $E_b/N_o = 12$dB is applied to each of the structures for which the initial frequency offset is set to be $10^{-1}R_b$, which is the sample rate of the carrier recovery portions of the loops. Costas loop bandwidth is $\frac{1}{20}R_b$, or one-half the initial offset, and AFC loop bandwidth is $\frac{1}{200}R_b$. Given the careful selection of these loop parameters, the combined loop was able to exploit the best features of both the Costas and AFC loops.

The quadrature sample values, q_k, were chosen to compare the performance of each loop on equal footing. For the AFC loop there is no phase error estimate, but for a Costas

loop with a hard-limited I-arm as is performed here in parts (B) and (C) of Figure 5.7, the quadrature samples are equal to the phase error samples, $e_{\phi,k}$, assuming no bit errors or equivalently a relatively high input SNR. For a phase-coherent recovery scheme, we would expect that $q_k = e_{\phi,k}$ would go to zero upon phase acquisiton for BPSK. Note that part (A) of Figure 5.7 shows just what is meant by the AFC loop being an *essentially* non-coherent device. Note that after only a couple of oscillations in the phase, the AFC loop quickly settles down but it never completely acquires phase. For this reason, even at steady-state, the phase error randomly walks around due to random noise perturbations. The frequency error is essentially zero, but since the AFC loop is not responsive to phase at all, there is no coherent phase reference being produced. These random phase perturbations can have a pathological impact on the combined loop, and this important aspect will be discussed shortly.

Now in part (B) of Figure 5.7, we see the behavior of the Costas loop acting alone. Note that since the initial offset is twice the Costas loop bandwidth, acquisition takes a relatively long time, about 500 symbols. This is possibly an unacceptably long acquisition period, and as noted in section 5.3, the Costas loop has an acquisition time that is approximately proportional to the inverse of the cube of the loop bandwidth normalized to the offset. In other words, if we had chosen a significantly larger initial offset for this example, the Costas loop might have taken orders of magnitude longer to acquire. Nevertheless, in this academic example, the Costas loop does indeed acquire and, as expected, the quadrature samples converge to a noisy zero mean process.

In part (C), we can see the effect combining these loops. The AFC loop, as expected, quickly acquires the frequency. As soon as the frequency error becomes small, well within the loop bandwidth of the Costas loop, the latter loop "takes over" and quickly acquires the phase. Note that, as in part (B), the error goes to zero mean, indicating coherent phase acquisition. The steady-state jitter in part (C) is similar to that of part (B), but there is some degradation due to the additional noise allowed in via the AFC portion of the loop. The nature of this degradation becomes the next important point to make. The loop bandwidth parameters in the foregoing example were chosen *carefully* for the given noise environment with good reason as we shall see.

What is the degradation of a Costas loop's phase estimate due to the presence of the parallel AFC loop? This is a most important question, and one that has not, to our knowledge, been explored in the refereed literature previously. Figures 5.8 and 5.9 are the results of simulations, performed as part of this research, that try to answer this question. These figures attempt to show a very complex interaction, and thus we spend several paragraphs

attempting to explain these plots.

In Figures 5.8 and 5.9, the z-axes gauge the relative difference between the phase jitter observed in simulation, including the presence of the parallel AFC loop as shown in Figure 5.6, versus that predicted by theory for the Costas loop acting alone. The theoretical values for Costas loop jitter are predicted by (4.4) or, as is the case here, with I-channel hard-limiting by (3.37), assuming sufficient input SNR. These z-axes are base-10 logarithms of the observed values of phase jitter normalized to the theoretical value. The x and y axes represent the base-10 logarithms of the Costas loop and AFC bandwidths normalized to the symbol (sample) rate respectively. A z-axis result at or near 0 means that no significant phase jitter was induced by the AFC loop. Jitter degradation equal to 1 on Figures 5.8 and 5.9 means that the AFC loop added an order of magnitude of jitter to the loop. Such a degradation may or may not be acceptable depending on a particular application. Note however, that degradations of 4 and 5 orders of magnitude represent catastrophic failure of the coherent carrier recovery scheme. In these situations, the noise allowed in by the AFC loop is dominating the performance of the combined loop. What seems to be happening is that, for AFC loop bandwidths equal to or greater than the Costas loop bandwidth, the AFC noise is causing random fluctuations in the estimated phase.[†] The Costas loop, limited by its own relatively small loop bandwidth, is attempting but utterly failing to compensate.

The behavior shown in Figures 5.8 and 5.9 is actually rather counter-intuitive. A designer might, as a first pass design of the combined loop, specify a large AFC loop bandwidth to obtain rapid frequency acquisition and specify a narrow Costas loop bandwidth since the expected frequency error will then be small. These figures show categorically that "it doesn't work that way!" In fact for a given AFC loop bandwidth, say $10^{-3}R_b$ in Figure 5.8, the resulting phase jitter, given a Costas loop bandwidth of $10^{-3}R_b$, is actually much worse than if we chose a Costas loop with a bandwidth of 10^{-1}. In fact, what has happened in this case is, as we described above, a complete loss of phase coherence and a complete inability of the Costas loop, given its narrow bandwidth to acquire. While Figures 4.10 and 4.11 of Chapter 4 show that the phase jitter of a Costas demodulator is inversely log-linear with respect to loop bandwidth, an entirely opposite result is occuring here due to the presence of the AFC loop.

So in a combined Costas and AFC loop, careful attention must not only be given to absolute loop bandwidths for the purpose of jitter control, but attention must also be paid to make the AFC loop bandwidth only a small fraction of that of the Costas portion. Moreover, this consideration, i.e., just how small a fraction this ought to be, is also influenced by the

[†]Thus essentially defeating any real notion of steady-state phase behavior and essentially making the observation of phase jitter a meaningless statistic, except as it shows a complete loss of phaselock.

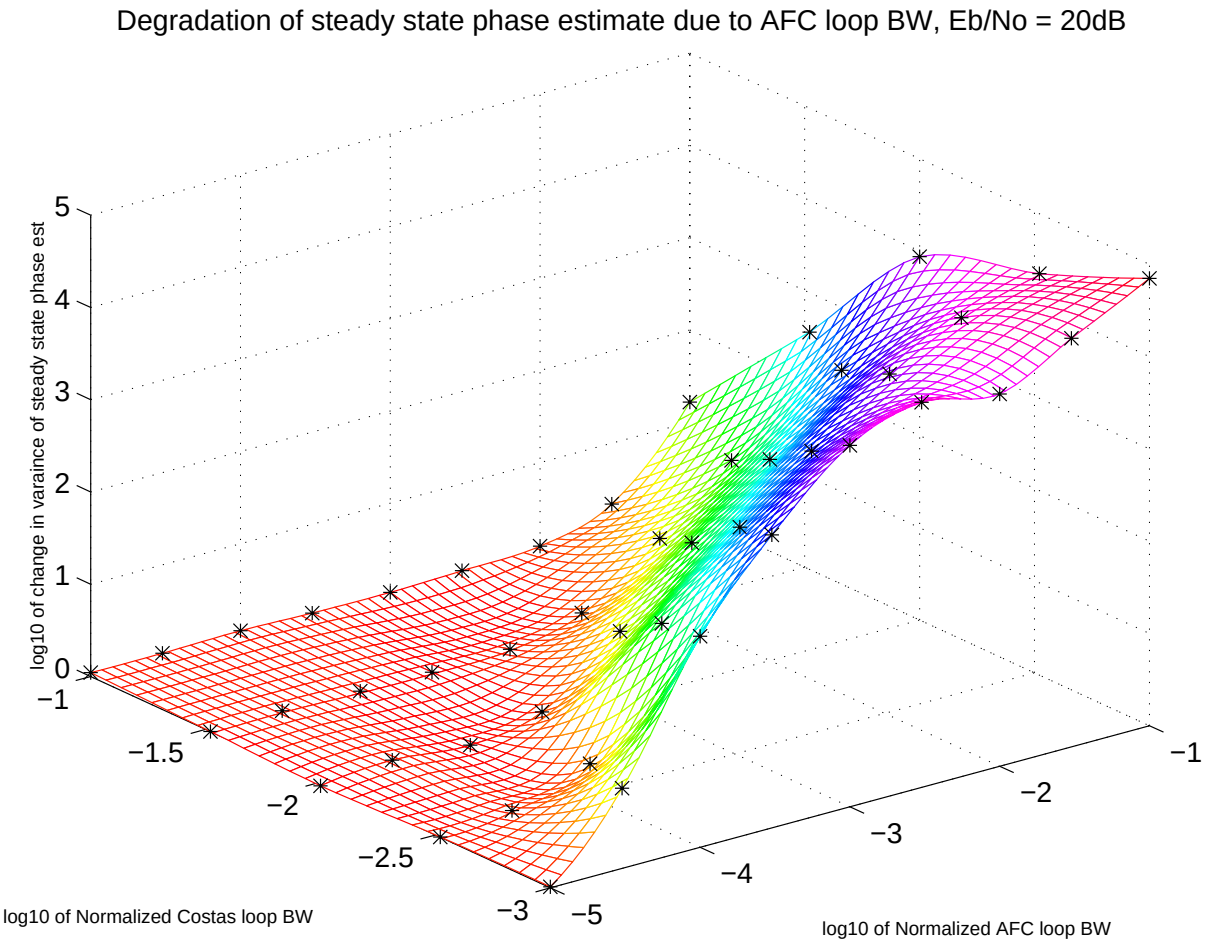

Figure 5.8: Degradation of phase output estimate for coherent carrier recovery with the addition of an AFC loop; $E_b/N_o = 20$ dB; $*$ denote simulated points; interpolation used to help show detail; all values logarithmic (base 10).

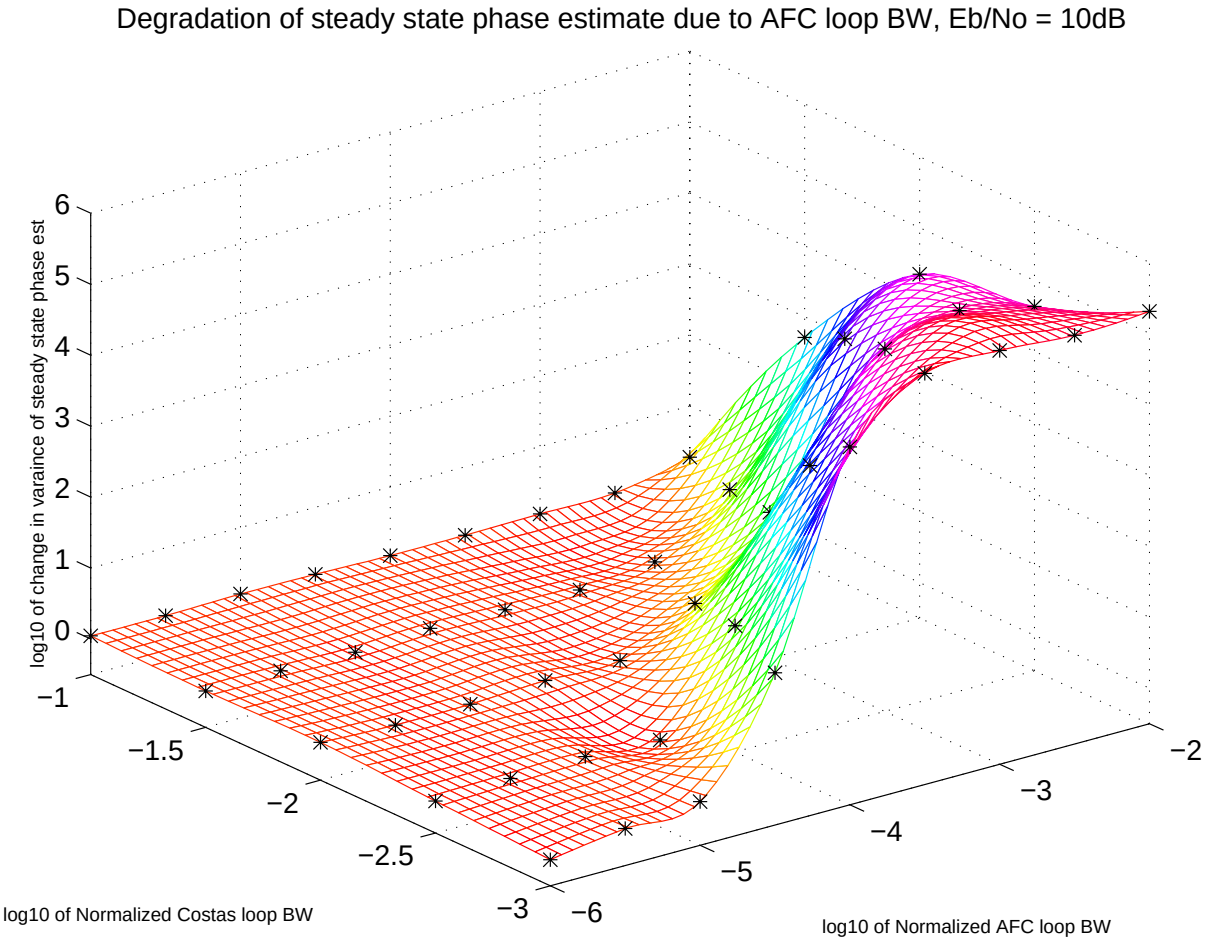

Figure 5.9: Degradation of phase output estimate for coherent carrier recovery with the addition of an AFC loop; $E_b/N_o = 10$ dB; $*$ denote simulated points; interpolation used to help show detail; all values logarithmic (base 10).

expected input SNR. Some intuition concerning this question may be gained by observing the differences between Figures 5.8 and 5.9. Note that in a relatively high SNR case, $E_b/N_o = 20$dB in Figure 5.8, there is roughly a log-linear line, parallel to the xy plane, to the left of which the AFC contributes no more than approximately an order of magnitude of degradation. This line starts around $(x = -1, y = -2)$ and ends around $(x = -3, y = -4)$. So a fundamental design constraint for the combined loop in this SNR environment would be one in which $B_{L,c}$ should be greater than or equal to 10 times $B_{L,f}$. To the right of this diagonal line we see a strong "knee" behavior, a very rapid rise in observed jitter as we scan to the right. Beyond this, the AFC contributes so much noise to the loop that it utterly fails to track phase at all.

In contrast, consider Figure 5.9 where the input SNR is a more moderate $E_b/N_o = 10$dB. We see the same behavior except that it is accentuated, i.e., after a certain point the knee behavior observed previously is now steeper. Note also that we have used a range of AFC loop bandwidths an order of magnitude smaller than in Figure 5.8, ranging from $10^{-6}R_b$ to $10^{-2}R_b$. Here the diagonal line of "acceptable" degradation runs from $(x = -1, y = -2)$ to $(x = -3, y = -5)$. So at the large bandwidth end, i.e., large Costas loop and AFC loop bandwidths, the constraint of an order of magnitude smaller AFC bandwidth still holds. But at the low end, i.e., small Costas and AFC loop bandwidths, we are now constrained to hold the AFC loop bandwidth to be two orders of magnitude smaller.

Basically the FDD operation performed in AFC circuits, which is essentially one of differentiation is a noisy process. Differentiation of a noisy signal naturally creates an even more noisy signal. Thus we have observed the overarching principle that the loop bandwidth of AFC must in general be smaller than that of a Costas loop. This is nowhere more true than when these loops operate in parallel. We must choose bandwidths for the Costas and AFC portions such that the AFC noise will not overwhelm the Costas tracking. Further, we conclude that as input SNR goes down, where we would typically choose a narrower Costas loop bandwidth to control phase jitter, the AFC bandwidth must become an ever smaller fraction of the Costas loop bandwidth. It stands to reason that at some low SNR threshold AFC loop bandwidth must of necessity become exceedingly small for such a combined loop to work properly. Nevertheless, as noted in section 5.3, the frequency acquisition time for AFC is only inversely proportional to its loop bandwidth. The Costas loop frequency acquistion time is approximately inversely proportional to the cube of its bandwidth. Given this observation, it may still be advantageous to implement AFC in parallel with Costas tracking even in receivers designed for low SNR environments. We reiterate, however, that the addition of AFC is motivated only in systems wherein the initial frequency uncertainty

is greater than the Costas loop bandwidth. In systems where the frequency uncertainty is less than this bandwidth, we can expect the Costas loop to acquire frequency and phase quite quickly on its own.

Chapter 6

Simulation Strategy

This chapter serves as a bridge between the substantive theory presented in Chapters 3 through 5 and the detailed simulation results presented in Chapters 7 and 8. Here we endeavor to describe and justify the simulation parameters and procedures. First, we briefly discuss the exchange of the figures of merit, developed in Chapters 3 through 5 for carrier recovery structures, with BER in section 6.1. Then we give a detailed outline of the PSK system under consideration in sections 6.2 and 6.3. The former describes the general system parameters as well as the fading models assumed for Chapter 8. The latter section describes the differences between the reverse and forward links assumed for this study. Finally, in section 6.4, we discuss the selection process of candidate algorithms for carrier recovery applicable to the challenges presented in sections 6.2 and 6.3. Here we present a few preliminary simulation results to help justify these selections.

6.1 BER as a Figure of Merit

In Chapters 3 through 5, we presented a variety of carrier recovery structures suitable for implementation in receivers designed to demodulate digital PSK modulated signals. In these chapters, we examined the carrier recovery performance primarily by scrutinizing acquisition time and steady-state phase jitter, noting that in general these performance measures work against each other in the design of the digital receiver.

Beginning with this chapter, we now turn our attention to arguably the most important figure of merit for the digital receiver, bit error rate (BER) or bit error probability. This proves to be convenient as we now propose to examine the wide variety of digital receivers under a wide variety of channel conditions, only the most benign of which, the additive white Gaussian noise (AWGN), single-user channel, allows a few theoretical expressions for

carrier recovery performance. So instead of continuing to examine acquisition time and steady-state phase jitter, we now take what was learned in chapters 3 through 5, apply it to the design of receivers that are optimized for lowest possible BER, and measure their effectiveness thereby.

6.2 CDMA System Overview

Based on the information provided in previous chapters, a virtually infinite number of PSK receivers might be proposed, with various loop bandwidths, for any particular channel environment. It is, however, not the intent here to present a nearly infinite number of results. Some method must be found to eliminate a large number of potential carrier recovery structures from consideration right from the start. The first step in this process is clearly defining the type of system in which we will examine the performance of receivers employing suppressed-carrier recovery.

As noted in Chapter 1, this work was from the very beginning motivated by the development of adaptive despreading algorithms for cellular CDMA systems. We noted very early in the research that the complex-weight fractionally spaced linear adaptive receiver (CW-FSLAR) examined by our colleagues in [52] and [53] performed quite poorly in the presence of even small carrier frequency offsets. Ideal coherent (unrealizable) carrier recovery had been assumed up to this point. Since this research was sponsored in part by the Defense Advanced Research Projects Agency's (DARPA's) Global Mobile Communications (GloMo) program and working prototypical adaptive radios were part of the promised deliverables, a method had to be found to make the adaptive receiver work in harsh real-world conditions. This led quickly to the development of the differentially coherent adaptive receiver outlined in Figure 4.13 in section 4.2.7. This receiver was found to be robust to frequency offsets and a variety of channel environments. Nevertheless, a nagging question remained: Is this the best we can do? Differentially coherent (DPSK) reception is well known to provide about one dB of degradation in conventional BPSK receivers. However the degradation of performance for a receiver employing adaptive equalization in a mobile, multiuser, CDMA environment was unknown. Could we "buy back" some or all of this degradation due to DPSK by employing robust carrier estimation techniques? Hence, all of the research in chapters 3 through 5 was motivated.

The purposes of this research, therefore, have been two-fold throughout:

1. discover and test carrier recovery schemes for BPSK signals that may allow coherent detection and thus buy back some of the performance penalty of DPSK,

and

2. determine whether such techniques can reliably be applied to adaptive suppression of CDMA multiple access interference (MAI).

Failure to obtain either of these will still provide a worthwhile effort in showing that DPSK is the best *realizable* system to employ in any number of particular channel environments. As we narrow down the system specifications in section 6.2.1, many of the potential carrier recovery structures possible are eliminated for one reason or another. This paring down of structures to a manageable number is discussed in section 6.4 but, as a preview, the harsh multiple access interference combined with relatively low bit energies seems to have disqualified most of the contenders. In section 6.2.2, we devote considerable discussion to the various channels of interest in this simulation work.

6.2.1 System Specifications

The general parameters for the systems that will be simulated are given in Table 6.1. Many of the parameters have been borrowed from the actual DARPA contract which sponsored this research. Simply put, this research examines a direct-sequence spread-spectrum (DSSS) multiple access system. Binary phase shift keying (BPSK) is employed with differential encoding of the data symbols and code-on-pulse spreading of length 15. Differential encoding is necessary for the differentially coherent receivers examined and also proves useful in the coherent receivers since the 180^o phase ambiguity is eliminated. Differential encoding does not automatically imply differential detection. Differentially encoded PSK can be detected coherently and thus approach the BER, P_e, of "ideal" coherent PSK, i.e., where the absolute sense of the received data is known. For this reason, we now permanently make a distinction between BPSK, "ideal" coherent 2-ary PSK, and differentially encoded BPSK (DEBPSK), a term used in [54] and elsewhere. For all simulations, the latter form of signalling is used.

The BER of BPSK in an AWGN channel is given by

$$P_e = Q\left(\sqrt{\frac{2E_b}{N_o}}\right) \tag{6.1}$$

where $Q(x)$ is the Markum Q-function defined by

$$Q(x) \triangleq \frac{1}{\sqrt{2\pi}} \int_x^\infty e^{-u^2} du \tag{6.2}$$

E_b is the bit energy usually taken to be PT_b, or the signal power integrated over a bit period, and N_o is the single-sided noise spectral density in [W/Hz]. The BER of DEBPSK

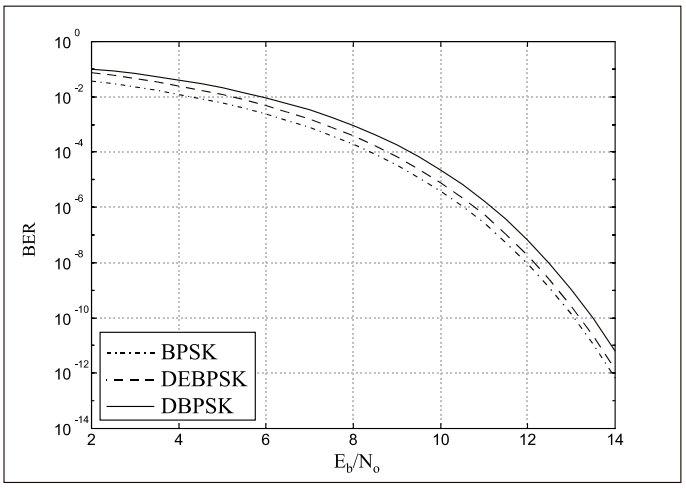

Figure 6.1: Bit error probabilities for three different binary signalling and recovery strategies

is given by

$$P_e = 2Q\left(\sqrt{\frac{2E_b}{N_o}}\right) \tag{6.3}$$

or exactly double that in the former case. This is due quite simply to the fact that in DEPSK, for any M, the receiver makes exactly two errors for every one error of ideal PSK. The factor of two increase in BER is for all practical purposes negligible. Differential detection of DEBPSK employs no coherent reference but rather the conjugate of the previous received complex-valued symbol as a reference. Since this is *presumably* a more noisy reference than that obtained by coherent reception, the system undergoes degradation in BER. This reception scheme is henceforth denoted by differential BPSK (DBPSK). The degradation, however, is very small for 2-ary signalling, as can be seen in Figure 6.1. The BER for DBPSK is given by

$$P_e = \frac{1}{2}e^{-\frac{E_b}{N_o}} \tag{6.4}$$

which is shown on Figure 6.1 as well. For higher-order modulations, such as 8-PSK or QAM, this degradation approaches 3 dB and thus provides an ever greater motivation to implement coherent carrier recovery.

Direct-sequence spreading is with length 15 Gold codes. A set of 15 such codes was constructed by taking the one maximal sequence (M-sequence) available for this length and modulo-2 adding it to its time reverse image. See [55] for the details of Gold sequence generation. When synchronized, Gold codes provide optimally low mutual cross-correlation between CDMA users, an absolute value of 1/15. When asynchronous, this cross-correlation

Table 6.1: General parameters for simulation study

System Rates:		
Carrier Frequency	f_o	= 2050 MHz
Chip Rate	f_c	= 1.92 Mcps
Bit Rate	R_b	= 128 kbps
Sample Rate	f_s	$= 2f_c = 3.84$ MSps
Other Parameters:		
Modulation		code-on-pulse DSSS, BPSK—differentially encoded data bits
Spreading Gain	G_p	= 15
Spreading Codes		set of 15 Gold codes of length 15
Code assignment		randomly assigned each Monte Carlo simulation point
Pulse shaping		none
FEC		none
Frequency Uncertainty	$2\sigma_{f,1}$	$= 1/40R_b = 3200$ [Hz] for SOI
(Gaussian dist.)	$2\sigma_{f,I}$	$= 1/20R_b = 6400$ [Hz] for SNOIs
Number of users	K	$\in \{1, 2, 4, 7, 10, 13\}$
Adaptive Filter	μ_t	= 0.5; during training
NLMS step sizes	μ_d	= 0.1; during decision direction
Key Simulation Assumptions:		
Symbol timing	assumed perfect knowledge for SOI—first 3 paths	
AGC Implementation	signal is normalized by $\sqrt{\sum_{u=1}^{U} A_u}$ where A_u is the known amplitude of user u before any fading, and U is the number of users	
Settling time	all receivers are given 100 bits to synchronize and, in the case of adaptive receivers, to train; after this time all bit errors are counted toward BER	
Observation interval	each Monte Carlo point is run for 10,000 bits; minimum of 100 Monte Carlo points per simulation	

is bounded by 7/15 and thus these codes perform no better than we might expect from random codes. Nevertheless, having the cross-correlation bounded by a known value is still convenient. This short spreading gain is not terribly close to that of IS-95 but is nevertheless quite comparable to that of spread-spectrum systems currently being deployed in the Industrial, Scientific, and Medical (ISM) bands as well as systems employing the IEEE 802.11 standard.

The chip rate, f_c, is, of course, an integer multiple, 15, times the bit rate, R_b, due to the code-on-pulse spreading with the codes described above. This rate is much higher than the throughput of IS-95 but lower than those rates specified by 802.11. It is representative for an ISM-band wireless modem. Fractionally-spaced sampling, i.e., two samples per chip,

was chosen as a benefit to the adaptive algorithms under examination. This leads to an aggregate system sample rate, f_s, of 3.84 MSps. Note that three samples per chip was chosen in [52] and [53], previous works on this subject. The selection of two samples reflects an attempt to reduce the DSP processing burden in real-time implementation of the systems proposed by this work.

The carrier frequency, f_o, of the system was chosen to be 2050 MHz, a band in which the MPRG has an experimental license. Note that this is considerably higher than that of US or European cellular systems, but it quite comparable to PCS systems now being deployed as well as the 2400 MHz ISM-band. Since the simulations are carried out using complex-baseband signal representation, the only affect f_o has on the system is in the Doppler frequency, f_d, utilized in the fading models discussed in section 6.2.2 and in determining "reasonable" frequency uncertainties observed at baseband, which we discuss here.

The frequency uncertainty, described by $2\sigma_{f,1}$ for the SOI and $2\sigma_{f,I}$ for the SNOIs in Table 6.1, is assumed to be a Gaussian random variable distributed with zero mean and variance σ_f^2. The quantity $2\sigma_f$ is then equal to two standard deviations and sets an approximate upper limit on the randomly generated frequency uncertainty, expected at any particular Monte Carlo simulation point. The values chosen for $2\sigma_f$ are reasonable for modest-priced oscillators that might be used in a mobile receiver. Consider an oscillator with a specified frequency stability of 1 part per million (ppm). At 2050 MHz, this corresponds to a residual baseband offset of 2050 kHz, which is approximately equal to $1/60R_b$ in the simulations. We express the offset in terms of R_b since the processing for *all* of the receivers considered is implemented at the baud rate. Consider, now a cellular CDMA signal at 900 MHz with the same oscillator, producing a baseband offset of 900 Hz. At an encoded symbol rate of about 25 kHz, suitable for voice, this corresponds to approximately $1/30R_b$. So the choice of uncertainty equal to $1/40R_b$ for the SOI reflects a medium point between the two situations—pessimistic for the former case and slightly optimistic for the latter. When the users are asynchronous, the interferers are assigned random carrier frequencies with two standard deviations equal to $1/20R_b$. This was chosen since it seemed reasonable that the frequency range of the interference would be more uncertain than that of the SOI.

Some simple form of automatic gain control (AGC) is assumed in the simulation environment. AGC was chosen primarily because the adaptive receiver algorithms were sometimes observed to fail catastrophically if the input signal was too large with respect to a reference signal, given either by training or decision direction, of amplitude one. Since it is reasonable that AGC would be implemented in any realistic receiver and we make the very harsh requirement of only 100 synchronization/training bits, some type of AGC is quite

important. The amplitudes of the various users are normalized to the root sum of squares of the amplitudes created randomly based upon the log-normal power variance. Specifically

$$A'_u = \frac{1}{\sqrt{\sum_{u=1}^{U} A_u^2}} A_u \tag{6.5}$$

is the AGC-adjusted amplitude of the uth user, where U is the total number of users, and

$$A_u = 10^{\frac{1}{20}\sigma_P P_u} \tag{6.6}$$

where A_u^2 is assumed to have a log-normal distribution with standard deviation σ_P, and $P_u \sim \text{Normal}\,(0,1)$.

To sum up the various simulation parameters, we now describe the unfaded CDMA signal. In complex baseband representation, it is given by

$$s(t) = \frac{1}{\sqrt{\sum_u A_u^2}} \sum_{u=1}^{U} A_u b_u(t-\tau_{d,u}) c_u(t-\tau_{d,u}) \exp\left[j\left(2\pi f_u t + \theta_u\right)\right] + n(t) \tag{6.7}$$

where b_u, c_u, A_u, f_u, θ_u, and $\tau_{d,u}$ are the differentially encoded bit, the spreading code, the amplitude, the baseband carrier frequency offset, the carrier phase, and the delay relative to the SOI of the uth user respectively. U is the number of simultaneous users. Noise, $n(t)$ (which lies outside of the summation), is a complex valued Gaussian process given by $n(t) = n_d(t) + jn_q(t); n_d, n_q \sim \text{Normal}\,(0, \sigma_n^2)$. The variance is calculated by the rule

$$\sigma_n = \sqrt{\frac{A_1'^2 N_s}{2} \frac{N_o}{E_b}} \tag{6.8}$$

where A'_1 is as defined in (6.5), N_s is the number of samples per bit, 30, and E_b/N_o is the bit energy to noise spectral density ratio. The bits and codes are represented by ± 1.

The data bits are chosen randomly for each user and differentially encoded. In the simulation program, the data bits are the output of a 32 stage maximal length sequence generator, having a repeat period of $2^{32} - 1 \approx 4$ billion bits. The codes are assigned randomly each Monte Carlo simulation with the requirement that no two users get the same code. Gaussian noise is generated using the modified Box-Muller transform of uniform random variable created via the Wichman-Hill algorithm, techniques outlined in [56]. The other parameters are assigned randomly each Monte Carlo simulation as well, but they are assigned differently depending upon whether we are examining the forward link (synchronous) or the reverse link (asynchronous). Therefore the discussion of these parameters is put off until section 6.3.

Table 6.2: Simulation channels models

Channel	E_b/N_o**[dB]**	**Veh spd [kph]**	**# rays**	**Delays**	**Ray ampl.**	**Ray env.**
AWGN	fwd lnk $\in \{8, 10\}$ rev lnk $\in \{8, 12\}$	N/A	1	0.0 μs	1.0	unity
Flat fading	fwd lnk TBD rev lnk TBD	$\in \{15, 45\}$	1	0.0 μs	1.0	Rayleigh
Rayleigh 2-ray	fwd lnk TBD rev lnk TBD	$\in \{15, 45\}$	2	0.0 μs 5.0 μs	1.0 0.5	Rayleigh Rayleigh
COST-207: "Typical rural"	fwd lnk TBD rev lnk TBD	$\in \{15, 45\}$	4	0.0 μs 0.2 μs 0.4 μs 0.6 μs	1.0 0.7937 0.3162 0.1	Ricean Rayleigh Rayleigh Rayleigh
COST-207: "Typical urban"	fwd lnk TBD rev lnk TBD	$\in \{15, 45\}$	6	0.0 μs 0.2 μs 0.6 μs 1.6 μs 2.4 μs 5.0 μs	0.7071 1.0 0.7937 0.5 0.4 0.3162	Rayleigh Rayleigh Gaus 1 Gaus 1 Gaus 2 Gaus 2
COST-207: "Bad case urban"	fwd lnk TBD rev lnk TBD	15	6	0.0 μs 0.4 μs 1.0 μs 1.6 μs 5.0 μs 6.6 μs	0.7071 1.0 0.7071 0.5657 0.7937 0.6325	Rayleigh Rayleigh Gaus 1 Gaus 1 Gaus 2 Gaus 2
COST-207: "Typical Hilly"	fwd lnk TBD rev lnk TBD	15	6	0.0 μs 0.2 μs 0.4 μs 0.6 μs 15.0 μs 17.2 μs	1.0 0.7937 0.6325 0.4472 0.5 0.2449	Rayleigh Rayleigh Rayleigh Rayleigh Gaus 2 Gaus 2

6.2.2 Fading Models

The Fading models are described in some detail in Table 6.2. A total of seven distinct models are assumed. In all but the first, AWGN, complex-valued fading waveforms of one second duration are created for each path based on one of four probabilistic approaches. Many of the rays are assumed to have a Rayleigh distribution. These are ones where the excess delay is not greater than 0.5μs. This well-known Doppler spectrum is given by

$$S_\tau(f) = \frac{A}{\sqrt{1-(f-f_d)^2}} \qquad \tau < 0.5\mu\text{s} \tag{6.9}$$

where A is a complex Gaussian process of baseband bandwidth equal to f_d, the maximum Doppler frequency, and $f \in \{-f_d, f_d\}$. When a line-of-sight (LOS) component exists, a

Ricean spectrum is assumed and is modeled by

$$S_\tau(f) = A\left(\frac{0.41}{2\pi f_d\sqrt{1-(f/f_d)^2}} + 0.91\delta\left(f-0.7f_d\right)\right) . \tag{6.10}$$

Two additional Doppler spectra, denoted *Gaus 1* and *Gaus 2* in Table 6.2, are proposed in the COST 207 final report. These were developed for the European Groupe Special Mobile (GSM) standard. [57] Let $G(f)$ denote a Gaussian spectral density, defined by

$$G(f;A,f_1,f_2) = Ae^{-\frac{(f-f_1)^2}{2f_2^2}} \tag{6.11}$$

where A is again a sample of a complex Gaussian process. For individual rays in which the excess delay times exceed 0.5μs but are less than 2μs, we apply Gaus 1, given by

$$S_\tau(f) = G\left(f;A,-0.8f_d,0.05f_d\right) + G\left(f;A_1,0.4f_d,0.1f_d\right) \qquad 0.5\mu\text{s} < \tau < 2.0\mu\text{s} . \tag{6.12}$$

When excess delay times exceed 2μs, the Gaus 2 spectrum, given by

$$S_\tau(f) = G\left(f;B,0.7f_d,0.1f_d\right) + G\left(f;B_1,-0.4f_d,0.15f_d\right) \qquad \tau > 2.0\mu\text{s} \tag{6.13}$$

is used.

In the simulations, a Doppler spectrum for each ray is created, zero padded out to 1000 samples, and then transformed into the time domain via the inverse discrete Fourier transform (IDFT). Thus we obtain a fading waveform of duration one second, sampled at 1 kHz. Then several cubic polynomial interpolations are performed to upsample this wave to the required 3.84 MSps rate. Note that these channel models allow statistical variations in the amplitudes and phases of the received rays but do not allow variations in the relative delays of each arriving component as would be expected in a truly dynamic channel. Nevertheless, these models give a good idea of what performance to expect from the realizable carrier recovery structures proposed in a nice variety of channel environments.

As may be noted from Table 6.2, we also select a set of E_b/N_o ratios at which we examine each of the channels. Vehicle speeds are also selected. In each case, an attempt is made to give as wide as possible range of impressions of receiver performance. Note that vehicle speeds of 15 and 45 kph correspond to Doppler frequencies for the 2050 MHz carrier of 28 and 85 Hz respectively. Note that while these speeds are conservative, at a carrier frequency of 900 MHz, consistent with cellular systems, these Dopplers reflect much faster speeds of 33.6 and 102 kph.

6.3 The Mobile Links

There are profound differences between the forward and reverse links that are assumed for this work. A brief outline of these differences is given by Table 6.3. Our motivations for investigating and presenting both links is to allow for the quite reasonable possibility that certain receiver or carrier recovery structures might be best applied to only one of these links. Since both are essential to cellular or mobile radio communications and since performance parity between the links is required to maximize system capacity, an examination of peculiarites of both the forward and reverse link is in order.

Table 6.3: Link-specific parameters for simulation study

	Forward Link	**Reverse Link**
Power variance	equal powers for all users; $\sigma_p^2 = 0$ $\left[\text{dB}^2\right]$	Log normal distribution; amplitudes $A_u = 10^{1/20\sigma_p P_u}$ where $\sigma_p^2 \in \{2, 20\}$ $\left[\text{dB}^2\right]$ and $P_u \sim \text{Normal}\,(0,1)$
Carrier phases	uniform dist. on $[0, 2\pi)$—all users identical	uniform dist. on $[0, 2\pi)$ —randomly assigned
Carrier frequencies	$\sim \text{Normal}\left(0, \sigma_{f,1}^2\right)$—all users identical	$\sim \text{Normal}\left(0, \sigma_{f,1}^2\right)$ SOI $\sim \text{Normal}\left(0, \sigma_{f,I}^2\right)$ SNOIs
Symbol timing	all users synchronous; mutual Xcorr is 1/15	all users have random delays; Xcorr is bounded by 7/15
Fading	single carrier; each path gets multiplied by one fading envelope	multiple carriers; each path from each user gets multiplied by one fading envelope

6.3.1 The Forward Link

The forward link is the much more forgiving link in the simulation strategy. First of all, we assume complete synchronization of the forward link. This means that there is only one carrier for all CDMA users. There is therefore only one carrier phase to track regardless of the level of MAI. The length 15 Gold codes, when synchronous, have an optimally low mutual cross-correlation of 1/15. In addition, the multiple access signal is constrained to have all users at equal powers. Thus the MAI is quite benign up to a fairly large number of users.

Finally, since there is only one carrier, only one set of fading waveforms need be generated. The received forward link signal gets multiplied by only one set of fading waveforms.

The complex baseband forward link signal is thus given by

$$s(t) = \frac{1}{\sqrt{U}} \sum_{u=1}^{U} \sum_{p=1}^{\#\text{Paths}} b_u(t-\tau_p)c_u(t-\tau_p)A_p\delta\left(t-\tau_p\right) M_p(t) \exp\left[j\left(2\pi\left(f_1 t - f_o\tau_p\right) + \theta_1\right)\right] + n(t) \tag{6.14}$$

where b_u, c_u, U, and $n(t)$ are as defined in (6.7), A_p and τ_p are the deterministic amplitude and time delay of the pth ray component as given in Table 6.2, f_1 and θ_1 are the frequency offset and phase of the SOI (which are shared by all users), $f_o = 2050$MHz, and $M_p(t)$ is the complex-valued fading waveform discussed in section 6.2.2.

The use of a forward link pilot channel is common in CDMA systems and is a key feature of IS-95. We make no such assumption here as we are interested in the receiver's ability to perform coherent carrier recovery, relying solely upon the suppressed-carrier received signal. Moreover, as pilot pollution, the corruption of reference tones by those of surrounding cells, has become a noted weakness of IS-95, we believe it is helpful to further consider systems that place no reliance on dedicated carrier references.

6.3.2 The Reverse Link

The reverse link assumed in this research combines all that is challenging in CDMA systems. Power variances of 2 and 20 $\left[\text{dB}^2\right]$ are examined with 2 dB being the "tight" power control case, and 20 dB corresponding to a virtual lack of power control. In addition, the codes are completely asynchronous, which increases the mutual cross-correlation. Carrier frequencies and phases are also different for each user. This, as will be noted, can have some deleterious effects on carrier recovery structures that employ Mth-order nonlinearites to remove modulation.

Finally, in contrast to the forward link, each user's signal gets multiplied by mutliple fading waveforms, denoted $M_{p,u}$. This ultimately makes the received complex baseband, reverse link signal look like

$$\begin{aligned} s(t) = \frac{1}{\sqrt{\sum_u A_u^2}} \sum_{u=1}^{U} \sum_{p=1}^{\#\text{Paths}} & A_u b_u(t-\tau_u-\tau_p)c_u(t-\tau_u-\tau_p)A_p\delta\left(t-\tau_u-\tau_p\right) \\ & \times M_{p,u}(t) \exp\left[j\left(2\pi\left(f_u t - f_o\tau_p\right) + \theta_u\right)\right] + n(t) \end{aligned} \tag{6.15}$$

where all of the variables have been previously defined in either (6.7) or (6.14). Once again the the noise process $n(t)$ lies outside of the summations. Note that the consideration of fading simultaneous with power variances may give pessimistic results, especially in the case of loose power control.

6.4 Candidate Receivers Structures

At the start of the simulation portion of this work, we nominated a large number of potential receiver structures that might be applied to receiving the SOI in the conditions described above. In this section, we discuss the process of how the field was narrowed down from the very large number of possible carrier recovery candidates, discussed in section 6.4.1, to the more manageable number presented in section 6.4.3. Section 6.4.2 discusses this "weeding out" process and presents some early simulation results that helped make the determination of the final candidate algorithms and receiver structures.

6.4.1 Original Candidate Structures

Table 6.4 outlines a representative sampling of the original candidate structures of interest in the simulation work. Parameters, especially loop bandwidth for Costas and AFC loops, or, equivalently, N, the number of symbols over which the estimator is averaged, for open-loop structures, were iteratively tweaked to test candidate algorithms. Table 6.4 shows the best designs we were able to come up with for some of the various structures discussed in Chapters 3 through 5. Most of these preliminary simulations were run in single-user AWGN channel environments over a fairly low range of E_b/N_o ratios with a conventional matched filter receiver. Since the performance of such a receiver is known from theory for both ideal coherent and differentially coherent cases, we can see very clearly the BER impact of the carrier recovery structures.

We provide diagrams of most of these candidate receiver structures in figures at the end of this chapter where we denote all real scalars by single thin lines, complex scalars by double thin lines, and vector values by bold lines. Note that decision feedback, or equivalently, hard-limiting the I-channel of a Costas loop, while beneficial in forgiving high E_b/N_o and low MAI conditions, was not employed in any of the receivers examined since most of the conditions to be examined in Chapters 7 and 8 will not be so forgiving. Finally note that "ideal" carrier recovery means "perfect knowledge of the phase of the first arriving component of the SOI" is assumed as shown in Figures 6.6 and 6.12. While this is clearly unrealizable, it ought provide a *nearly* best case performance in the experiments in fading detailed in Chapter 8. It is conceivable, however, that the RAKE receiver, or a realizable adaptive receiver could perform *better* than this ideal receiver in any particular fading environment. This will, in fact, be observed in certain situations examined in Chapter 8.

As shown in Table 6.4, in many cases we implement a bank of similar carrier recovery circuits with different parameters. For example, five different Costas demodulators differing only in loop bandwidth were implemented for the conventional matched filter receiver; six

Table 6.4: Potential receiver structures with symbol rate processing

Description	**# Rxs**	**Parameters**	**Comments**
Matched Filter Receivers:			
Ideal coh.	1		Conforms to theory, 1 usr
Diff. coh.	1		Conforms to theory, 1 usr
Costas loop alone	5	$B_{L,c} = 10^{-3} R_b$	Acqu. time way too long
		$B_{L,c} = 10^{-2.5} R_b$	"
		$B_{L,c} = 10^{-2} R_b$	"
		$B_{L,c} = 10^{-1.5} R_b$	pretty good
		$B_{L,c} = 10^{-1} R_b$	very near ideal
Costas loop w/ combined AFC loop	6	$B_{L,c} = 10^{-3} R_b$, $B_{L,f} = 10^{-5} R_b$	Very bad performance
		$B_{L,c} = 10^{-3} R_b$, $B_{L,f} = 10^{-4} R_b$	"
		$B_{L,c} = 10^{-3} R_b$, $B_{L,f} = 10^{-3} R_b$	"
		$B_{L,c} = 10^{-2} R_b$, $B_{L,f} = 10^{-4} R_b$	"
		$B_{L,c} = 10^{-2} R_b$, $B_{L,f} = 10^{-3} R_b$	"
		$B_{L,c} = 10^{-2} R_b$, $B_{L,f} = 10^{-2} R_b$	best but still not good
AFC loop switched to Costas loop	3	$B_{L,c} = 10^{-2} R_b$, $B_{L,f} = 10^{-2} R_b$	Very bad performance
		$B_{L,c} = 10^{-2} R_b$, $B_{L,f} = 10^{-1.5} R_b$	"
		$B_{L,c} = 10^{-2} R_b$, $B_{L,f} = 10^{-1} R_b$	"
Modified 1st order, open loop est.	5	$N = 500$	Very high complexity
		$N = 168$	high complexity
		$N = 50$	reasonable complxty
		$N = 16$	good performance
		$N = 5$	"
RAKE Receiver:			
3-Finger diff. coh.	1		Identical perf. to diff. coh. MF in AWGN
Adaptive Filter Receivers:			
Ideal coh.	1		
Diff. coh.	1		
Costas loop alone	3	$B_{L,c} = 10^{-2} R_b$	Acqu. time way too long
		$B_{L,c} = 10^{-1.5} R_b$	okay performance
		$B_{L,c} = 10^{-1} R_b$	Pretty good
Modified 1st order, open loop est.	5	$N = 500$	Very high complexity
		$N = 168$	high complexity
		$N = 50$	reasonable complexity
		$N = 16$	good performance
		$N = 5$	"
Second-order open-loop estimator	6	$N = 16$ $\beta = 0.9$	fair performance
		$N = 16$ $\beta = 0.8$	bad performance
		$N = 16$ $\beta = 0.7$	"
		$N = 5$ $\beta = 0.9$	good but same as Mod 1st
		$N = 5$ $\beta = 0.8$	bad performance
		$N = 5$, $\beta = 0.7$	"

different second-order ML open-loop estimation structures were examined for the adaptive receiver; etc. In both the conventional matched filter and adaptive receiver cases, we implement ideal coherent carrier recovery to provide a baseline for the simulation results. We also implement differentially coherent receivers in which no carrier recovery is performed. The performance of these inherently realizable receivers will tell us whether carrier recovery was worth the trouble since it is the performance of these receivers that we are trying to better with coherent carrier recovery. In addition, a three-finger differentially coherent RAKE receiver is compared side-by-side with the others.

6.4.2 The "Weeding-Out" Process

It could be seen from very early in the simulation study that many receiver structures were simply not going to make the final cut. Costas loop receivers with bandwidths wider than the frequency uncertainty were penalized severely by the 100-bit synchronization requirement. This can be seen in Figure 6.2 where BER results for the widest three Costas loops are plotted. The loop bandwidths are $10^{-2}R_b$, $10^{-1.5}R_b$, and $10^{-1}R_b$ respectively and improve in performance in that order. Note how close the widest bandwidth Costas loop conforms to theory. This shows just how relatively immune binary PSK is to phase jitter. No errors were generated for 12 dB, but we have no reason to expect a sample point here not to conform to theory as well. Narrower bandwidths, $10^{-3}R_b$ and $10^{-2.5}R_b$, were also examined but fared even worse than the top curve in Figure 6.2. The acquisition time for the narrowest three Costas loops was judged to be far too long. The widest two, $B_{L,c} = 10^{-1.5}R_b$ and $B_{L,c} = 10^{-1}R_b$, were chosen for the final competition.

We chose to apply AFC in combination with the middle Costas loop, i.e., the one with the Costas bandwidth, $B_{L,c} = 10^{-2}Rb$, to see if AFC could buy back some of the BER penalty incurred by the requirement of synchronization in 100 symbols. Figure 6.3 shows the results of this portion of the preliminary investigation. As can be seen, widening the AFC loop bandwidth, $B_{L,f}$, incrementally improved the BER performance by improving the acquisition time relative to the Costas loop acting alone. Still, at no E_b/N_o did the performance of the combined AFC/Costas loop outperform the simulated DBPSK receiver.

All receiver structures employing AFC performed dismally for apparently one of two reasons. When the AFC loop bandwidth was narrow relative to the Costas loop bandwidth, as was suggested in Chapter 5, the acquisition time became too long. Thus a severe BER penalty was incurred, just as with the narrowbandwidth Costas loops. When the AFC loop bandwidth was widened, as was proscribed in Chapter 5, the acquisition time improved dramatically and incrementally improved BER, but in these situations steady-state phase

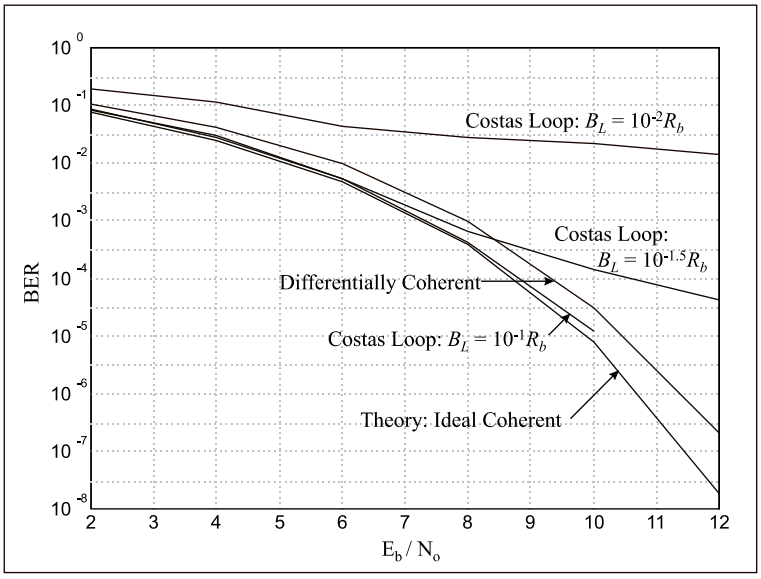

Figure 6.2: Simulation results for bit error probabilities versus E_b/N_o for three Costas demodulator structures; frequency uncertainty, $2\sigma_f = 1/40R_b$; simulated results for DBPSK and theoretical DEBPSK performance also shown

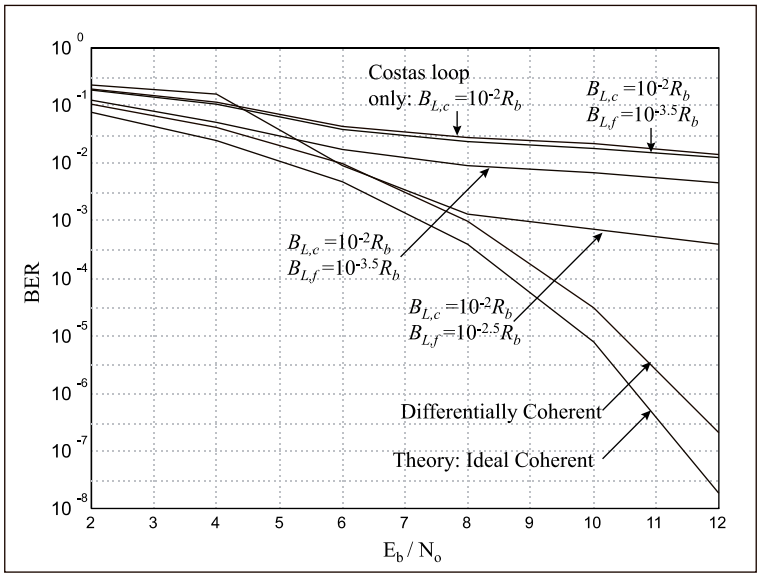

Figure 6.3: Simulation results for bit error probabilities versus E_b/N_o for three combined AFC and Costas loop carrier recovery structures; Costas bandwidth, $B_{L,c}$ is the same for all three; frequency uncertainty, $2\sigma_f = 1/40R_b$; Costas loop acting alone shown for comparison; simulated results for DBPSK and theoretical DEBPSK performance also shown

jitter became such a problem that BER was impacted anyway. If the frequency uncertainty had been much higher or if a higher-order signal constellation was used that proscribed the use of a wide bandwidth Costas loop, the addition of AFC might have been shown to be beneficial. In no observed cases in the preliminary study, however, did AFC prove helpful. A wide bandwidth Costas loop acting alone is a better choice given the constraints of the system described in sections 6.2 and 6.3. Thus all AFC implementations were removed from the final competition.

As a "sanity check" for the combined AFC/Costas loop, we examined a scheme where the AFC loop was allowed to run alone during the synchronization period and then was switched off in favor of the Costas loop after that. To our surprise, this switched scheme fared no better than a combined AFC/Costas loop where the outputs of both loop filters were summed. In fact, in some cases, it fared worse as shown in Figure 6.4. Reasonably good performance was only obtained from the widest bandwidth, $B_{L,f} = 10^{-2}R_b$, combined structure. Note, however, that it still performs worse than DBPSK. We believe that the inherently noisy differentiation process required by AFC limits its usefulness to high signal energy situations, and the low E_b/N_o constraints in our simulations proved catastrophic for AFC in terms of BER performance.

Early simulation results for the ML open-loop estimation schemes described in Chapter 4 proved quite illuminating. The modified first-order ML structure of section 4.2.4 proved to be quite adequate for the range of frequency offsets encountered in the preliminary investigation. In no case did the second-order structure of section 4.2.5, which utilizes a dedicated frequency offset estimator, perform better than the former structure. We observed, in fact, quite deleterious effects when increasing the value of N for the second-order structure, as shown for $N = 16$, $\beta = 0.9$, in the highest curve in Figure 6.5. This can only be due to the error of the frequency estimator propagating through the delay-line sum as shown in Figure 4.9. This error can be minimized by making the "forgetting factor," β, approach unity. This dramatically increases the acquisition time of the loop, however, and the 100-bit period synchronization requirement proved a handicap when this was tried. Since the second-order ML structure provided no appreciable gains in the simulation conditions, we removed it from consideration.

The values of $N \in \{500, 168, 50, 16, 5\}$ set for the modified first-order structures directly corresponded the loop bandwidths $B_{L,c} \in \{10^{-3}, 10^{-2.5}, 10^{-2}, 10^{-1.5}, 10^{-1}\} \times R_b$ of the Costas loops examined above. As noted in Chapter 4, an equivalent loop bandwidth for open-loop estimators may be defined as

$$B_{L,\hat{\theta}} = \frac{R_b}{2N} \, . \tag{6.16}$$

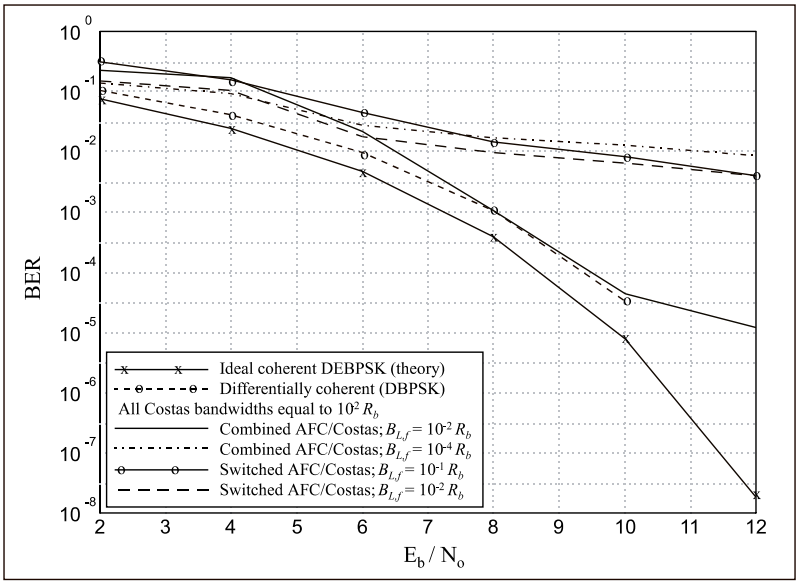

Figure 6.4: Simulation results for bit error probabilities versus E_b/N_o for two combined AFC/Costas loop carrier recovery structures and two switched loop structures; Costas bandwidth, $B_{L,c} = 10^{-2}R_b$ in all cases; frequency uncertainty, $2\sigma_f = 1/40R_b$; simulated results for DBPSK and theoretical DEBPSK performance also shown

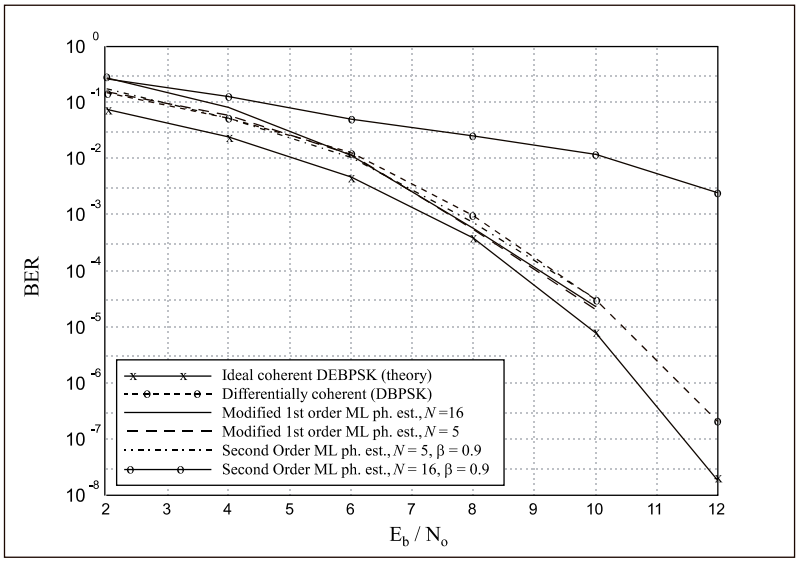

Figure 6.5: Simulation results for bit error probabilities versus E_b/N_o for four ML open-loop carrier recovery structures; frequency uncertainty, $2\sigma_f = 1/40R_b$; simulated results for DBPSK and theoretical DEBPSK performance also shown

Table 6.5: Final candidate receiver structures simulated and compared in future chapters on the basis of BER performance

Description	# Rxs	Parameters
Matched Filter Receivers:		
Ideal coh. DEBPSK	1	
Diff. coh. DBPSK	1	
Costas loop alone	2	$B_{L,c} = 10^{-1.5} R_b$ $B_{L,c} = 10^{-1} R_b$
Modified 1st-order open-loop est.	3	$N = 50$ $N = 16$ $N = 5$
RAKE Receiver:		
3-Finger diff. coherent	1	
Adaptive Filter Receivers:		
Ideal coherent	1	
Diff. coherent	1	
Costas loop alone	2	$B_{L,c} = 10^{-1.5} R_b$ $B_{L,c} = 10^{-1} R_b$
Modified 1st-order open-loop est.	3	$N = 50$ $N = 16$ $N = 5$

The complexity of the ML schemes for large N became a significant drawback when considering real-time implementation. Since these seemed to perform no better than those of smaller N, the $N = 500$ and $N = 168$ structures were disqualified for their complexity. The widest "bandwidth" structures, i.e., $N \in \{50, 16, 5\}$, were selected as final candidates. Note that the value of f_{max} for the modified first-order structure is set to $2\sigma_{f,1} = 1/40 R_b = 3200$Hz in all simulations.

6.4.3 Final Candidate Structures

The weeding out process described in section 6.4.2 led to the final nomination of receiver structures outlined in Table 6.5. Five receivers, of the original total of 15, the ideal and differentially coherent matched filter receivers, the three-finger differentially coherent RAKE receiver, and the ideal and differentially coherent adaptive receivers, employ no carrier recovery scheme at all. (The "ideal" coherent receivers, as noted above, simply make use of *perfect* knowledge of the phase of the first arriving SOI component.) These are presented in the simulations to provide baseline performance comparisons. The RAKE receiver, shown

in Figure 6.11, is particular interesting as it provides a more fair comparison to the adaptive equalizing receiver in the presence of multiple signal rays. Moreover, a three finger RAKE is implemented in the IS-95 CDMA standard. So five candidate carrier recovery algorithms made the final cut, two Costas loops and three modified first-order open-loop estimators. These are each applied to both the conventional matched filter and adaptive receivers to make up the final 10 receivers under consideration in Chapters 7 and 8.

6.5 Chapter Summary

The selection of candidate receiver structures for examination in the next two chapters is complete. In this chapter, we first presented detailed simulation procedures and assumptions in sections 6.1 through 6.3. We then used the system so defined to perform preliminary investigations into a large number of potential carrier recovery structures and weeded out all those whose performance did not seem worth additional attention. This exercise is detailed in section 6.4. This process led to the selection of the final candidates presented in Table 6.5. All that is left now is to move on to Chapters 7 and 8 where simulation results for these structures is presented.

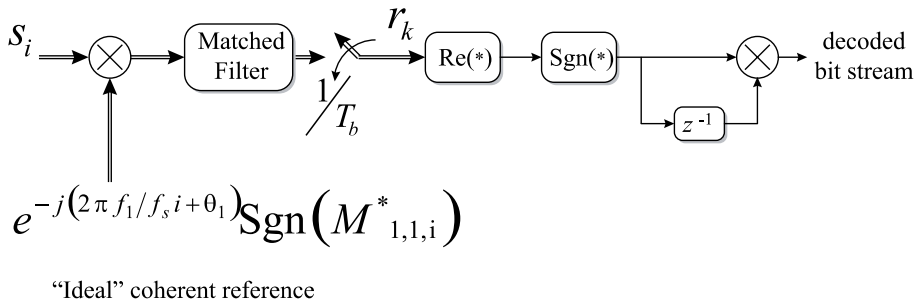

Figure 6.6: Conventional matched filter receiver for DEBPSK with "ideal" coherent carrier reference; $M_{1,1,i}$ corresponds to the first arriving fading waveform of user 1 at time i.

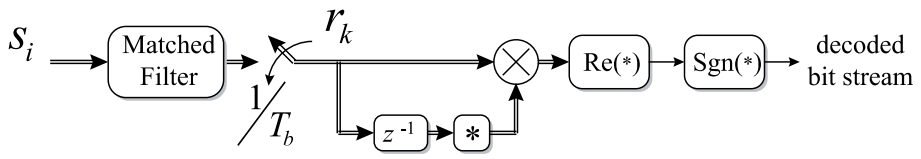

Figure 6.7: Conventional matched filter receiver using differentially coherent (DBPSK) detection

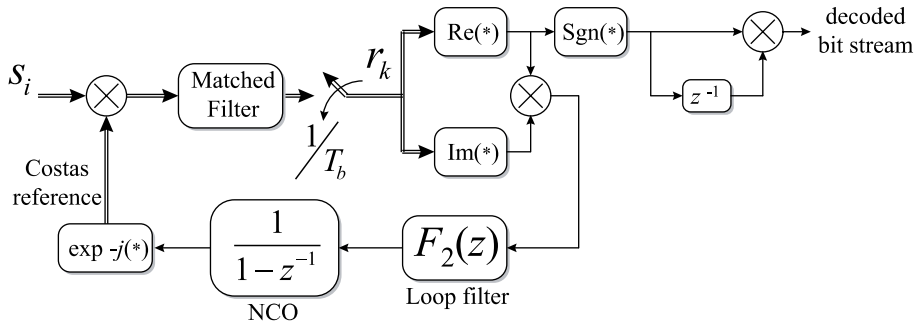

Figure 6.8: Conventional DEBPSK matched filter receiver with Costas loop carrier recovery

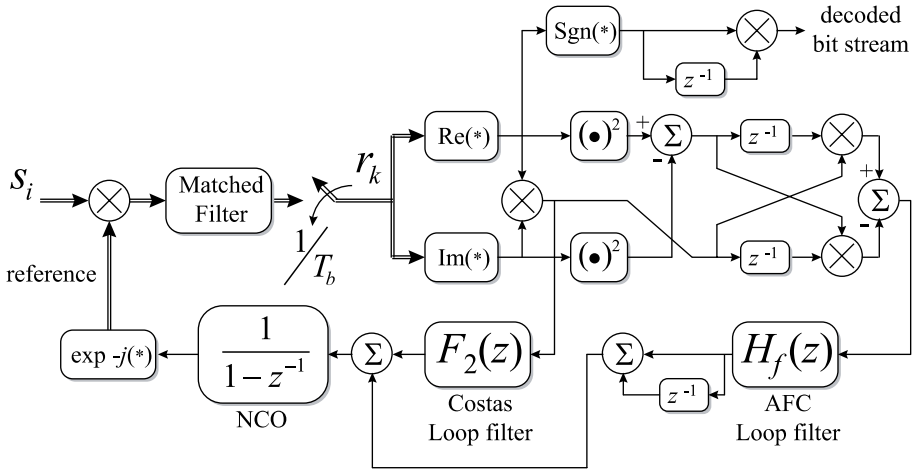

Figure 6.9: Conventional DEBPSK matched filter receiver with combined Costas and AFC loops for carrier recovery

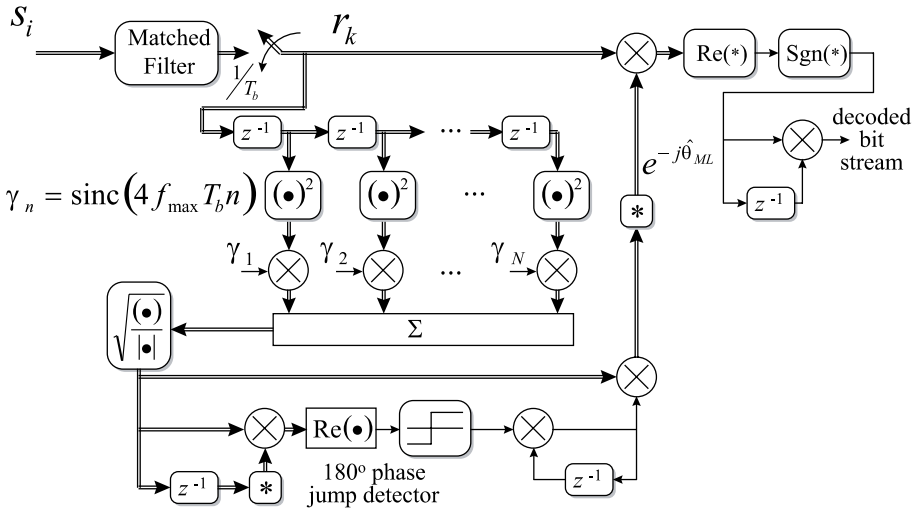

Figure 6.10: Conventional DEBPSK matched filter receiver with modified first-order ML carrier phase estimation circuit

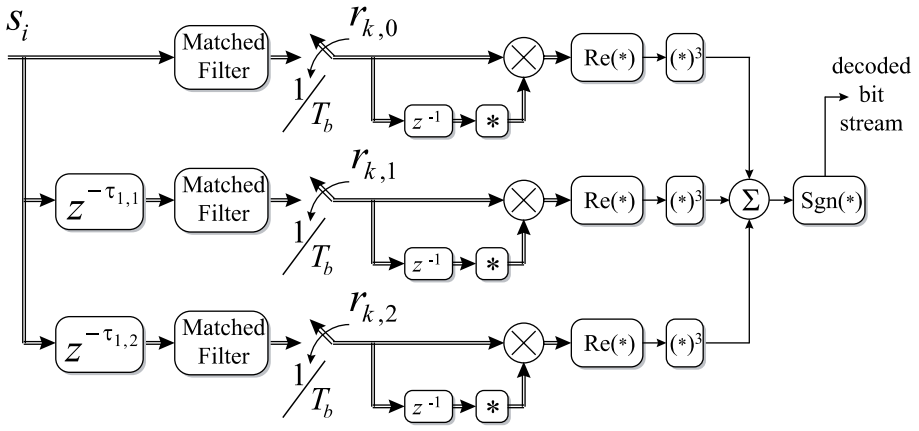

Figure 6.11: Three finger differentially coherent RAKE receiver with equal gain combining; First three arriving rays are assumed known, and first path is assumed to have delay, $\tau = 0$.

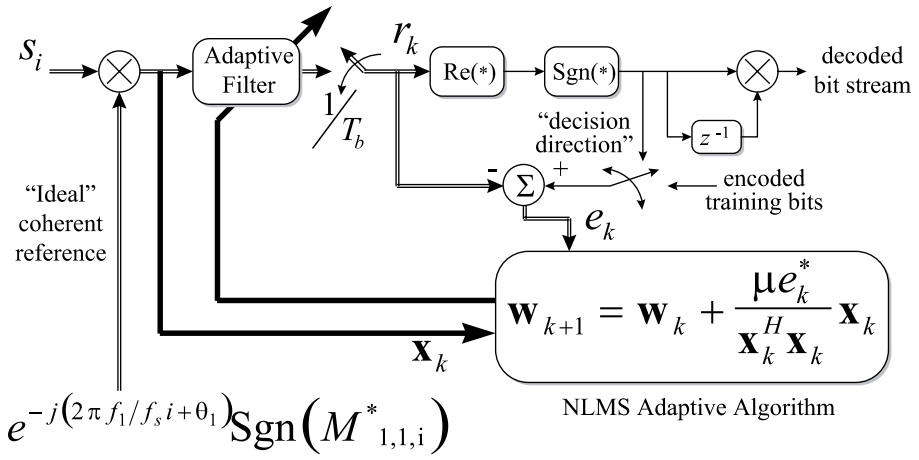

Figure 6.12: Adaptive filter receiver for DEBPSK with "ideal" coherent carrier reference; $M_{1,1,i}$ corresponds to the first arriving fading waveform of user 1 at time i.

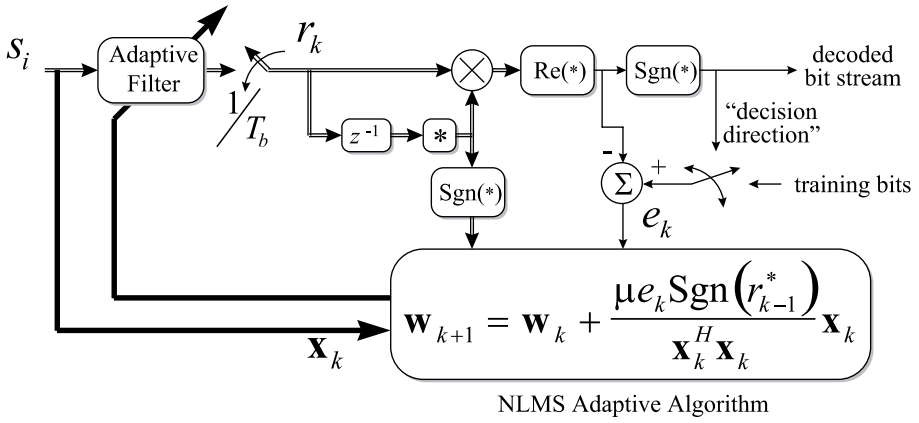

Figure 6.13: Adaptive filter receiver employing differentially coherent (DBPSK) detection

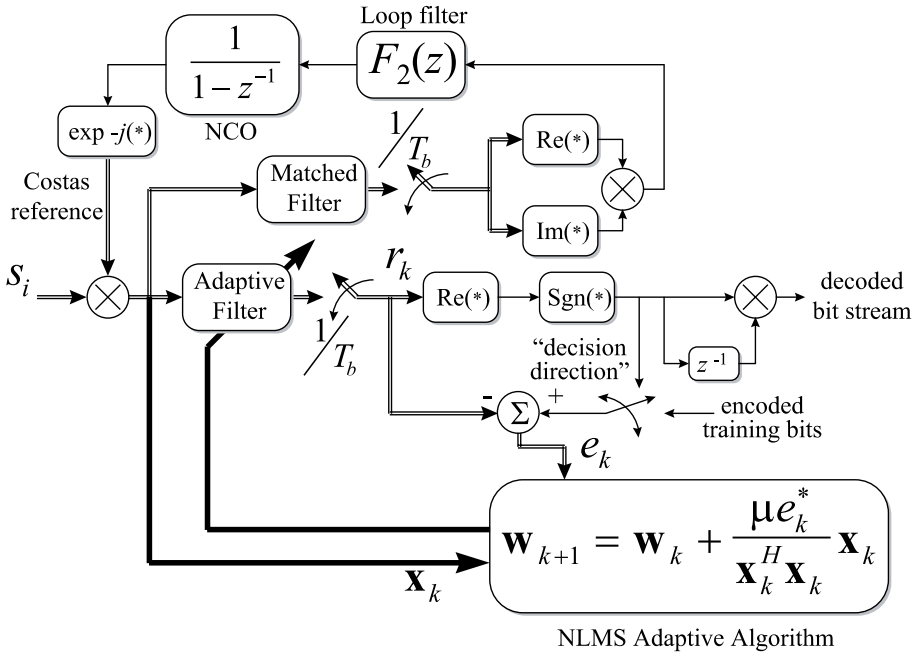

Figure 6.14: Adaptive filter receiver for DEBPSK with conventional Costas loop carrier recovery

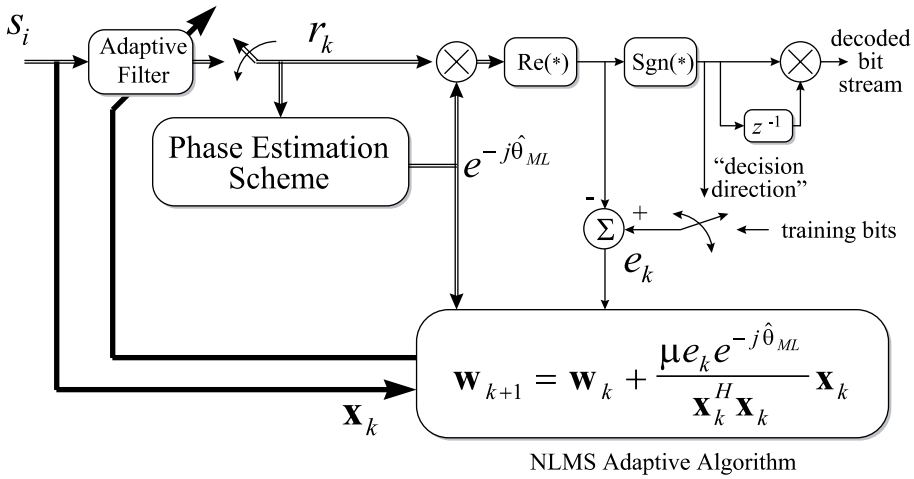

Figure 6.15: Adaptive filter receiver for DEBPSK with either modified first-order or second-order open-loop phase estimation scheme

Chapter 7

Receiver Performance in AWGN Channels

This chapter denotes the beginning of the presentation of results obtained via the Monte Carlo simulation methods discussed in Chapter 6. Results for the forward link and the reverse link, under two different power control assumptions, are presented in sections 7.2 and 7.3 respectively. In these sections, we also briefly discuss peculiar problems, caused by spread-spectrum MAI, faced by coherent carrier recovery structures in CDMA systems. Before discussing these results, however, this juncture serves as an opportune location to point out, in section 7.1, some of the relevant differences between the conventional and adaptive CDMA receivers examined in this research.

7.1 Notes on Conventional vs. Adaptive Reception

Before discussing performance results of several carrier recovery techniques in AWGN channels, it is important to give some high level discussion to *increased* performance degradation of adaptive reception, with respect to conventional reception, when differential detection is employed. The adaptive filter solution reduces the correlation, $\rho_{1,u}$ between the spreading code of the SOI (user 1) and those of the SNOIs (users u). This correlation *is* the MAI that incrementally degrades DSSS signals as more users are overlapped in time and frequency. Figure 7.1 shows this ability. It displays the correlation of the SOI's spreading code with 10 spreading codes in the system for a conventional matched filter receiver and of (borrowing the nomenclature [52]) a complex-weight fractionally-spaced linear adaptive receiver (CWFSLAR) after adaptation. Figure 7.1 clearly shows a dramatic reduction of MAI and a corresponding dramatic improvement in such a receiver's decision statistic. Time-dependent

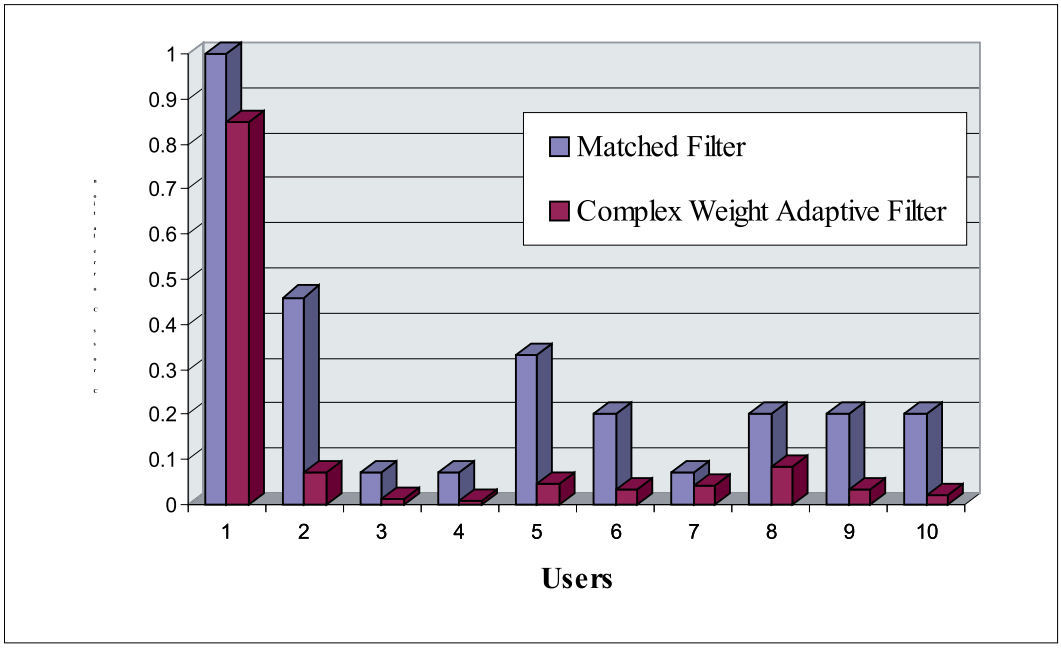

Figure 7.1: Cross-correlation of all user's pseudo-random codes with those of user 1 for matched filter and CWFSLAR filter, the latter exploiting cyclostationarity in the MAI; adapted from [52].

adaptive filtering for CDMA has been shown in [52] and [53] to be most effective when the CDMA users in a system share code repeat and chip rates, which allows the exploitation of cyclostationary signal properties.

The impact of reduced correlation between users can also be seen in Figures 7.2 and 7.3, where the BER performance on a synchronous CDMA forward link for matched and adaptive filter receivers are shown. The E_b/N_o ratios are 8 and 10 dB respectively. The ideal coherent and differentially coherent matched filter receivers are those shown in Figures 6.6 and 6.7, and the ideal and differentially coherent adaptive receivers are those shown in Figures 6.12 and 6.13. The reduced slope of the adaptive receiver performance curves shows adaptive reception has a lower sensitivity of BER to the number of simultaneous users. This is due entirely to the ability of the adaptive receiver to reduce cross-correlation with the MAI. We have noted in previous chapters that differential detection of encoded BPSK suffers about 1 dB of power degradation relative to ideal coherent reception of the same, a loss that hardly seems worth buying back given the simplicity of the DBPSK demodulator. This result however is for single user, AWGN environments, for receivers *not* employing adaptive equalization. What Figures 7.2 and 7.3 show dramatically is that the performance

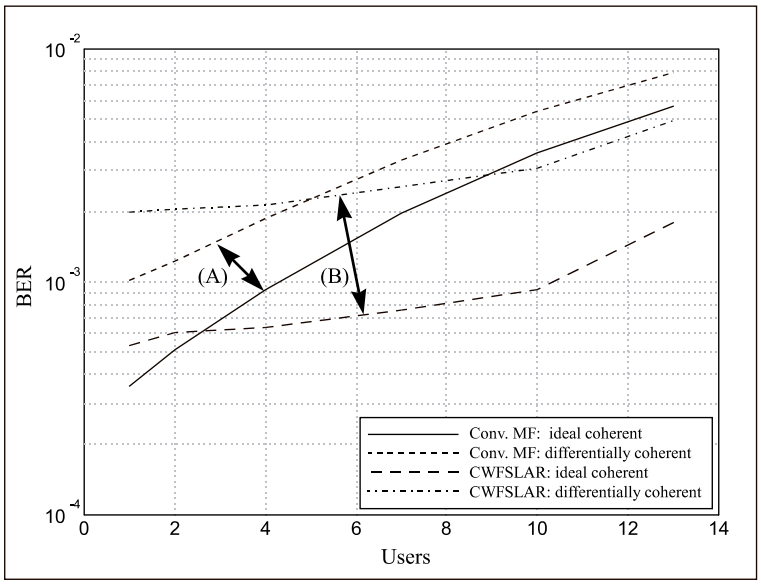

Figure 7.2: Simulation results for bit error probabilites versus number of users on the forward link in AWGN channel; $E_b/N_o = 8$ dB; performance of conventional matched and adaptive filters with "ideal" and differentially coherent reception shown; frequency uncertainty, $2\sigma_f = 1/40R_b$.

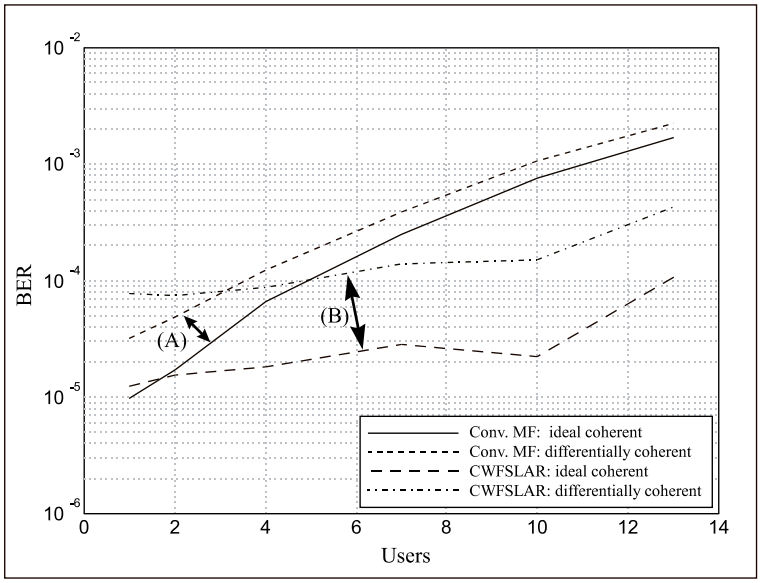

Figure 7.3: Simulation results for bit error probabilites versus number of users on the forward link in AWGN channel; $E_b/N_o = 10$ dB; performance of conventional matched and adaptive filters with "ideal" and differentially coherent reception shown; frequency uncertainty, $2\sigma_f = 1/40R_b$.

degradation of differential with respect to ideal coherent detection is far worse for adaptive receivers than for conventional matched filter receivers. Note the distances denoted by arrows (A), are much shorter than the distances marked by (B). So the news that adaptive reception can increase CDMA system capacity is now accompanied by the news that much of its promised capacity is dependent upon coherent carrier recovery. This observation is the most critical motivation for examining carrier recovery for adaptive receivers as we attempt to "buy back" as much of this degradation as possible.

Observe, too, that in all cases in Figures 7.2 and 7.3, the performances of conventional and adaptive receivers cross at some small number of users. Theoretically the performance of the matched and adaptive filter receivers should be precisely equivalent for one user, since the adaptive filter ought converge to the matched filter which is the optimal filter, according to the Weiner criterion, for a *single user* receiver in AWGN. However, due to the non-zero NLMS stepsize, μ, which is equal to relatively large values of 0.5 during training and 0.1 during decision direction, we can expect additional mean squared error in the adaptive algorithm. It is therefore not surprising that the matched filter receiver performs better than the adaptive in single-user AWGN environments. That the differential receiver performance lines cross at 5 users in both figures is somewhat surprising. We point out, however, that the mutual cross-correlation between the users in this forward link situation is 1/15. Therefore, the adaptive receiver really has very little interference to mitigate in this benign environment. In short, at E_b/N_o of 8 and 10 dB, the conventional receivers perform quite well and the adaptive receivers offer relatively little enhancement.

7.2 The Forward Link in AWGN

Figures 7.4 through 7.7 show the performance of the two candidate Costas loops relative to ideal and differentially coherent receivers. In all cases, the Costas loop of bandwidth, $B_{L,c} = 10^{-1.5}R_b$, performed much worse than the expectations given in Chapter 6. This is very likely due to relatively high value of frequency uncertainty, $2\sigma_f = 1/40R_b \approx 10^{-1.6}R_b$, used for all simulations. What was even more unexpected was the terrible performance of the widest bandwidth Costas loop with $B_{L,c} = 10^{-1}R_b$ for multiple user cases. This bandwidth is sufficiently wide for the typical values of frequency offsets simulated. Note that in each of Figures 7.4 through 7.7, showing conventional and adaptive receiver performance at both 8 and 10 dB respectively, this latter Costas loop does exactly what we expect for one user—it performs better than the respective differentially coherent receivers and closely approaches the performance of ideal coherent reception. But adding as few as one user, for a total of two, causes the performance of this Costas loop to dramatically degrade. It is

quite clear that even in this seemingly benign forward link environment, MAI wreaks havoc for conventional Costas demodulators. We attribute this problem to additional amplitude jitter, which is described in section 7.2.1. Then in section 7.2.2, we give further discussion to the simulation results obtained for Costas loops (Figures 6.8 and 6.14 for conventional and adaptive receivers respectively) and open-loop estimators (Figures 6.10 and 6.15) on the forward link in AWGN.

7.2.1 Costas Loop Jitter on Synchronous CDMA Links

Recall that the forward link CDMA signal may be expressed in complex baseband representation by

$$s(t) = \left(\sum_{u=1}^{U} d_u(t) c_u(t) \right) e^{j\,(2\pi f_1 + \theta_1)} + n(t) \tag{7.1}$$

where, as in previous chapters, d_u and c_u are the differentially encoded data symbol and the spreading code of the uth user at time, t; f_1 and θ_1 are the residual frequency offset and phase of user 1, the SOI, which are shared by all users on the single carrier; U is the total number of users on the system; and $n(t)$ is a complex-valued Gaussian noise process. Downconversion by a complex-valued reference,by $\exp\left[-j\left(2\pi f_{ref} + \hat{\theta}\right)\right]$, as shown in Figure 6.8 and sampling at time, $t = kT_b$, results in a receiver statistic

$$r_k = \left(d_{1,k} + \sum_{u=2}^{U} d_{u,k}\rho_{1,u} \right) e^{j\phi_k} + n_k \tag{7.2}$$

where we have subsumed frequency and phase errors between the reference and transmitted carriers into the possibly time-varying phase error, ϕ. $\rho_{1,u}$ represents the cross-correlation between the spreading code of user 1 and user u. Note that in this particular case, all cross-correlation values between all users' time-synchronous bits are 1/15. So let $\rho_{i,j} = \rho = 1/15, \forall i \neq j$, and note that $\rho_{i,i} = 1$. In-phase and quadrature arm samples may thus be represented by

$$i_k = \left(d_{1,k} + \sum_{u=2}^{U} d_{u,k}\rho_{1,u} \right) \cos\phi_k + n_{d,k} \tag{7.3}$$

and

$$q_k = \left(d_{1,k} + \sum_{u=2}^{U} d_{u,k}\rho_{1,u} \right) \sin\phi_k + n_{q,k}\ . \tag{7.4}$$

The error term, e_k, is no longer a simple function of one symbol and noise as it was in Chapter 4. Rather it is given by

$$e_k \ \stackrel{\triangle}{=}\ i_k q_k$$

$$= \frac{1}{2}\sin 2\phi \left[d_{1,k}^2 + \rho^2 \left(\sum_{u=2}^{U} d_{u,k}^2 + \sum_{u=2}^{U} \sum_{\substack{v=2 \\ v \neq u}}^{U} d_{u,k} d_{v,k} \right) \right] + f(n_k)$$

$$= \frac{1}{2}\sin 2\phi \left[1 + \rho^2 \left((U-1) + \sum_{v=1}^{U(U-1)} d'_v \right) \right] + f(n_k) \tag{7.5}$$

where $f(n_k)$ is some complicated function of the noise that is ignored for now and d' is simply a binary random variable taking values ± 1. Note that at steady-state, when 2ϕ is supposed to be small, the effect of the cross-correlation between the SNOIs and user 1 on the error term *should* be small, especially since $\rho^2 = (1/15)^2 = 1/225$. There are two things to note, however. First of all, the summation in (7.5) of $U(U-1)$ binary random variables is well-known to be itself a random variable with variance $U(U-1)$. This wide variance would seem to contribute significantly to the jitter of the Costas loop even at steady-state for even a relatively small number (say about 4) of users. Since we have chosen a very wide Costas bandwidth to meet the specification of acquisition within 100 symbols, this jitter may not be getting mitigated sufficiently in the loop filter. Secondly, the acquisition behavior of the Costas loop due to these added random terms in the error signal could become severely compromised. We believe that some combination of these issues contributes to the poor performance of even the best Costas loop shown in Figures 7.4 through 7.7.

7.2.2 Results on the Forward Link in AWGN

The performance degradation of the Costas loop in the adaptive filter receiver, as seen in Figures 7.5 and 7.7, is more striking than that seen in the conventional receivers in Figures 7.4 and 7.6. As noted briefly in section 4.2.7, the interaction between dual feedback systems as depicted in Figure 6.14 is complicated and seems likely to lead to catastrophic effects. In combining closed-loop carrier recovery with complex-weight adaptive filtering, we operated on the assumption that the *time constant* of the carrier recovery loop ought to be shorter than that of the adaptive algorithm. That is, we desired the carrier recovery structure to respond more quickly to changes in phase and correct for them before the adaptive algorithm could react. We therefore only examined relatively wide Costas bandwidths for the adaptive receiver, the widest being $B_{L,c} = 10^{-1} R_b$ as shown in Figures 7.5 and 7.7. That this structure performed well for one user is encouraging. But the nearly catastrophic performance degradation seen in these plots for even a few additional users suggests that close-loop carrier recovery circuits interact poorly in adaptive receivers designed to mitigate spread-spectrum MAI.

One final note on Costas loop performance here is that remodulation or hard-limiting

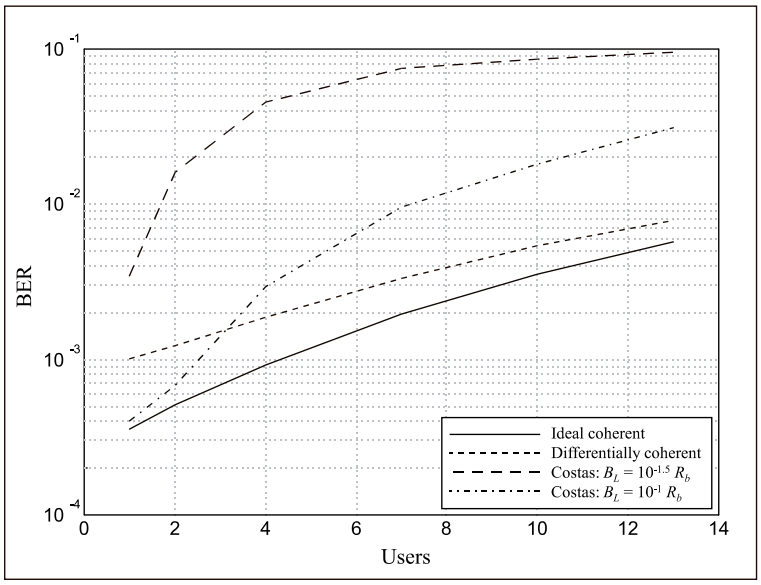

Figure 7.4: Simulation results for bit error probabilites versus number of users on the forward link in AWGN channel; $E_b/N_o = 8$ dB; performance of conventional matched filter receivers with various Costas loops, "ideal" carrier recovery, and differentially coherent reception shown; frequency uncertainty, $2\sigma_f = 1/40R_b$.

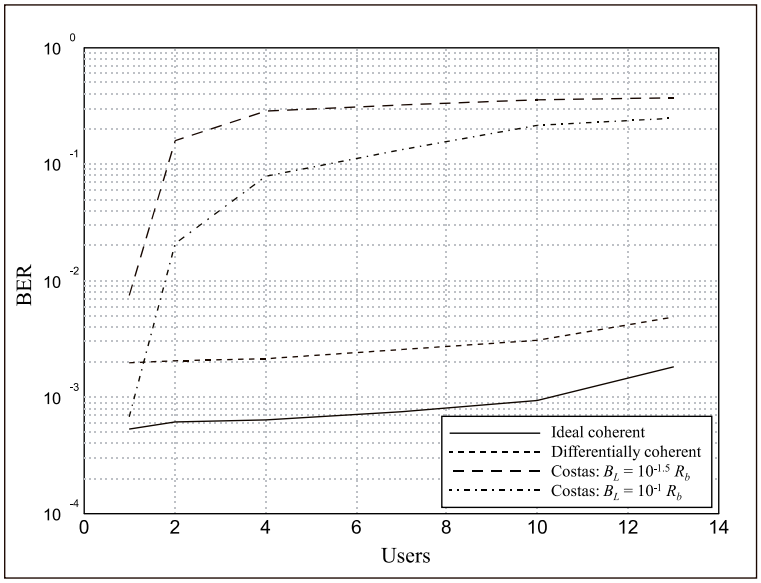

Figure 7.5: Simulation results for bit error probabilites versus number of users on the forward link in AWGN channel; $E_b/N_o = 8$ dB; performance of adaptive filter receivers (CWFSLAR) with various Costas loops, "ideal" carrier recovery, and differentially coherent reception shown; frequency uncertainty, $2\sigma_f = 1/40R_b$.

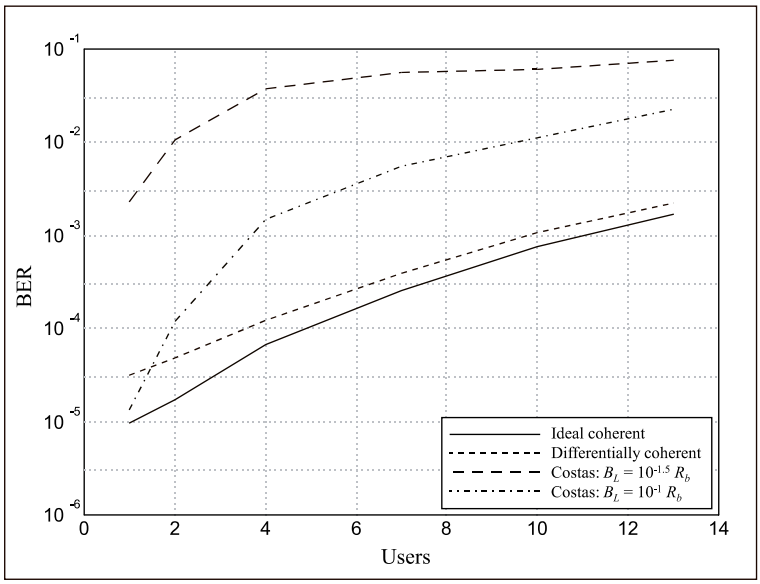

Figure 7.6: Simulation results for bit error probabilites versus number of users on the forward link in AWGN channel; $E_b/N_o = 10$ dB; performance of conventional matched filter receivers with various Costas loops, "ideal" carrier recovery, and differentially coherent reception shown; frequency uncertainty, $2\sigma_f = 1/40R_b$.

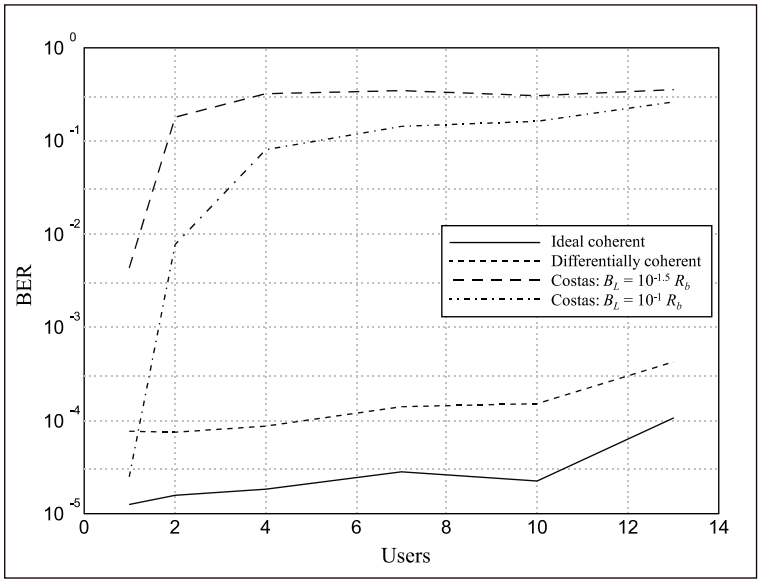

Figure 7.7: Simulation results for bit error probabilites versus number of users on the forward link in AWGN channel; $E_b/N_o = 10$ dB; performance of adaptive filter receivers (CWFSLAR) with various Costas loops, "ideal" carrier recovery, and differentially coherent reception shown; frequency uncertainty, $2\sigma_f = 1/40R_b$.

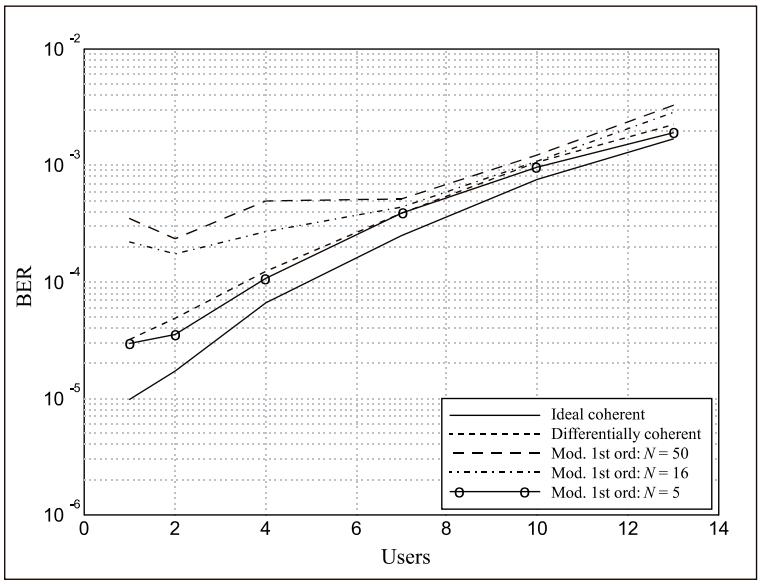

Figure 7.8: Simulation results for bit error probabilites versus number of users on the forward link in AWGN channel; $E_b/N_o = 10$ dB; performance of conv. matched filter receivers with various modified 1st-order ML phase estimation structures, "ideal" carrier recovery, and differentially coherent reception shown; frequency uncertainty, $2\sigma_f = 1/40R_b$.

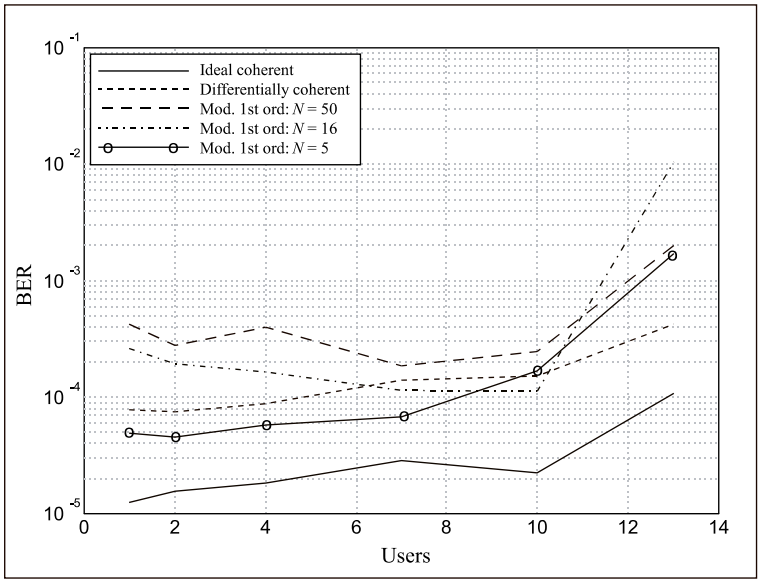

Figure 7.9: Simulation results for bit error probabilites versus number of users on the forward link in AWGN channel; $E_b/N_o = 10$ dB; performance of adaptive filter receivers (CWFSLAR) with various modified 1st-order ML phase estimation structures, "ideal" carrier recovery, and differentially coherent reception shown; freq. uncertainty, $2\sigma_f = 1/40R_b$.

the I-channel was not applied in any of the results presented here. This practice would undoubtedly mitigate the problems shown in (7.5) due to squaring but would create additional problems in low E_b/N_o or high MAI where as noted in Chapter 4, the receiver statistics are highly corrupted and $\hat{d}_k$ might often be 180^o out of phase with d_k. A possible work-around for this problem would be to create a receiver that could arbitrarily switch between squaring and remodulation (hardlimiting) based on some knowledge of received E_b/N_o and/or the number of CDMA users on the system. An algorithm would have to be developed for such a receiver and would incrementally increase mobile unit complexity for the forward link. As such, this possibility was not pursued for this research but is posited as a possibly fruitful area of future work in carrier recovery.

Figures 7.8 and 7.9 show the performance of the modified first-order ML phase estimator, at $E_b/N_o = 10$ dB, relative to the ideal and differentially coherent conventional and adaptive receivers respectively. Here quite opposite behavior to that of the Costas loop seems to be taking place. Especially for the $N = 50$ and $N = 16$, performance is degraded for a low number of users, but performance is improved with respect to the Costas loop for a large number of users. In a most encouraging result, the $N = 5$ modified first-order estimator performed quite well in both the conventional and adaptive receivers. In Figure 7.8, the conventional receiver case, this estimator did slightly better than the differentially coherent receiver at all numbers of users examined. In the adaptive receiver case shown in 7.9, the $N = 5$ estimator did significantly better than the differentially coherent scheme at 1 through 7 users, equally well at 10 users, and quite a bit worse at 13.

The reasons for the degraded performance of the two ML estimators for one or few users are not exactly known. According to the theory presented Chapter 4, the performance between an ML estimator and a Costas loop is identical in a single-user, AWGN environment, which *is* the case at one user in Figures 7.8 and 7.9. This prediction only holds, however, for channels in which the received phase, θ_k, is not time-varying. Remember that the modified first-order ML structure, described in section 4.2.4, relies on a sinc$(*)$ weighting function to compensate for a frequency offset, which is reflected in a constant rotation in the samples θ_k. This structure was shown to be the ML estimator for a frequency offset *equal* to f_{max}. In these simulations, however, $f_{max} = 2\sigma_{f,1}$, and not the actual value of the frequency offset. Some degradation is therefore expected. This fact alone probably explains how the $N = 5$ estimator usually outperformed the $N = 16$ and $N = 50$ estimators. The longer the averaging period, the greater the impact of the suboptimality of choosing a fixed f_{max} parameter. In addition, the performance of the 180^o phase jump detector is not perfect and can be expected to contribute to BER degradation. For these reasons, we are not terribly

surprised with the performance curves of the ML estimators shown in Figures 7.8 and 7.9 and are in fact quite pleased with the performance of the $N = 5$ estimator.

7.3 The Reverse Link in AWGN

7.3.1 Estimator Bias in Multiple Access Channels

The jitter problem for the Costas loop on the synchronous forward link in CDMA channels described in section 7.2.1 has something of an analogous problem on asynchronous reverse links. This is seen most easily in a bias that can creep in to the ML estimators studied. Consider the reverse link desicion statistic seen by the base station at the output of the matched filter,

$$r_k = d_{1,k}e^{j\theta_{1,k}} + \sum_{u=2}^{U} A_u d_{u,k}\rho_{1,u}e^{j\theta_{u,k}} + n_k \tag{7.6}$$

where $d_{u,k}$, $\rho_{1,u}$, U, and n_k are as defined in section 7.2.1; the respective, generally time-varying, carrier phases, $\theta_{u,k}$, are now arbitrary for each user, u; and A_u is the amplitude of the uth user defined via

$$A_u = 10^{\frac{1}{20}\sigma_P P_u}, P_u \sim \text{Normal}\,(0,1) \tag{7.7}$$

or the square root of the uth user's power, which is distributed log-normally with variance σ_P^2 $\left[\text{dB}^2\right]$.

Assuming that the use of decision feedback for the phase estimation scheme is unwarranted or unavailable, we remove the modulation on the statistics r_k by squaring them. Consider r_k^2 on this asynchronous reverse link. Squaring (7.6) we get

$$\begin{aligned} r_k^2 &= d_{1,k}^2 e^{j2\theta_{1,k}} + \sum_{u=2}^{U} d_{u,k}^2 A_u^2 \rho_{1,u}^2 e^{j2\theta_{u,k}} + \sum_{u=2}^{U}\sum_{\substack{v=2\\v\neq u}}^{U} d_{u,k}A_u\rho_{1,u}e^{j2\theta_{u,k}} d_{v,k}A_v\rho_{1,v}e^{j2\theta_{v,k}} + f(n_k) \\ &= e^{j2\theta_{1,k}} + \sum_{u=2}^{U} A_u^2\rho_{1,u}^2 e^{j2\theta_{u,k}} + \sum_{u=2}^{U}\sum_{\substack{v=2\\v\neq u}}^{U} d_{u,k}d_{v,k}A_uA_v\rho_{1,u}\rho_{1,v}e^{j2\left(\theta_{u,k}+\theta_{v,k}\right)} + f(n_k) \end{aligned} \tag{7.8}$$

where, as before, $d_i^2 = 1$ and $f(n_k)$ is some function of the noise. As discussed in Chapter 4, we then sum these statistics over N observations, possibly weighting each statistic. The complex square root and signum function then yields the phase estimate of $e^{j\theta 1,k}$.

The double summation term in (7.8) clearly might cause jitter in this estimate, but note that summing over N observations reduces the impact of this term since the term is randomly modulated by $d_u d_v$. Observe, however, that the second, single-sum term could

become quite pernicious to efforts of extracting an estimate. This term is no longer dependent upon the randomly modulated data, and thus produces a potentially large bias in the estimator. The effects of the second term can only be averaged out over N observations if the frequency offsets of user 1 and users u, which produce the time-varying quality of θ_k, are quite different. But it is very easy to imagine a situation where the frequency offsets of the various users, while different, are nevertheless close, and thus in an observation interval of N symbols, θ_k of the various users will change very little. This will hinder the attempt at constructing an estimate for the phase of the SOI, $e^{j\theta_{1,k}}$, and, at any rate, cause the estimator to no longer be ML.

The bias produced by the second term of (7.8) could be assumed to be small if the various A_u are relatively equal and the $\rho_{1,u}$ are small. However, on the reverse link, we cannot make this assumption in general. The amplitudes A_u, relative to A_1, are now random parameters based on the level of power control available and/or the instantaneous fading levels and $\rho_{1,u}$ is bounded by the fairly high value of 7/15. This weakness therefore might be expected to show itself in sections 7.3.2 and 7.3.3 where results on the reverse link are discussed. Note finally that this perceived weakness of the ML estimators developed in Chapter 4 could be overcome by developing, from first principles, a ML phase estimator for the peculiarities of the multiple access link under consideration. Though such an estimator is not attempted in this work, it is believed to be a possibly fruitful area of future research. Moreover, we believe that if such an estimator were constructed, it would necessarily rely upon knowledge of the MAI, specifically the time-varying phase of all the users in the system. Since such information could reasonably be expected to be available in base station technology, the development of such a structure might possibly have profound implications and benefits for multiuser detection.

7.3.2 Results in Strict Power Control

Figures 7.10 through 7.13 show the performance of Costas loop carrier recovery for conventional matched filter and adaptive filter receivers at E_b/N_o of 8 and 12 dB respectively. These results are obtained on an asycnhronous reverse link with "strict" power control, a situation defined by $\sigma_P^2 = 2$ dB^2. As in section 7.2, the narrower bandwidth Costas loop, $B_{L,c} = 10^{-1.5}R_b$, performs much worse than hoped. Again this is most likely due simply to the large frequency uncertainty, $2\sigma_f = 3200$ Hz, present in all of these simulations. Also in very much the same way as it did for the synchronous forward link, the Costas loop helps the adaptive receivers in Figures 7.11 and 7.13 only for one user. For two or more CDMA users, the Costas loop quickly degrades in these plots and performs far worse than

the differentially coherent adaptive receiver.

The one bright spot in Figures 7.10 through 7.13 is how well the wider bandwidth, $B_{L,c} = 10^{-1}R_b$, Costas carrier recovery circuit works for the conventional matched filter receivers in Figures 7.10 and 7.12. At $E_b/N_o = 8$ dB (Figure 7.10) this Costas loop outperforms differentially coherent reception for 1 through 7 users and performs equivalently for a higher number. At $E_b/N_o = 12$ dB (Figure 7.12), this Costas loop performs roughly the same as differentially coherent reception. The reasonably good performance of this Costas loop in these two plots is in stark contrast to its performance in Figures 7.4 and 7.6 where quick and almost catastrophic degradation is seen for even a few users added. Again, we believe that this is due to the jitter problem discussed in section 7.2.1. Interestingly, the Costas loop examined performs better relative to the differentially coherent receiver on the asynchronous reverse link where the MAI is undoubtedly worse, than on the synchronous forward link where there is only a single carrier to track.

The performance of the modified first-order ML* phase estimation structures is shown in Figures 7.14 and 7.15 for the conventional and adaptive receivers respectively at $E_b/N_o = 12$ dB. For the conventional receiver (Figure 7.14), the open-loop schemes perform resonably well although in no case do they do better than differentially coherent reception. For the adaptive filter receiver (Figure 7.15), the "narrow bandwidth," $N \in \{50, 16\}$ recovery schemes fare quite a bit worse than differentially coherent in all cases. The $N = 5$ estimator performs reasonably well for $U = \{1, 2, 4\}$ users, but this receiver's performance degrades catastrophically for higher numbers of users.

We point out here that the adaptive receiver is subject to *complete failure*, i.e., it gets into situations where decision directed adaptation with a high density of incorrect decisions produces a highly suboptimal filter, and the BER approaches 0.5. This problem is exacerbated by the stringent 100-symbol synchronization requirement and shows itself more and more as the channel conditions get worse and worse, i.e., as the fading rate or level of MAI increases or as received E_b/N_o drops. Such catastrophic failure is not observed in the matched filter receiver, but a steady, more predictable degradation due to these impairments. This can strongly bias the BER results seen in the plots presented for the adaptive receiver. In a realistic receiver, this failure would result in a "dropped call" in cellular telephony or in a request for retransmit in a packet-based wireless data system, and therefore, though such failures ought to be considered a penalty against the receiver, they would nevertheless not likely result in a steady-state BER as bad as is being counted in these simulations.

*We now use the "maximum likelihood" designation loosely, only to bring consistency to the discussion. As pointed out in section 7.3.1, this estimator is not ML for the asynchronous CDMA environment.

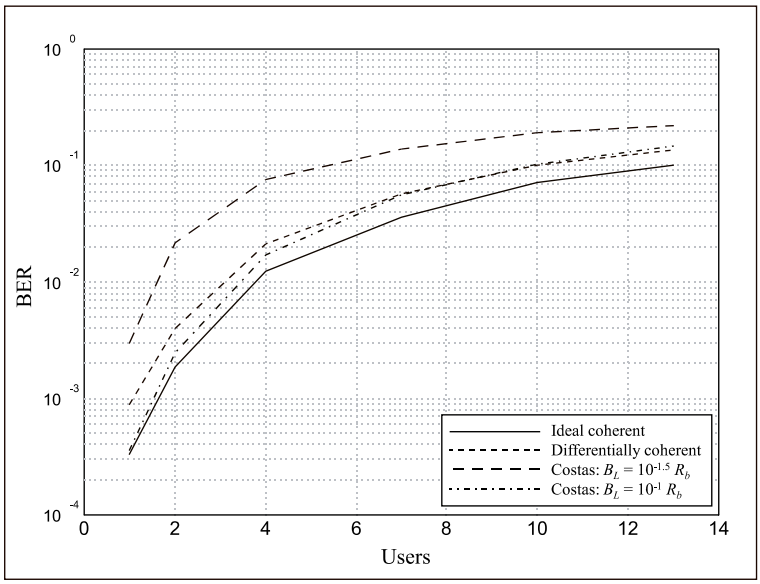

Figure 7.10: Simulation results for bit error probabilites versus number of users on reverse link in AWGN channel; "strict" power control, $\sigma_P^2 = 2$ dB^2; $E_b/N_o = 8$ dB; performance of conv. matched filter receivers with various Costas loops, "ideal" carrier recovery, and differentially coherent reception shown; freq. uncert., $2\sigma_f = 1/40R_b$.

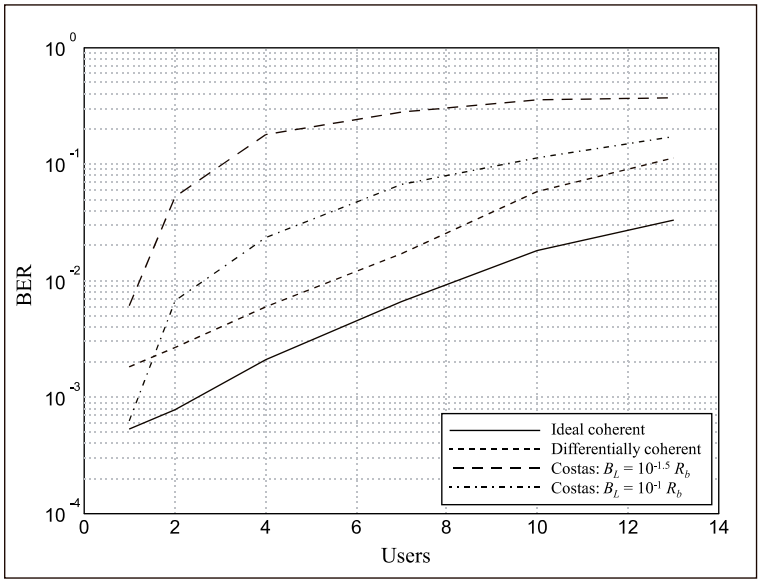

Figure 7.11: Simulation results for bit error probabilites versus number of users on reverse link in AWGN channel; "strict" power control, $\sigma_P^2 = 2$ dB^2; $E_b/N_o = 8$ dB; performance of adaptive filter receivers (CWFSLAR) with various Costas loops, "ideal" carrier recovery, and differentially coherent reception shown; freq. uncert., $2\sigma_f = 1/40R_b$.

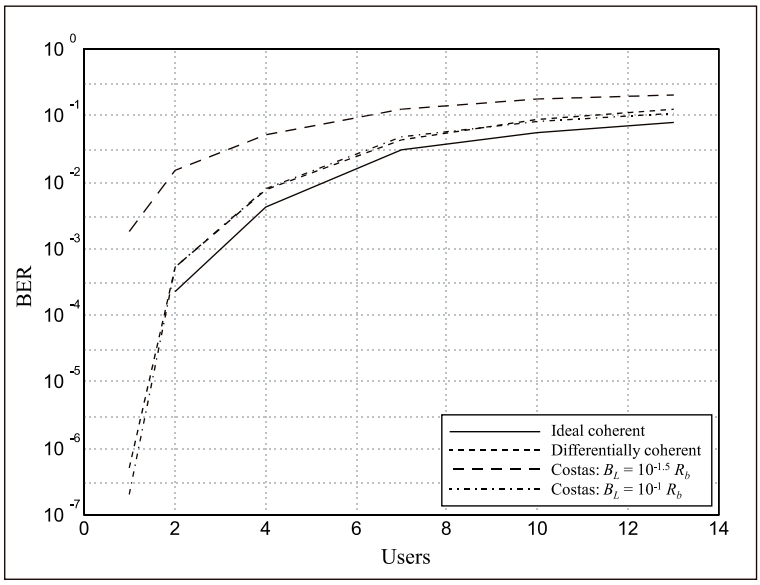

Figure 7.12: Simulation results for bit error probabilites versus number of users on reverse link in AWGN channel; "strict" power control, $\sigma_P^2 = 2$ dB^2; $E_b/N_o = 12$ dB; performance of conv. matched filter receivers with various Costas loops, "ideal" carrier recovery, and differentially coherent reception shown; freq. uncert., $2\sigma_f = 1/40R_b$.

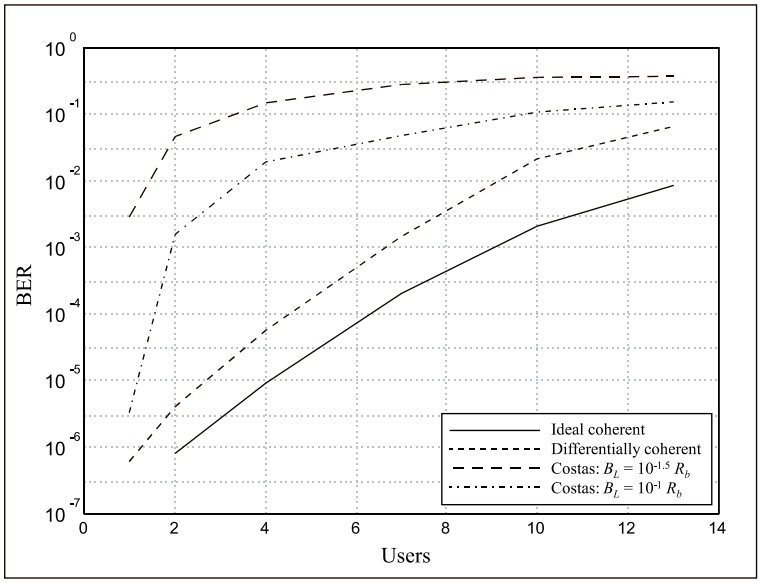

Figure 7.13: Simulation results for bit error probabilites versus number of users on reverse link in AWGN channel; "strict" power control, $\sigma_P^2 = 2$ dB^2; $E_b/N_o = 12$ dB; performance of adaptive filter receivers (CWFSLAR) with various Costas loops, "ideal" carrier recovery, and differentially coherent reception shown; freq. uncert., $2\sigma_f = 1/40R_b$.

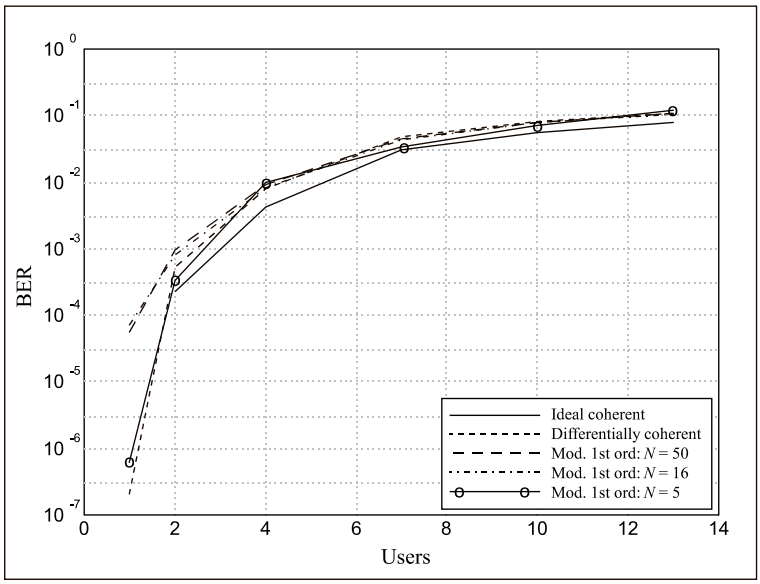

Figure 7.14: Simulation results for bit error probabilites versus number of users on reverse link in AWGN channel; "strict" power control, $\sigma_P^2 = 2$ dB^2; $E_b/N_o = 12$ dB; performance of conv. matched filter receivers with various modified 1st-order ML phase est. structures, "ideal" carrier recovery, and diff. coherent reception shown; freq. uncert., $2\sigma_f = 1/40R_b$.

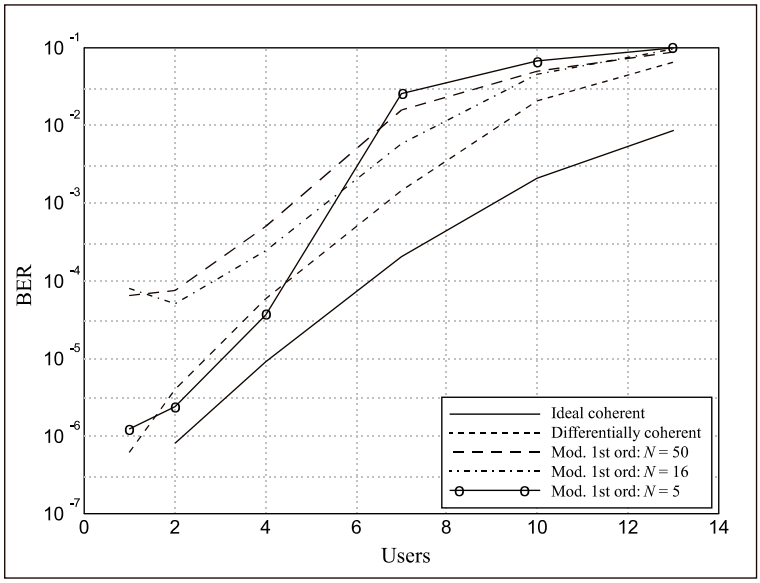

Figure 7.15: Simulation results for bit error probabilites versus number of users on reverse link in AWGN channel; "strict" power control, $\sigma_P^2 = 2$ dB^2; $E_b/N_o = 12$ dB; performance of adaptive receivers (CWFSLAR) with various modified 1st-order ML phase est. structures, "ideal" carrier recovery, and diff. coherent reception shown; freq. uncert., $2\sigma_f = 1/40R_b$.

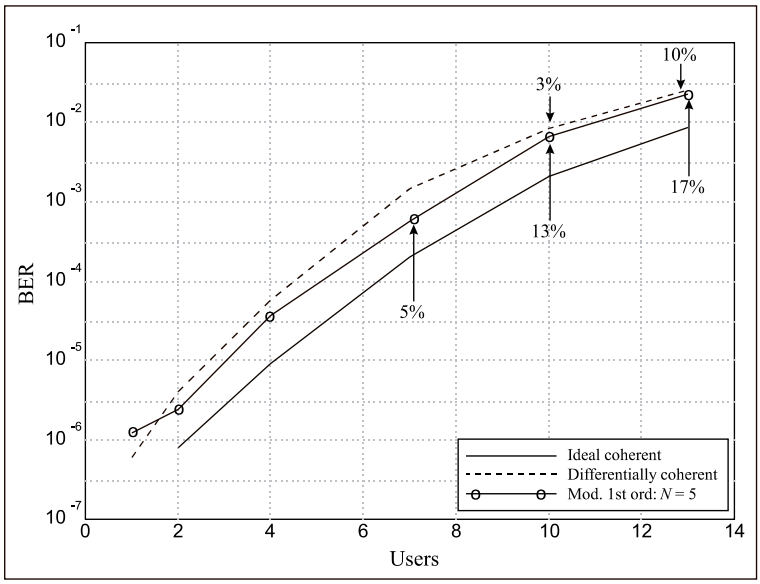

Figure 7.16: Same simulation results as shown in Figure 7.15 (check), except BER results exceeding 0.2 are discarded and replaced with the receiver failure rate.

We therefore reserve the right to discount simulation points resulting in a sufficiently high BER for the adaptive receivers and substitute instead a failure rate for the various receivers. Sufficiently high BER is henceforth arbitrarily defined as 0.2 because once a receiver begins to make errors at this rate, incorrect decision direction will force the filter to a abitrarily incorrect solution and it is highly atypical for such a filter solution to be rectified solely by continued decision-direction. When the adaptive filter fails, retraining is necessary. Using this threshold, we point out that for Figure 7.15, the failure rates are zero for the ideal coherent adaptive receiver at all numbers of users. For the differentially coherent and the $N = 5$ open-loop estimation receivers the failure rates are {0%, 3%, and 10%} and {5%, 13%, and 17%} at 7, 10, and 13 users respectively. This different view of the results in Figure 7.15 is given in Figure 7.16 where the performance of the $N = 5$ ML estimation receiver is seen to improve dramatically with respect to differentially coherent detection. In fact, ignoring for the moment the unpleasant fact of the high failure rate, we get expected performance from the realizable coherent receiver, i.e., the performance curve lies pretty much between the differential and ideal receiver and "buys back" some of the performance degradation.

7.3.3 Results in Loose Power Control

The asynchronous reverse link with users' powers distributed log-normally with a variance of 20 dB^2 is the most challenging environment yet discussed in this work. Large power variances are sometimes referred to as the *Near-Far* (NF) problem and are a widely recognized "Achilles heel" of conventional CDMA systems. Figures 7.17 and 7.18 show the performance of Costas loops at $E_b/N_o = 12$ dB for the conventional and adaptive receivers respectively. For the conventional matched filter receiver in Figure 7.17, all strategies, including ideal coherent carrier recovery, perform almost equally poorly, and therefore very little can be said concerning the efficacy of carrier recovery strategies for such receivers in this environment. The NF problem does its expected work in severely degrading the performance of all the matched filter receivers.

The adaptive receiver, on the other hand, with its ability to mitigate MAI, shows great promise in Figure 7.18, at least for the ideal coherent receiver. The adaptive receiver is at its best when reducing the correlation between CDMA users and as such, advertises itself as a Near-Far resistant receiver strategy. The very disappointing feature of this figure is that even differentially coherent reception is degraded severely relative to the ideal coherent case. The two Costas loops examined, $B_{L,c}$ equal to $10^{-1.5}$ and 10^{-1} R_b, give no improvement. The great distance seen between the ideal and differentially coherent curves in Figure 7.18 continues to motivate an on-going search for carrier recovery structures that can better approach the performance provided by ideal.

The performance of open-loop estimation structures is shown for conventional and adaptive receivers in Figures 7.19 and 7.20 respectively. In the same manner as with the Costas loop, all conventional receivers degrade badly in these severe NF conditions. For the adaptive receivers in Figure 7.20, the $N = 50$ and $N = 5$ modified first-order estimation receivers show some promise in at least approaching the performance of the differential receiver. But the distance between these curves and that of ideal coherent reception is disappointing.

As was true in section 7.3.2, the BER simulated for adaptive filter receiver suffers dramatically from fairly high failure rates in Figures 7.18 and 7.20. These rates, not surprisingly, are much higher than those seen in the "tight" power control conditions of the previous section. These failures, while no small problem for receiver design, nevertheless bias the BER curves in these figures. Without plotting the adjusted results, we point out that even the ideal coherent adaptive receiver experienced failures at rates of {1%, 6%, and 7%} at 7, 10, and 13 users respectively. The diffentially coherent and modified first-order receivers, however, failed at much higher rates. The differentially coherent receiver failed {1%, 9%, 19%, 35%, and 43%} of the time, for 2, 4, 7, 10, and 13 users respectively. Similarly, the

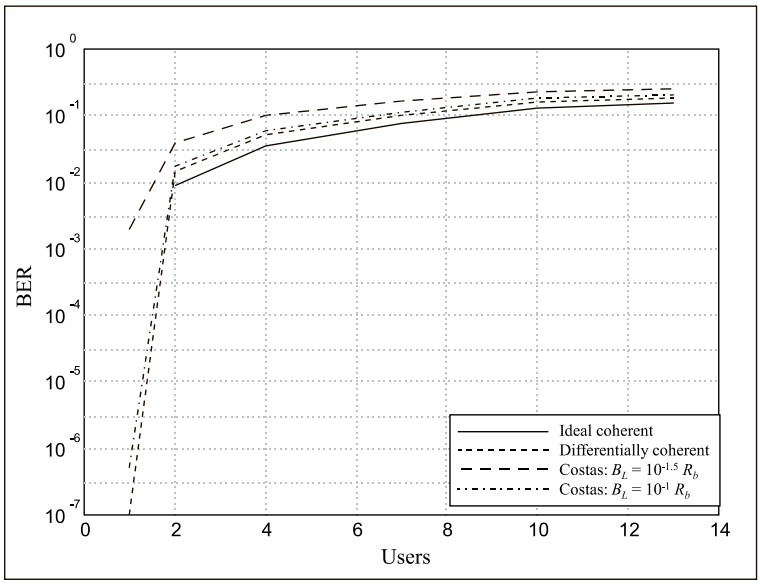

Figure 7.17: Simulation results for bit error probabilites versus number of users on reverse link in AWGN channel; "loose" power control, $\sigma_P^2 = 20$ dB^2; $E_b/N_o = 12$ dB; performance of conv. matched filter receivers with various Costas loops, "ideal" carrier recovery, and differentially coherent reception shown; freq. uncert., $2\sigma_f = 1/40R_b$.

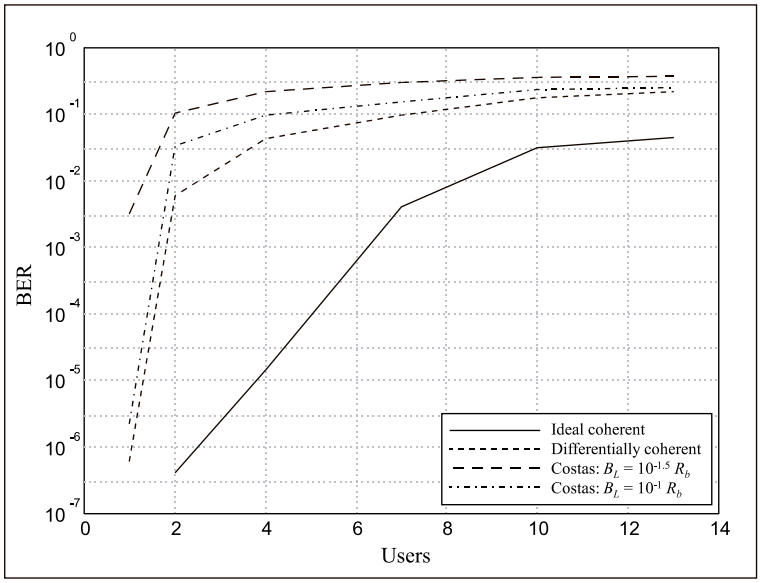

Figure 7.18: Simulation results for bit error probabilites versus number of users on reverse link in AWGN channel; "loose" power control, $\sigma_P^2 = 20$ dB^2; $E_b/N_o = 12$ dB; performance of adaptive receivers (CWFSLAR) with various Costas loops, "ideal" carrier recovery, and differentially coherent reception shown; freq. uncert., $2\sigma_f = 1/40R_b$.

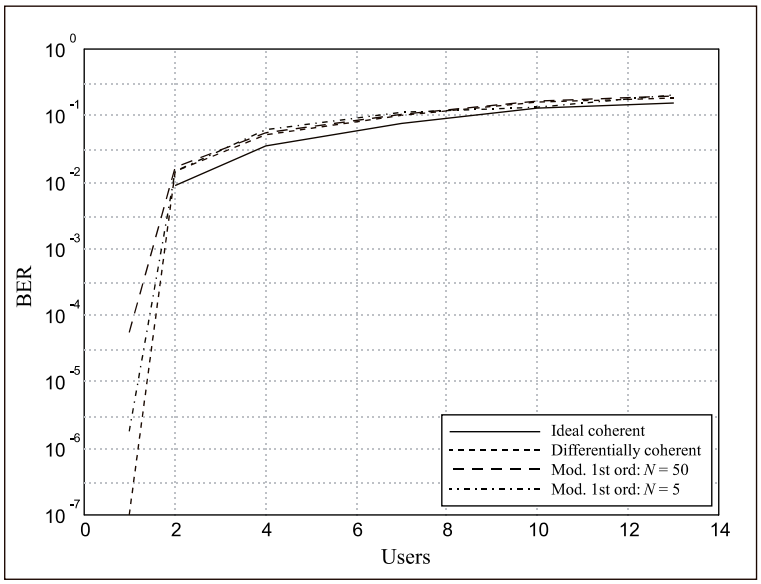

Figure 7.19: Simulation results for bit error probabilites versus number of users on reverse link in AWGN channel; "loose" power control, $\sigma_P^2 = 20$ dB^2; $E_b/N_o = 12$ dB; performance of conv. matched filter receivers with various modified 1st-order ML phase est. structures, "ideal" carrier recovery, and diff. coherent reception shown; freq. uncert., $2\sigma_f = 1/40R_b$.

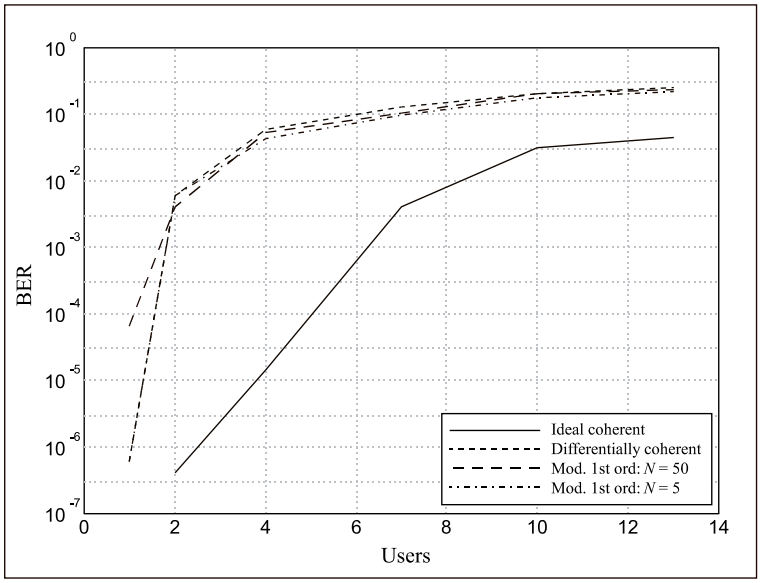

Figure 7.20: Simulation results for bit error probabilites versus number of users on reverse link in AWGN channel; "loose" power control, $\sigma_P^2 = 20$ dB^2; $E_b/N_o = 12$ dB; performance of adaptive receivers (CWFSLAR) with various modified 1st-order ML phase est. structures, "ideal" carrier recovery, and diff. coherent reception shown; freq. uncert., $2\sigma_f = 1/40R_b$.

$N = 5$ open-loop estimator receiver failed {1%, 12%, 25%, 40%, and 50%} of the time, for 2, 4, 7, 10, and 13 users. This dismal performance in bad, though still reasonable, channel conditions continues to motivate investigation not only into carrier recovery circuits that can approach the performance of ideal coherent reception but also into ways of preventing the failure of the adaptive algorithms to begin with.

7.4 Chapter Summary

In this chapter, we have examined the performance of conventional matched filter and adaptive (CWFSLAR) receivers with ideal coherent carrier recovery, with differentially coherent detection, and with several realizable, closed-loop and open-loop carrier recovery schemes. Where expedient, we have endeavored to give some mathematical justification for the types of results seen in the simulations. Specific attention was given to the problem of added Costas loop jitter being caused by the synchronous MAI in section 7.2.1. The problem of estimator bias in an asynchronous reverse link was also discussed in section 7.3.1.

The results are somewhat disappointing for the carrier recovery circuits examined as we had hoped that they could consistently narrow the gap between the performance of ideal coherent carrier recovery and that of differentially coherent detection. That this has not been observed is nevertheless illuminating and lends credence to early suspicions that differential reception might be a very good alternative in mobile channels. We now move on to the final area of investigation in this research in Chapter 8 where we will expand the investigation to include a variety of fading channels commonly encountered in mobile systems.

Chapter 8

Receiver Performance in Fading Channels

In this chapter, we submit the various receivers proposed in Chapter 6 to even more challenging conditions, those of fading that are so often encountered in mobile environments. In section 8.1, we briefly examine receiver performance in flat fading—a situation where a single path is received, in which all frequency components of the signal are attenuated identically, at any given time. Then in sections 8.2 through 8.4, we examine frequency selective channels where 2, 6, and 4 rays, respectively, reach the receiver spaced by periods greater than the channel coherence time. In the on-going consideration of these channels, we continue to examine both synchronous forward link results as well those of asynchronous reverse links.

We caution the reader to be prepared to see some very high BER values in the proceeding discussion. This motivates two points. First of all, the high BERs and high failure rates for adaptive receivers, commonly seen in this chapter, remind us that BER is not the only figure of merit for wireless digital systems. Rate of packet loss or requests for retransmit for data communications and blocking probability or rates of call-dropping for isochronous voice or multimedia applications are all valid bases, other than steady-state BER, upon which to judge the performance of wireless systems. Further, these auxilliary figures of merit can provide a *different* and *useful* perspective for such systems. Because of the additional complexity required by the simulations to measure these characteristics, we were not able to investigate them in this present research. We acknowledge this weakness in this work only to suggest and motivate future investigation strategies. Interleaving, packetization or frame-based transmission strategies, and forward error correction, should be considered ripe and relatively untouched topics for research in the area of suppressed-carrier recovery.

Note, however, that *relative* merits of various reception strategies are presented herein, and they nevertheless provide a fairly wide view of the subject.

A second point to be made is that due to the high BERs observed, especially in sections 8.2 through 8.4 and additionally in the interest of time and of brevity, we do not present results for two of the channel models mentioned in Chapter 6. Specifically, the "Hilly" and "Bad Urban" channels are left relatively untouched in this work. These are the two most challenging of all the channels described and as such can be expected and have been observed to give even worse results than those given attention here.

Finally, in section 8.5, we briefly re-focus attention on the simulation procedures used. Specifically, the impact of the stringent 100-symbol synchronization and training requirement and the impact of the choice of wide frequency uncertainty upon the BER performance is examined. This examination is part of an attempt to explain the relatively poor BER results which follow. We ultimately find, however, that relaxation of the simulation parameters mentioned does not provide any additional information concerning the receivers under examination.

8.1 The One-Ray Rayleigh, "Flat Fading" Channel

The flat-fading model is not one in which we expect to see the adaptive receivers significantly outpace the conventional receivers. As we will see in proceeding sections, adaptive reception has the capability of coherently combining multipath in addition to suppressing MAI, but in this particular model there is no multipath to combine, only small-scale Rayleigh fading applied to a single ray. That being so, there is still some benefit of adaptive reception in the suppression of MAI, but the dramatic improvements, relative to conventional matched filter reception seen when the adaptive filter additionally exploits multipath, will be delayed until sections 8.2 through 8.4 where frequency-selective environments are considered. Simulations for this the one-ray Rayleigh channel model were carried out at E_b/N_o of 15 and 20 dB at vehicle speeds of 15 and 45 kph for both forward and reverse links. On the reverse link, power variances of 2 and 20 dB^2 were examined. In section 8.1.1, we briefly examine the results for forward link and then move on to those of the reverse link in section 8.1.2.

8.1.1 Performance on the Synchronous Forward Link

Figures 8.1 and 8.2 show the performance of receiver structures designed for conventional matched filter and adaptive receivers respectively. E_b/N_o is set to be 20 dB in these particular results, and the vehicle speed is 45 kph. The relative flatness of most of the curves

clearly shows the low level incremental MAI added for each user in a synchronous CDMA system. The most noteworthy feature of both plots is the bad performance of the Costas loop, $B_{L,c} = 10^{-1}R_b$, for all situations except one user. As was discussed in section 7.2.1, we believe this is due to the additional amplitude jitter induced into the Costas error signal by the MAI. The $N = 16$ modified first-order estimation structure, in contrast, performs quite well for both the conventional receivers in Figure 8.1 and the adaptive receivers in Figure 8.2. Nevertheless, at no time does this open-loop estimation scheme outperform differential detection, which tends in this case to discourage the use of carrier recovery at all.

8.1.2 Performance on the Asynchronous Reverse Link

Figures 8.3 and 8.4 show the BER performance of conventional and adaptive receivers, respectively, in the one-ray Rayleigh fading model. The conditions are an E_b/N_o of 15 dB, a vehicle speed of 15 kph, and "tight" power control. Results for the conventional receivers in Figure 8.3 are not terribly noteworthy except perhaps in that they show quite poor BER performance. Realizable carrier recovery structures show little or no improvement over differentially coherent detection. As expected, the ideal, unrealizable, coherent reception of differentially encoded PSK fares slightly better.

Results for the adaptive receivers in Figure 8.4, on the other hand, do show at least one interesting result. Ideal coherent reception, as we have come to expect, performs best for all numbers of users. For the first time in this work, however, the Costas loop, with $B_{L,c} = 10^{-1}R_b$, outperforms differential detection for the adaptive receiver. This is in stark contrast to the rather dismal results obtained in Chapter 7 where use of closed-loop carrier recovery was all but ruled out in combination with the adaptive receiver. The modified first-order open-loop estimator performs consistently worse than differential in this case.

To explain these unexpected results, it is important to point out the fundamental difference between the Costas loop scheme depicted in Figure 6.14 and the open-loop estimation receiver depicted in Figure 6.15 in their application to adaptive reception. Note that the Costas loop relies upon dedicated matched filter circuitry to compensate for phase and frequency errors. The open-loop estimator, however, relies upon the output of the adaptive filter itself to do the same.

Consider a situation where each receiver goes into a deep fade. Both receivers can be expected to do quite badly for a certain amount of time. The adaptive filter, in each case, will very likely get perturbed from its nearly optimal solution. Upon coming out of the fade, the Costas loop adaptive receiver has a decisive advantage. It will be able to quickly begin making very good estimates of the phase of the received signal again,

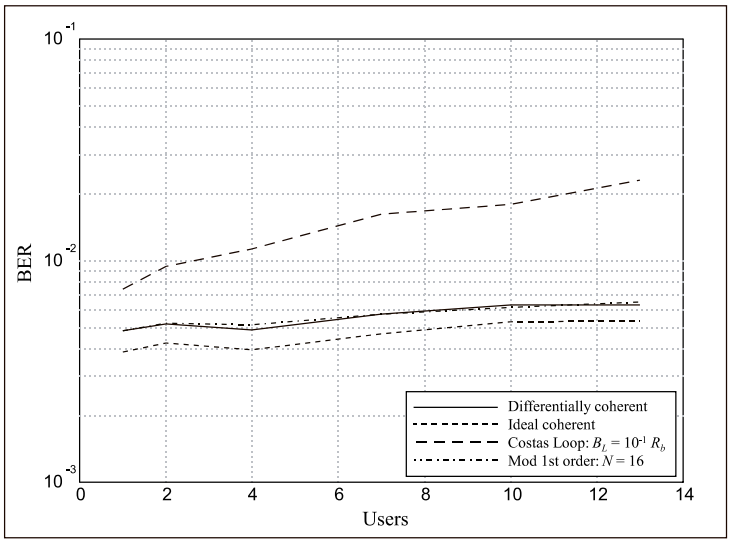

Figure 8.1: Simulation results for bit error probabilites vs. number of users on the forward link in flat Rayleigh-faded channel; $E_b/N_o = 20$ dB; performance of conventional receivers with "ideal" and differentially coherent reception, wide BW Costas loop and $N = 16$ modified 1st-order ML structure; freq. uncertainty, $2\sigma_f = 1/40R_b$; vehicle speed is 45 kph.

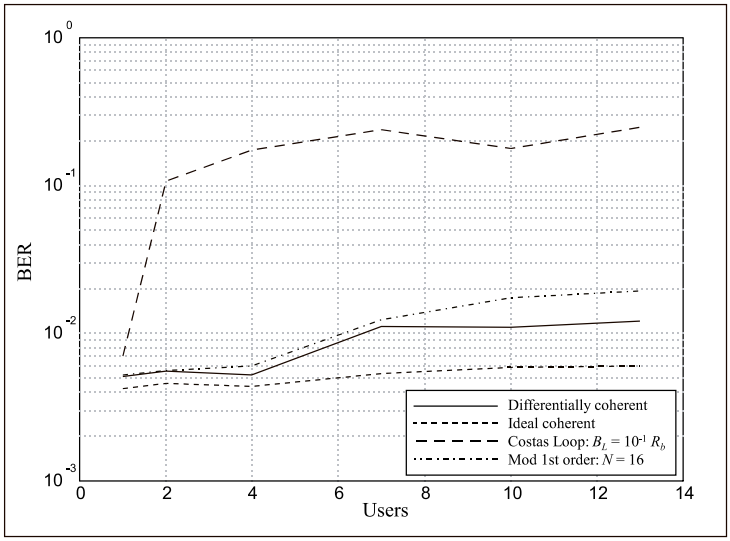

Figure 8.2: Simulation results for bit error probabilites vs. number of users on the forward link in flat Rayleigh-faded channel; $E_b/N_o = 20$ dB; performance of adaptive receivers with "ideal" and differentially coherent reception, wide BW Costas loop and $N = 16$ modified 1st-order ML structure; freq. uncertainty, $2\sigma_f = 1/40R_b$; vehicle speed is 45 kph.

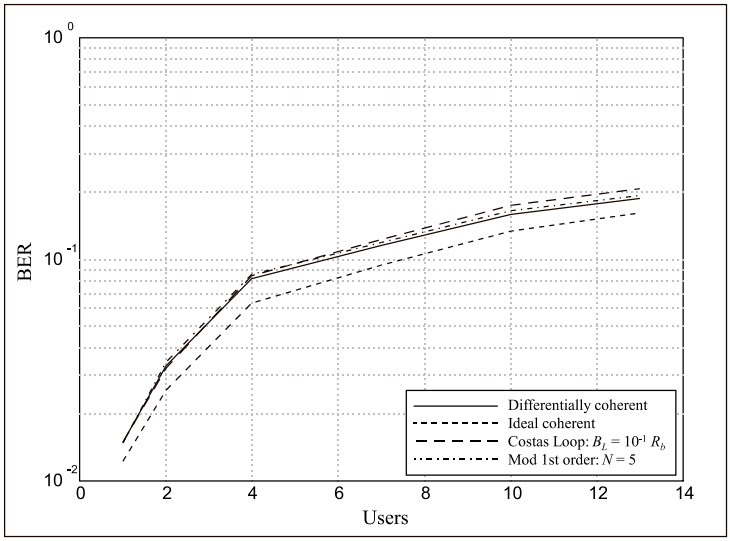

Figure 8.3: Simulation results for bit error probabilites vs. number of users on the reverse link in flat Rayleigh-faded channel; "strict" power control, $\sigma_P^2 = 2$ dB^2; $E_b/N_o = 15$ dB; performance of conventional receivers with "ideal" and differentially coherent reception, wide BW Costas loop and $N = 5$ modified 1st-order ML structure; freq. uncertainty, $2\sigma_f = 1/40R_b$; vehicle speed is 15 kph.

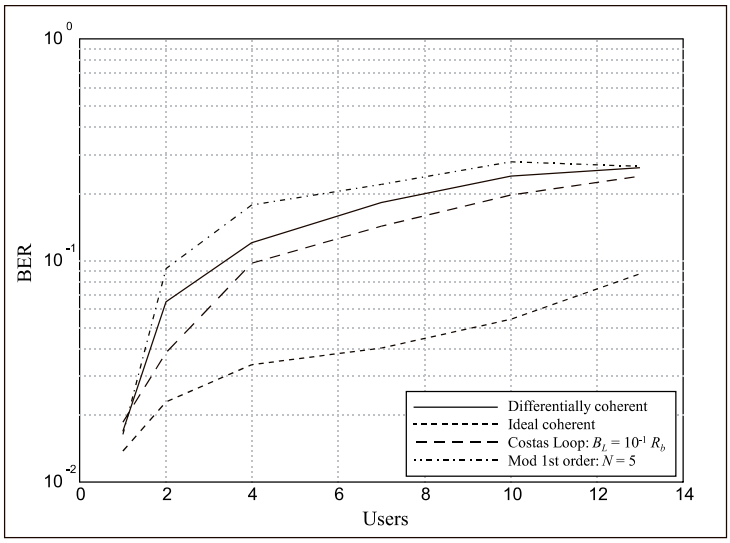

Figure 8.4: Simulation results for bit error probabilites vs. number of users on the reverse link in flat Rayleigh-faded channel; "strict" power control, $\sigma_P^2 = 2$ dB^2; $E_b/N_o = 15$ dB; performance of adaptive receivers with "ideal" and differentially coherent reception, wide BW Costas loop and $N = 5$ modified 1st-order ML structure; freq. uncertainty, $2\sigma_f = 1/40R_b$; vehicle speed is 15 kph.

regardless of the state of the adaptive filter. The open-loop estimation scheme as depicted in Figure 6.15, on the other hand, cannot quickly do so. The error in the adaptive filter will compound itself by failing to produce good phase estimates. This "double jeopardy" inherent to the latter receiver will increase the likelihood that the receiver makes a high density of symbol estimation errors, which, due to decision-directed adaptation, will in turn cause an increasingly worse adaptive solution and ultimately cause the receiver to fail. We believe this is precisely what is happening in Figure 8.4.

This suggests an additional receiver structure for future consideration: one in which an open-loop phase estimation structure is used but which utilizes the outputs of a dedicated matched filter instead of the adaptive filter. Investigation of such a structure was not possible for this work, however. Note that the rationale for using the adaptive filter as we have is to reduce the impact of MAI on the received symbols, which in turn yield the phase estimate. This impact, which is especially pernicious on the reverse link, as discussed in Chapter 7, can be significant to the open-loop phase estimation scheme.

8.2 The Two-Ray Rayleigh, "Frequency Selective" Channel

Although it has only two signal paths, the two-ray Rayleigh channel model chosen for this research is deceptively pernicious. The second signal component, as shown in Table 6.2, is only 6 dB down from the first-arriving faded component. Its delay of 5 μs, however, is what really causes problems for matched filter detection. In the system, this delay corresponds to approximately 10 chips, or about 2/3 a symbol period. In lieu of coherent combining, this dramatically increases the MAI seen at the output of a matched filter. It is in this section that we can introduce the recombining capabilities of adaptive reception. In addition, we introduce the performance of the differentially coherent, three-finger RAKE receiver, depicted in Figure 6.11, to provide the adaptive filter with a more fair comparison than that given by a simple matched filter. Simulations were run at E_b/N_o of 20, 24, and 28 dB, for vehicle speeds of 15 and 45 kph for both the forward link and the reverse link with power variances of 2 and 20 dB^2. Sections 8.2.1 and 8.2.2 discuss results obtained for the forward and reverse links respectively.

8.2.1 Performance on the Synchronous Forward Link

Figures 8.5 and 8.6 show the forward link performance of conventional and adaptive receivers respectively. In each case, the performance of the RAKE receiver is shown for the purposes of comparison. The bit energy to noise spectral density ratio is 28 dB,and vehicle speed

is 15 kph. For conventional matched filter receivers in Figure 8.5, no realizable carrier recovery strategies outperform the differentially coherent receiver. The Costas loop with $B_{L,c} = 10^{-1}R_b$ performs slightly worse than the modified first-order $N = 5$ phase estimator.

The adaptive receivers in Figure 8.6 once again produce a much more interesting result. Here, two realizable detection structures perform better than the "ideal" coherent receiver at a number of points. Specifically the differentially coherent and the $N = 5$ open-loop estimator perform better than "ideal" at 4 or fewer users. Remember that the definition of "ideal" carrier recovery in a multipath environment merely means that we assume the receiver has perfect knowledge at all times of the phase of the *first* arriving component, which is arbitrarily considered to have delay $\tau_1 = 0$. No knowledge is assumed about other paths. Clearly in this frequency-selective environment, realizable receivers, at least those equipped with an adaptive equalizer capable of coherently combining multipath, can do better than this "ideal" situation.

The wide bandwidth Costas loop applied to the adaptive receiver in Figure 8.6 performs quite poorly on the forward link. We are convinced that this is due to the dramatically increased jitter in the Costas error term induced by the MAI as described in Chapter 7. Note, finally, that at all numbers of users, the RAKE receiver outperforms all others. This is due to the fact that the RAKE receiver is a *better* recombiner of multipath than is the adaptive filter in this particular environment. Since second path is delayed by 2/3 of a baud period, only 1/3 of the energy in the second component is available in the time window of the adaptive filter.* The MAI, the mitigation of which is the primary purpose of the adaptive filter, is quite benign on the forward link. Borrowing the analogy of "interference-limited" versus "noise-limited," we denote this situation as "mulipath-limited" rather than "interference-limited." The dramatically better performance of the RAKE receiver versus all adaptive receivers is therefore not suprising.

8.2.2 Performance on the Asynchronous Reverse Link

Simulations results at $E_b/N_o = 28$ dB on the reverse link with "tight" power control are shown for conventional and adaptive receivers in Figures 8.7 and 8.8. Vehicle speed is 45 kph corresponding to a doppler frequency, $f_d = 85$ Hz. Once again, the curves for conventional receivers in Figure 8.7 tell us very little. In fact the RAKE receiver only deviates significantly from the performance of all the other receivers examined at 1 and 2 users.

*Extension of the adaptive filter to an arbitrary length, based on expected multipath delays, is quite feasible, but was not examined in this work.

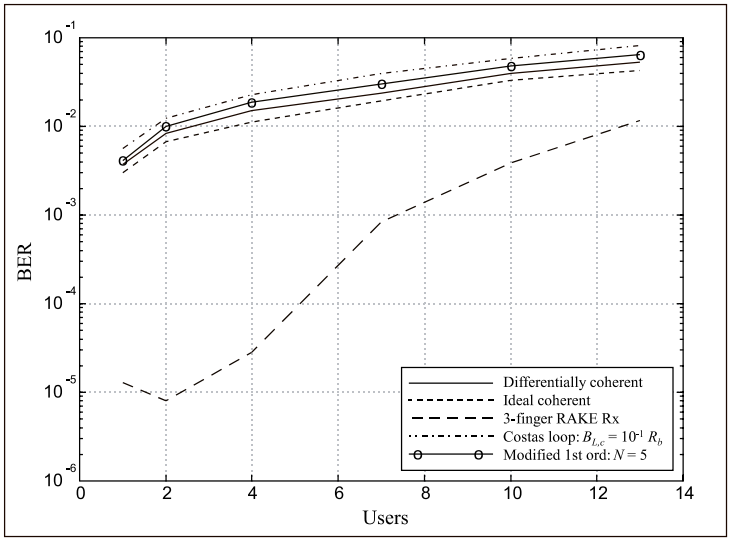

Figure 8.5: Simulation results for bit error probabilites vs. number of users on the forward link in 2-ray Rayleigh-faded, frequency-selective channel; $E_b/N_o = 28$ dB; performance of conventional receivers with "ideal" and differentially coherent reception, wide BW Costas loop and $N = 5$ modified 1st-order ML structure; 3-finger RAKE also shown; freq. uncertainty, $2\sigma_f = 1/40R_b$; vehicle speed is 15 kph.

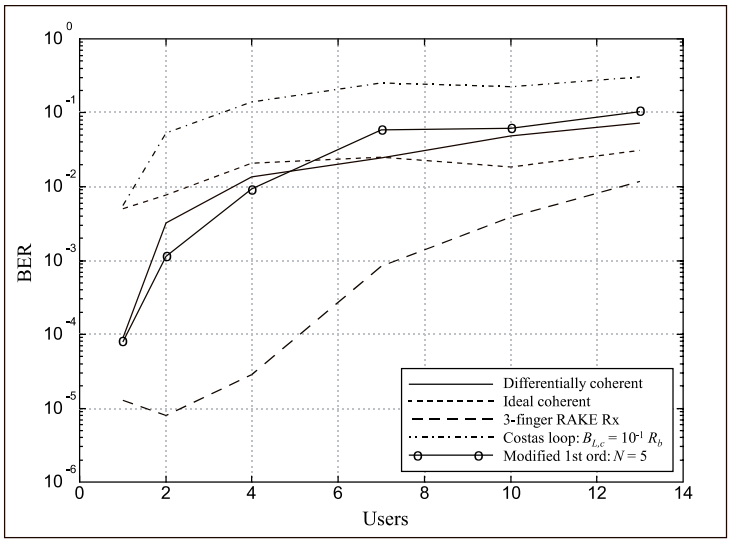

Figure 8.6: Simulation results for bit error probabilites vs. number of users on the forward link in 2-ray Rayleigh-faded, frequency-selective channel; $E_b/N_o = 28$ dB; performance of adaptive receivers with "ideal" and differentially coherent reception, wide BW Costas loop and $N = 5$ modified 1st-order ML structure; 3-finger RAKE also shown; freq. uncertainty, $2\sigma_f = 1/40R_b$; vehicle speed is 15 kph.

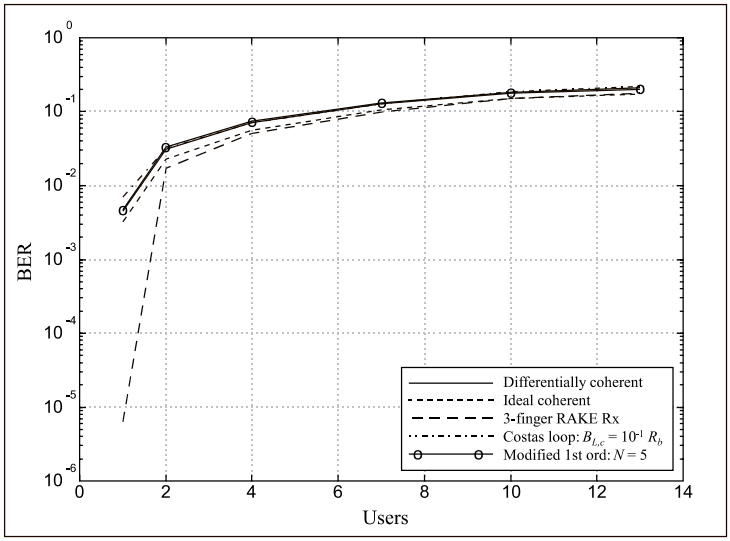

Figure 8.7: Simulation results for bit error probabilites vs. number of users on the reverse link in 2-ray Rayleigh-faded, frequency-selective channel; "strict" power control, $\sigma_P^2 = 2$ dB^2; $E_b/N_o = 28$ dB; performance of conventional receivers with "ideal" and differentially coherent reception, wide BW Costas loop and $N = 5$ modified 1st-order ML structure; 3-finger RAKE also shown; freq. uncertainty, $2\sigma_f = 1/40R_b$; vehicle speed is 45 kph.

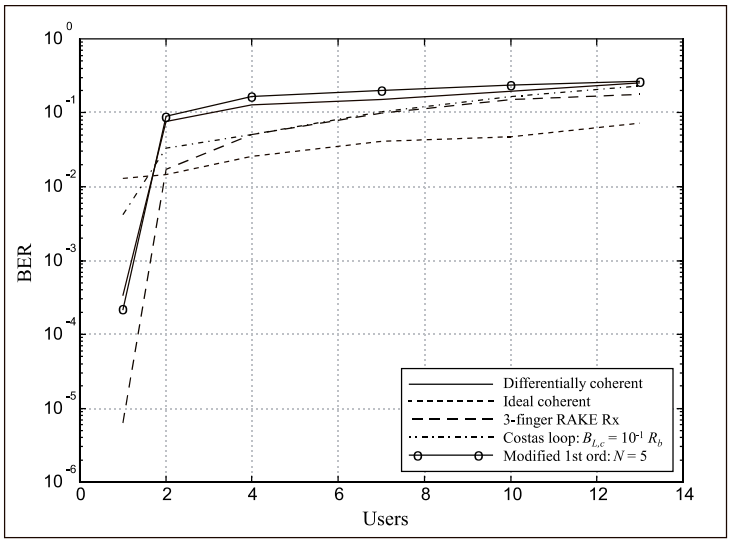

Figure 8.8: Simulation results for bit error probabilites vs. number of users on the reverse link in 2-ray Rayleigh-faded, frequency-selective channel; "strict" power control, $\sigma_P^2 = 2$ dB^2; $E_b/N_o = 28$ dB; performance of adaptive receivers with "ideal" and differentially coherent reception, wide BW Costas loop and $N = 5$ modified 1st-order ML structure; 3-finger RAKE also shown; freq. uncertainty, $2\sigma_f = 1/40R_b$; vehicle speed is 45 kph.

Results for the adaptive receivers, however, show us more illuminating results in Figure 8.8. Here the $N = 5$ open-loop estimator and the differentially coherent adaptive receivers perform almost identically. Note that at 1 user, these outperform the "ideal" coherent receiver by a wide margin. The performance of the adaptive receiver equipped with the parallel Costas loop structure is perhaps the most noteworthy. At all but one user, the performance of this receiver lies between that of differential and ideal coherent, which is precisely why we wish to do carrier recovery. Note also that in contrast to the forward link case in Figure 8.6, the adaptive receiver, at least the one with "ideal" coherent reception, now performs better than the RAKE receiver in all cases except one user.

8.3 The COST-207 "Typical Urban" Channel

Six distinct faded paths comprise the COST-207 "Typical Urban" channel. This is arguably the most challenging environment in which we examined the performance of the candidate receivers. As given from Table 6.2, the second arriving path is actually the strongest component, 3 dB higher than the first arriving ray. But note that since the delay of the second component, 0.2 μs, is less than one-half of the chip period of approximately 0.52μs, this really should not cause too big a problem for spread spectrum receivers. By the time we get out to the last path, arriving 5 μs later as in the two-ray Rayleigh model in section 8.2, the power is 10 dB down from the strongest component. So while "typical urban" model is certainly more complex than the two-ray case, we don't expect significantly worse results than obtained in the previous section. Simulations were run at E_b/N_o of 24 and 28 dB for both forward and reverse links, the results of which are given in sections 8.3.1 and 8.3.2 respectively. Vehicle speeds of 15 and 45 kph were considered, and for the reverse link, power variances of 2 and 20 dB^2 were examined.

8.3.1 Performance on the Synchronous Forward Link

Figures 8.9 and 8.10 show results on the forward link for the urban channel. Specific parameters for these plots include an E_b/N_o of 24 dB and a vehicle speed of 45 kph. The performance of all the single-path conventional receivers shown in Figure 8.9 is almost identical. Interestingly, the "ideal" coherent matched filter receiver performs worst. This is likely due to the fact that the "ideal" coherent tracker is tracking the first arriving component. Since this ray is weaker than both the second and third, it is not surprising that performance so degrades. As would be expected the three-finger RAKE receiver dramatically improves the performance on the channel.

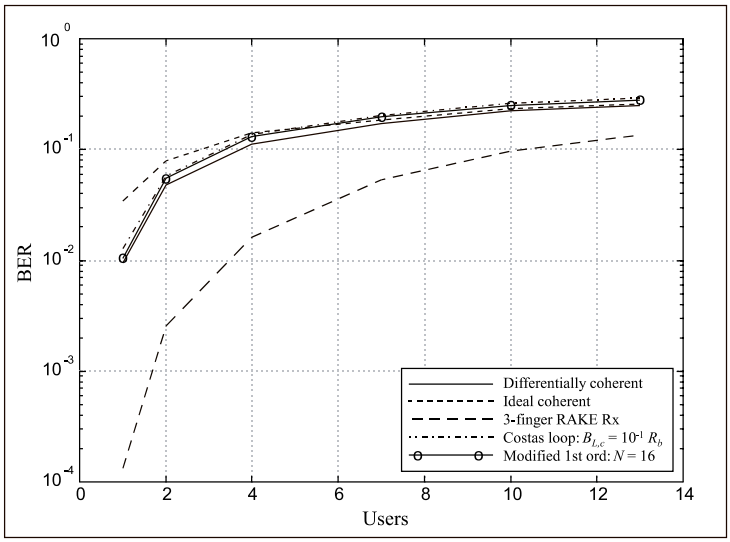

Figure 8.9: Simulation results for bit error probabilites vs. number of users on the forward link in COST-207 "Typical Urban" channel; $E_b/N_o = 24$ dB; performance of conventional receivers with "ideal" and differentially coherent reception, wide BW Costas loop and $N = 16$ modified 1st-order ML structure; 3-finger RAKE also shown; freq. uncertainty, $2\sigma_f = 1/40R_b$; vehicle speed is 45 kph.

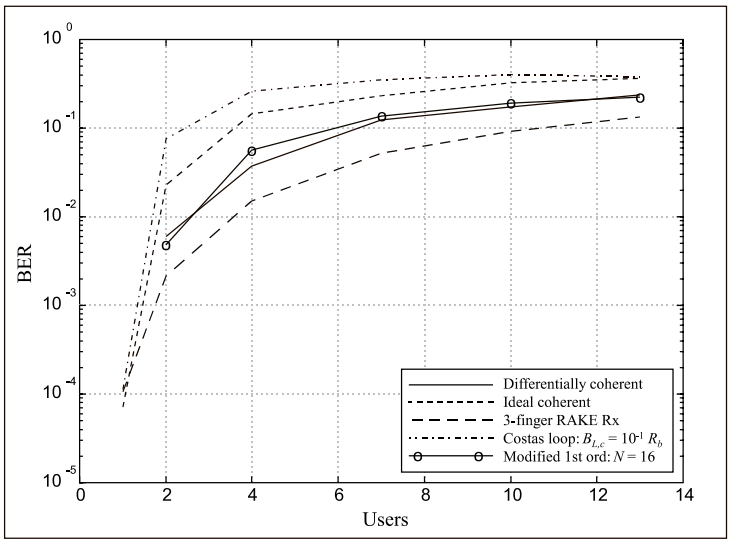

Figure 8.10: Simulation results for bit error probabilites vs. number of users on the forward link in COST-207 "Typical Urban" channel; $E_b/N_o = 24$ dB; performance of adaptive receivers with "ideal" and differentially coherent reception, wide BW Costas loop and $N = 16$ modified 1st-order ML structure; 3-finger RAKE also shown; freq. uncertainty, $2\sigma_f = 1/40R_b$; vehicle speed is 45 kph.

Results for the adaptive receivers shown in Figure 8.10 allow more discrimination between the different receiver structures. The RAKE still performs best over a wide range of users. The performances of differentially coherent and $N = 16$ open-loop phase estimator receivers are almost equivalent, and no errors were generated for either at one user, suggesting BERs in the range of 10^{-7}. Again the ideal coherent performs pretty badly, based on the now less than ideal assumption regarding "ideal" coherent carrier recovery. Only the Costas loop with $B_{L,c} = 10^{-1}R_b$ performs worse.

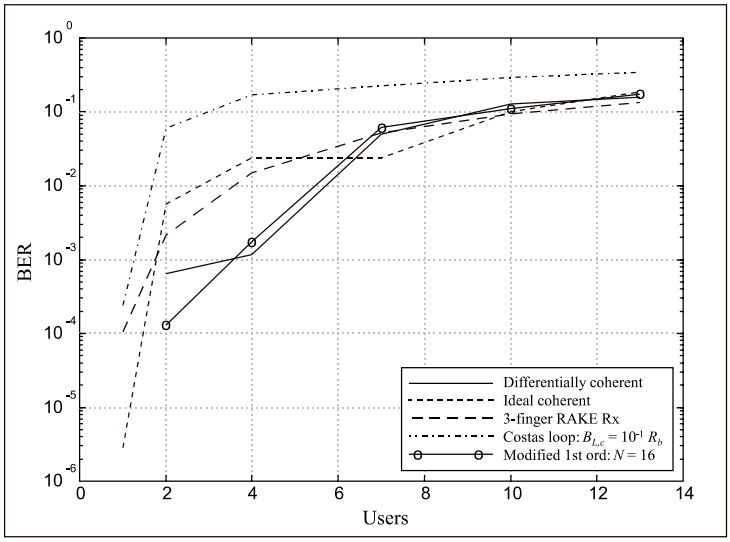

Figure 8.11: Results for the same conditions given in Figure 8.10, except at a slower vehicle speed of 15 kph.

In this particular channel model, it is quite interesting to see the results for adaptive filter receivers under conditions of the lower vehicle speed of 15 kph. Conventional receivers as well as the RAKE show little change and are not therefore plotted. But for the adaptive receivers, dramatic changes in the relative performance between receivers can be seen in Figure 8.11. In stark contrast to Figure 8.10, now the "ideal," differential, and open-loop phase estimator receivers perform significantly better than the RAKE over a range of users from 1 to about 7. This reinforces our earlier assertion of the ability of adaptive receivers to combine multipath in addition to suppressing spread-spectrum MAI. Note again that the differentially coherent and $N = 16$ open-loop receivers achieved no errors for one user, suggesting a BER less than 10^{-7}.

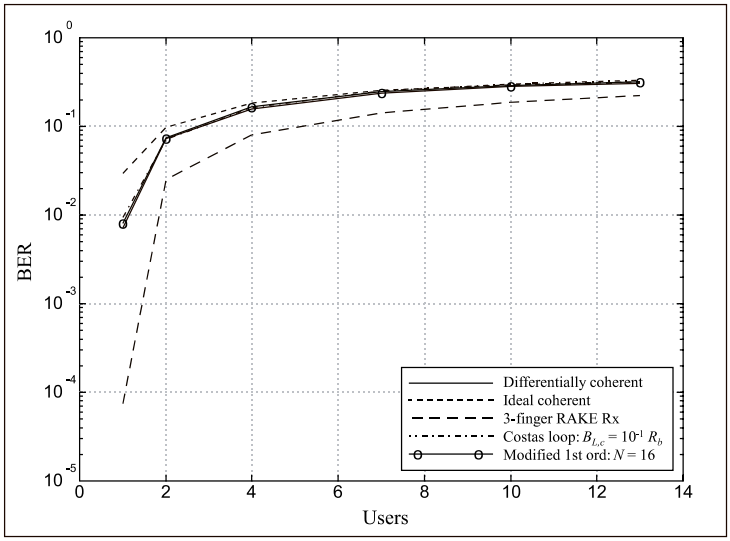

Figure 8.12: Simulation results for bit error probabilites vs. number of users on the reverse link in COST-207 "Typical Urban" channel; $E_b/N_o = 24$ dB; "strict" power control, $\sigma_P^2 = 2$ dB^2; performance of conventional receivers with "ideal" and differentially coherent reception, wide BW Costas loop and $N = 16$ modified 1st-order ML structure; 3-finger RAKE also shown; freq. uncertainty, $2\sigma_f = 1/40R_b$; vehicle speed is 15 kph.

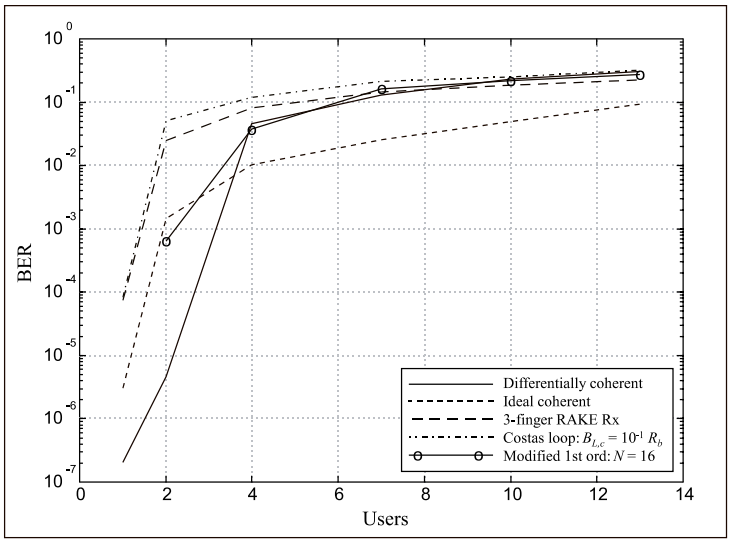

Figure 8.13: Simulation results for bit error probabilites vs. number of users on the revers link in COST-207 "Typical Urban" channel; $E_b/N_o = 24$ dB; "strict" power control, $\sigma_P^2 = 2$ dB^2; performance of adaptive receivers with "ideal" and differentially coherent reception, wide BW Costas loop and $N = 16$ modified 1st-order ML structure; 3-finger RAKE also shown; freq. uncertainty, $2\sigma_f = 1/40R_b$; vehicle speed is 15 kph.

8.3.2 Performance on the Asynchronous Reverse Link

For the reverse link, we show results in a system with a "tight" power variance of 2 dB^2 at a received E_b/N_o of 28 dB for the SOI, prior to fading. These are given in Figures 8.12 and 8.13 for conventional and adaptive receivers respectively. Vehicle speed is 15 kph. The conventional receivers again show little discrimination between various receiver structures with only the RAKE receiver performing slightly better. Again, the "ideal" coherent receiver performs worst of all.

Results for the adaptive receivers in Figure 8.13 again show the "ideal," differential, and $N = 16$ modified first-order open-loop estimator performing much better than the RAKE. While it is encouraging to see at least two realizable receivers perform better than the three-finger RAKE, we note with some disappointment how much better the "ideal" coherent receiver performs for 4 to 13 users than all others. It has been our hope that realizable carrier recovery structures could come close to this peformance or even exceed it under certain conditions. Figure 8.13 shows once again how very difficult and elusive this goal has been.

8.4 The COST-207 "Typical Rural" Channel

The rural channel provides a slightly different view of the receiver structures examined in this work. The first of four, arriving rays is assumed to have a Ricean fading envelope, wherein a strong line-of-sight (LOS) component exists. Since the rays are very tightly spaced, this is not a channel that we expect the adaptive receivers, with fractional sampling of only two samples per chip, to be able to combine multipath. This limits the ability of the adaptive, fractionally-spaced receivers to resolve the first from the second component, and the third from the fourth. Nevertheless MAI is still mitigated to some extent, and we therefore see the adaptive receivers giving a small improvement over the conventional matched filter. Simulations were run for forward and reverse links at E_b/N_o of 24 and 28 dB for the SOI prior to fading. On the reverse link only the "tight" power control situation with power variance of 2 dB^2 was examined. Simulations were run on both links for vehicle speeds of 15 and 45 kph.

8.4.1 Performance on the Synchronous Forward Link

Figures 8.14 and 8.15 show the forward link results for conventional and adaptive receivers, respectively, at an E_b/N_o of 24 dB and a vehicle speed of 45 kph. For the conventional

receivers in Figure 8.14, there is not much new information. The RAKE receiver dramatically outperforms all single-path matched filter receivers, and the Costas loop and $N = 5$ open-loop estimation receiver are unable to do better than the differentially coherent. The "ideal" coherent receiver, as it did for the urban channel forward link in section 8.3.1, performs quite badly for the conventional receivers as well as the adaptive receivers in Figure 8.15.

The results for the adaptive filters are, as they have usually been, slightly more illuminating. As we can see in Figure 8.15, the $N = 5$ receiver does quite well and outperforms differentially coherent detection for 1 and 2 users. Still the RAKE receiver does better than all adaptive receivers and is therefore recommended for the forward link in a rural channel.

8.4.2 Performance on the Asynchronous Reverse Link

Very little discriminatory information concerning carrier recovery was gained in examination of the reverse link in the rural channel. Figures 8.16 and 8.17 show results at $E_b/N_o = 24$ dB with a vehicle speed of 45 kph for conventional and adaptive receivers respectively. The conventional receivers in Figure 8.16 are very closely bunched together at all but one user. The "ideal" coherent again performs slightly worse than the others.

However, in Figure 8.17, for the adaptive receivers, "ideal" coherent performs better than all other receivers for a wide range of users. This is in stark contrast to the other results obtained in this section and in the section prior wherein the first arriving ray is *not* the strongest. We believe this is because the first arriving component in this particular channel is assumed to have a Ricean spectral density. The LOS component present in the first arriving ray may, at least in this instance, be sufficient to tip the balance and enable "ideal" coherent recovery to perform well once again. Differentially coherent and $N = 5$ open-loop estimation receivers once again perform almost equivalently.

The Costas loop with $B_{L,c} = 10^{-1}R_b$, on the other hand, outperforms both of these and, in fact, along with the "ideal" coherent receiver, outperforms even the RAKE for a wide range of users. Given that one of our major research goals has been to find realizable carrier recovery structures for adaptive receivers that are capable of "buying back" the performance generally lost in going from "ideal" to differentially coherent, we consider the performance of this Costas loop in this situation to be one of the bright spots.

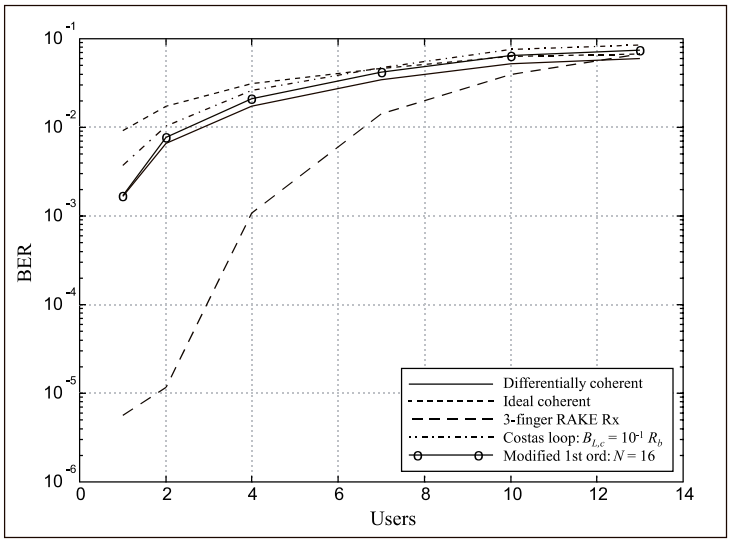

Figure 8.14: Simulation results for bit error probabilites vs. number of users on the forward link in COST-207 "Typical Rural" channel; $E_b/N_o = 24$ dB; performance of conventional receivers with "ideal" and differentially coherent reception, wide BW Costas loop and $N = 5$ modified 1st-order ML structure; 3-finger RAKE also shown; freq. uncertainty, $2\sigma_f = 1/40R_b$; vehicle speed is 45 kph.

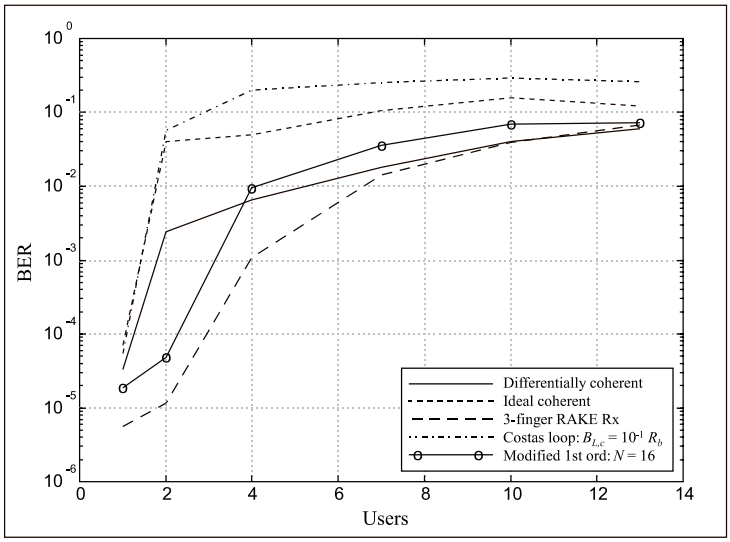

Figure 8.15: Simulation results for bit error probabilites vs. number of users on the forward link in COST-207 "Typical Urban" channel; $E_b/N_o = 24$ dB; performance of adaptive receivers with "ideal" and differentially coherent reception, wide BW Costas loop and $N = 5$ modified 1st-order ML structure; 3-finger RAKE also shown; freq. uncertainty, $2\sigma_f = 1/40R_b$; vehicle speed is 45 kph.

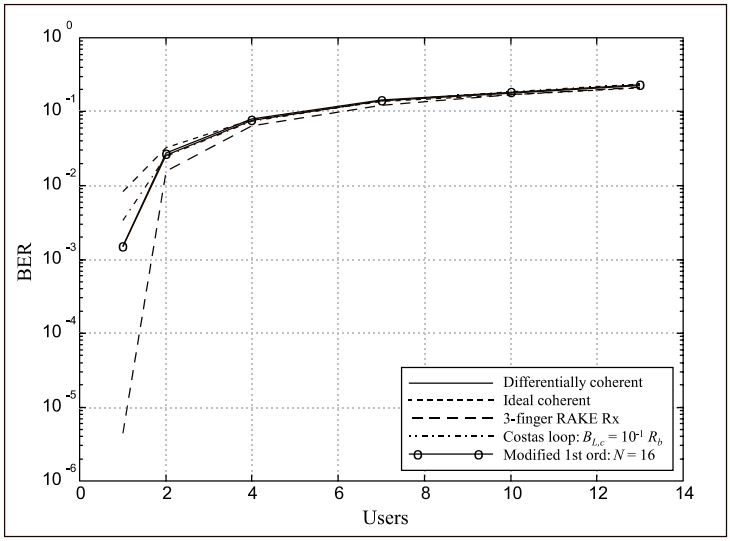

Figure 8.16: Simulation results for bit error probabilites vs. number of users on the reverse link in COST-207 "Typical Rural" channel; $E_b/N_o = 24$ dB; "strict" power control, $\sigma_P^2 = 2$ dB^2; performance of conventional receivers with "ideal" and differentially coherent reception, wide BW Costas loop and $N = 5$ modified 1st-order ML structure; 3-finger RAKE also shown; freq. uncertainty, $2\sigma_f = 1/40R_b$; vehicle speed is 45 kph.

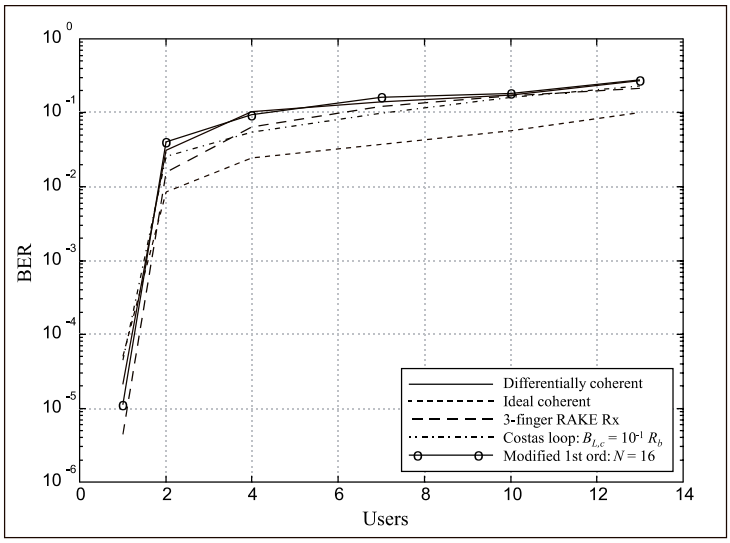

Figure 8.17: Simulation results for bit error probabilites vs. number of users on the forward link in COST-207 "Typical Rural" channel; $E_b/N_o = 24$ dB; "strict" power control, $\sigma_P^2 = 2$ dB^2; performance of adaptive receivers with "ideal" and differentially coherent reception, wide BW Costas loop and $N = 5$ modified 1st-order ML structure; 3-finger RAKE also shown; freq. uncertainty, $2\sigma_f = 1/40R_b$; vehicle speed is 45 kph.

8.5 The Effect of Training Period and Frequency Offset on Receiver Performance

As noted in Chapter 6, we have made stringent sycnhronization and training requirements on the receivers examined for this research. Moreover, we have assumed a rather large uncertainty in carrier frequency. Throughout the discussion of results in both this chapter and the last, we have often remarked that these two factors might play a role in producing the less than stellar results obtained and most importantly, the unacceptably high failure rates of many adaptive receivers. In this section, we relax these parameters and examine the system in slightly more forgiving conditions. It is hoped that modifying these simulation parameters would provide additional information regarding receiver performance. Alas, for reasons to which we can now only speculate, this will turn out *not* to be true in the sections below. First in section 8.5.1, we change one simulation parameter, viz., the length of the period given for receiver training and synchronization, and examine the difference achieved in BER results. Then in section 8.5.2, we dramatically reduce the frequency uncertainty in the simulations and consider the impact this has on receiver performance.

8.5.1 The Impact of Training and Synchronization Period

The first modification was to allow 1000 training symbols for the adaptive filters, as opposed to 100 given in previous trials. This is a generous allowance of time for an adaptive filter to converge, but is not unthinkably long when considering a telephony application where millions of bits could be transmitted over a link after call setup and synchronization is acheived. We examined both reverse and forward links with this parameter change in the two-ray Rayleigh fading model examined in section 8.2.

To our disappointment, this relaxation provided virtually no improvement in performance for any of the receiver structures under consideration. We expected the adaptive receivers to perform better given this additional training period, but as can be seen in Figures 8.18 and 8.19, which show results for the forward and reverse links respectively, this simply was not the case. For the forward link in Figure 8.18, the results are almost exactly the same as those obtained in the very similar conditions of Figure 8.6. No additional information concerning carrier recovery or receiver performance can be drawn. Similarly, results for the reverse link under tight power control with the 1000 bit training period, shown in Figure 8.19, are almost exactly the same as those seen under identical conditions in Figure 8.8 where only 100 such bits were allowed.

From these disappointing results, it is clear that the length of training period given

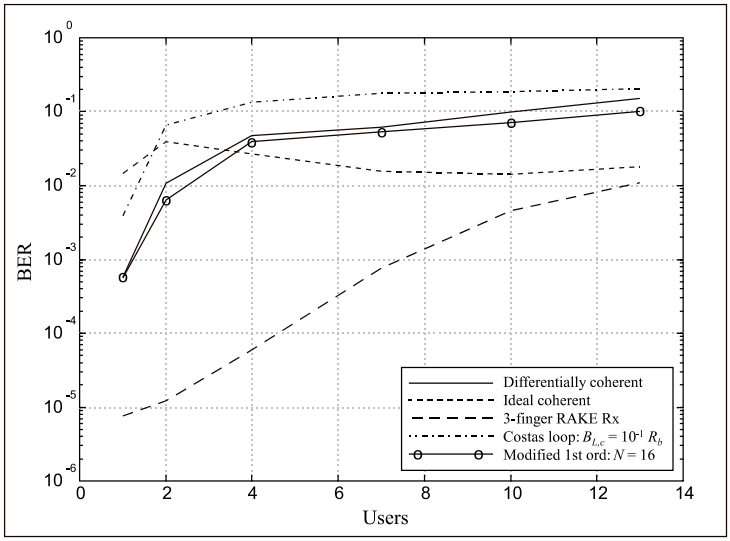

Figure 8.18: Simulation results for bit error probabilites vs. number of users on the forward link in 2-ray Rayleigh channel; 1000 bits allowed for training & synch.; $E_b/N_o = 28$ dB; performance of adaptive receivers with "ideal" and differentially coherent reception, wide BW Costas loop and $N = 5$ modified 1st-order ML structure; 3-finger RAKE also shown; freq. uncertainty, $2\sigma_f = 1/40R_b$; vehicle speed is 45 kph.

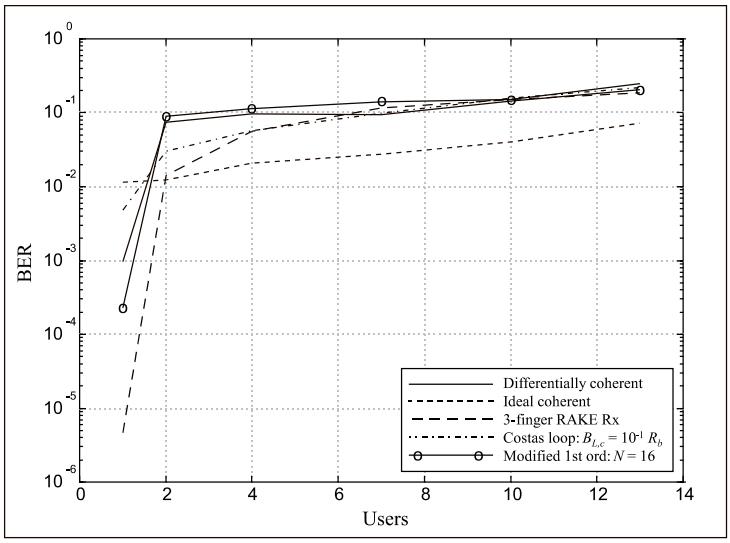

Figure 8.19: Simulation results for bit error probabilites vs. number of users on the reverse link in 2-ray Rayleigh channel; 1000 bits allowed for training & synch.; "strict" power control; $E_b/N_o = 28$ dB; performance of adaptive receivers with "ideal" and differentially coherent reception, wide BW Costas loop and $N = 5$ modified 1st-order ML structure; 3-finger RAKE also shown; freq. uncertainty, $2\sigma_f = 1/40R_b$; vehicle speed is 45 kph.

for the adaptive receiver does not significantly impact the very bad BER and high failure rates seen in previous sections of this chapter. We next turn attention to the frequency uncertainties assumed in this work to see if new results here can shed any light on this problem.

8.5.2 The Impact of Frequency Uncertainty

Simulations throughout chapters 7 and 8 up to this point have assumed a frequency uncertainty, $2\sigma_f = 3200$ Hz, equal to $1/40R_b$, for the SOI. We relaxed this parameter by one order of magnitude to 320 Hz. This is a reasonable figure given a more accurate, and thus slightly more expensive, set of oscillators are available for any particular receiver design. We then re-examined the receivers in the two-ray Rayleigh channel as in section 8.5.1. The results appear in Figures 8.20 and 8.21 for the forward and reverse links respectively. We had hoped that the relaxation of the relatively wide frequency offsets would result in better BER performance of at least some of the receivers and lower failure rates for the adaptive receivers. Once again this is not the case.

The forward link results shown in Figure 8.20 show no significant departure from those obtained in similar conditions for Figure 8.6. BERs are similar, and the relative performance between users remains essentially unchanged. This observation can be extended to the reverse link results shown in Figure 8.21 where there is similarly little departure from those shown in Figure 8.8. The failure in this and the preceding subsection to obtain an explanation for high BER and adaptive receiver failure rates suggests that there are more fundamental challenges to the design of CDMA receivers employing adaptive interference suppression, and further study is needed on this problem. We will suggest briefly in Chapter 9 that more advanced algorthims are needed, and the linking of equalization to channel coding should provide fertile ground in which to examine this issue.

8.6 Chapter Summary

In this chapter, we have presented selected results from the many hundreds of simulation points that were run in a variety channels for this research. We examined receiver performance for the flat fading case in section 8.1 and then moved on to examine frequency selective environments in sections 8.2 through 8.4. The most noteworthy finding in this chapter is arguably the difficulty the adaptive receivers had in fading channels. We digressed briefly in section 8.5 from the original simulation parameters in an attempt to explain this lackluster behavior. It was, however, to no avail and leaves us no choice but

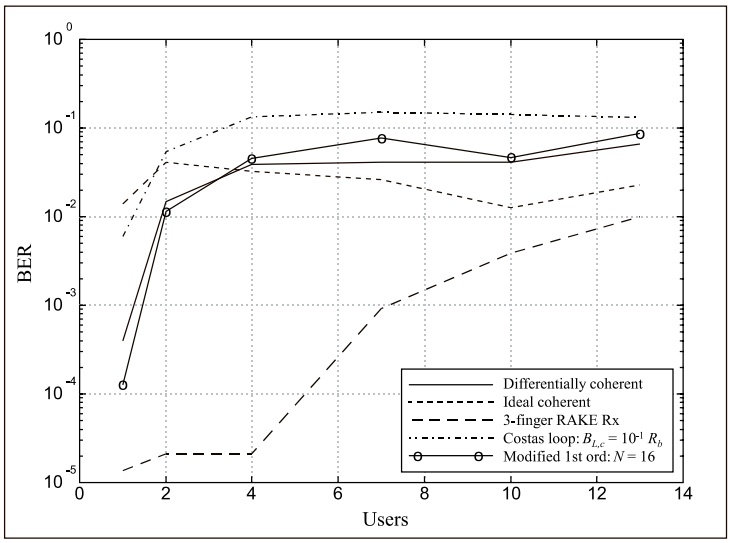

Figure 8.20: Simulation results for bit error probabilites vs. number of users on the forward link in 2-ray Rayleigh channel; lower frequency offset assumed, $2\sigma_f = 1/400R_b$; $E_b/N_o = 28$ dB; performance of adaptive receivers with "ideal" and differentially coherent reception, wide BW Costas loop and $N = 5$ modified 1st-order ML structure; 3-finger RAKE also shown; vehicle speed is 45 kph.

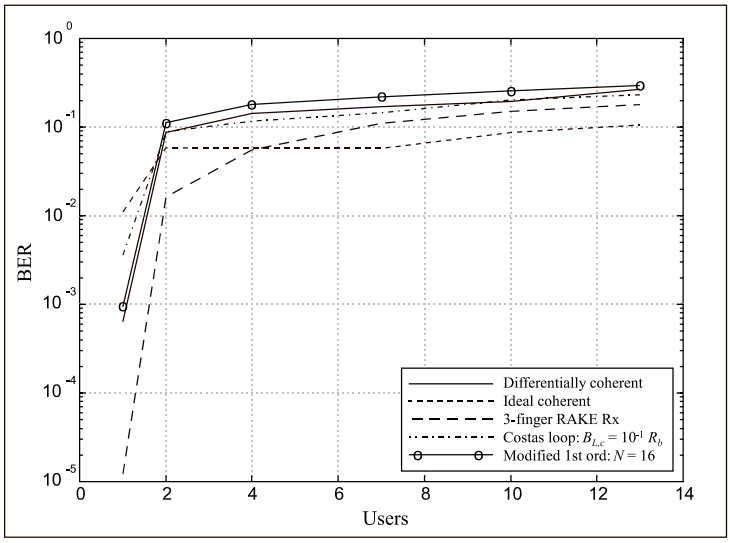

Figure 8.21: Simulation results for bit error probabilites vs. number of users on the reverse link in 2-ray Rayleigh channel; lower frequency offset assumed, $2\sigma_f = 1/400R_b$; "strict" power control; $E_b/N_o = 28$ dB; performance of adaptive receivers with "ideal" and differentially coherent reception, wide BW Costas loop and $N = 5$ modified 1st-order ML structure; 3-finger RAKE also shown; vehicle speed is 45 kph.

to recommend further study of realizable carrier recovery techniques suitable for receivers employing adaptive interference suppression.

Based on the observations in this chapter, the best performing realizable carrier recovery structures are the $N = 5$ and $N = 16$ modified first-order phase estimator for the forward CDMA link and a Costas loop with $B_{L,c} = 10^{-1}R_b$ for the reverse link. Both of these proved capable of beating the performance of the differentially coherent receiver, at least some of the time, on the respective links. These can thus be said, at least under certain conditions, to "buy back" part of the performance degradation between ideal coherent and differential reception.

Chapter 9

Conclusions

We set out very early in this research to see if carrier recovery structures could be found to work in CDMA environments. Specifically, we sought such structures that could "buy back" the well-known performance degradation caused by resorting to a simpler differentially coherent reception scheme. That this degradation seemed to be wider in systems employing adaptive interference suppression further motivated and broadened the work. The research began in Chapter 2 by surveying the available literature concerning synchronization, especially where this historical knowledge had been applied to suppressed-carrier recovery. Digestion of these concepts led to the introductory material provided in Chapters 3 through 5. With this knowledge as a foundation, we sought in Chapter 6 to apply it to the nomination of candidate receiver structures and candidate carrier recovery algorithms for the specific conditions of interest—a typical CDMA cellular system. Investigation via simulation was then carried out in Chapters 7 and 8 for both forward and reverse links in a variety of realistic mobile environments.

In this chapter, we review the salient points of the research process described above. In section 9.1, these points are broken up into a set of more theoretical contributions, and a set of more practical observations. Then in section 9.2, we conclude this thesis with recommendations for future research strategies—promising areas of investigation that time does not permit us to explore further in this work.

9.1 Significant Contributions and Findings of this Research

9.1.1 Theoretical Contributions

The major contributions of this work may be delineated by those of a theoretical nature and those of a more practical nature—the bulk of them belonging to the latter category. With

regard to substantive theory, the concise development of discrete-time transfer functions in Chapter 3, for PLL loop filters in terms of classical and intuitively understandable analog PLL paramaters, was the first major contribution of this work. These expressions allow designers of digital systems to very quickly specify parameters for a discrete-time, digitally implemented PLL that will have performance predicted by theory.

The exposition of several open-loop carrier phase estimation schemes based upon the maximum likelihood (ML) principle in Chapter 4 was our second major theoretical contribution—and perhaps the most important. The development of the decision feedback open-loop estimator based upon a high-SNR assumption in the ML equation given by (4.18) in that chapter is, to our knowledge, unique. Further, the evaluation of first- and second-order error statistics for both squaring and decision feedback structures shown in Figures 4.6 and 4.7 is unique to this work. That these statistics converged to those expected for the Costas loops with "squaring" and with I-channel hard-limiting provided a new and important insight into open-loop ML phase estimation structures. Finally, the development of a notion of "loop bandwidth" for such structures was original to this work and will hopefully prove helpful to future researchers.

9.1.2 Experimental Contributions

Experimental contributions of this research have been numerous. The first such contribution was the marriage of open-loop ML phase estimation schemes to the fractionally-spaced adaptive CDMA receiver first mentioned in section 4.2.7. This came very early in our research as a result of applying the estimation schemes presented in [41] to the general equalization strategies proposed in [51] for differentially coherent detection. It turned out to be a very robust receiver structure in the examinations performed in Chapters 7 and 8. From the very beginning, its performance served as a benchmark to be beaten by any and all realizable carrier recovery techniques.

In Chapter 5, after a brief introduction to the topic of automatic frequency control (AFC), we looked in some depth at the notion of combining AFC with a Costas loop by summing the outputs of respective loop filters. Although this idea is at least 20 years old, no known references have addressed the issue of the degradation of the Costas phase estimate due to the presence of the AFC as we did in section 5.4. This was observed in a few representative simulations. Framing the discussion in terms of Costas and AFC loop bandwidths, we were able to posit some general guidelines for the design of such a system that were not apparently well-known.

In Chapter 6, we spent a great deal of effort in helping to define the simulation procedures

and assumptions for this research. We specified a CDMA system where bit energy to noise or interference spectral density ratios were expected to be quite low. In narrowing down the field of candidate carrier recovery structures and algorithms to be applied to such an environment, we were able to observe major drawbacks to some of them. All receivers employing AFC were disqualified due to their poor performance in high noise or when AFC loop bandwidth was sufficiently narrow for the noise conditions, their unacceptably long acquisition time. We observed that AFC loops ought be reserved for situations in which the input SNR is sufficiently high, well above 10 dB, or in situations where the frequency uncertainty is very wide and the acquisition time of an AFC loop with even with a narrow bandwidth constraint will still be necessary. Neither of these conditions were examined in our simulation work.

We further noted in Chapter 6 that the second-order ML phase estimation structure proposed in Chapter 4, i.e., one implementing a dedicated frequency estimation loop, seemed to perform no better in the conditions in question than the modified first-order estimation structure. We observed, in fact, that for large N, the second-order structure performed significantly worse than the other. We suggested that this was probably due to the fact that jitter in the frequency estimate is multiplicative over the N-tap delay line in the second-order estimator. Such jitter can be reduced arbitrarily by making the forgetting factor β closer to unity but is paid for by an increasingly long acquisition period for the second-order loop. This is not a penalty incurred by the modified first-order estimator. For this reason, we applied no further investigation to the second-order structure and submitted that it be reserved for situations of far more extreme carrier offsets.

Chapters 7 and 8 finally brought us to the long-awaited simulation experiments for the final candidate receiver structures and carrier recovery algorithms. In Chapter 7, we addressed some of the problems expected when applying the candidate carrier recovery algorithms to CDMA environments. We observed in section 7.2.1 that Costas loops could particularly be expected to have difficulty on a synchronous spread-spectrum multiple-access forward link due to the rapid amplitude fluctuations due to MAI of the received samples. The open-loop structures examined avoid this weakness on the forward link since a distinct complex signum operation essentially eliminated this problem. We consquently observed that the Costas loop almost universally performed poorer than all other algorithms on the forward CDMA link at all points except one user. This is so in spite of the relatively small level of forward link MAI contributed by each user in our simulations.

The open-loop schemes on the other hand showed some promise on the forward link

in AWGN. The $N = 5$ modified first-order phase estimation structure significantly outperformed the differentially coherent adaptive receiver over a wide range of users at E_b/N_o of 10 dB (Figure 7.9) and performed slightly better than differentially coherent reception when applied to conventional matched filter receivers (Figure 7.8).

On the asynchronous CDMA reverse link, a new set of challenges is encountered. It was shown in section 7.3.1 that a potentially strong estimator bias can occur due to the squaring operation of our open-loop estimation schemes. Thus, we noted that the schemes derived from the ML principle in AWGN, single-user environments, are no longer ML when applied to CDMA. In reverse link situations of both "tight" power control, $\sigma_P^2 = 2\text{dB}^2$, and "loose" power control, $\sigma_P^2 = 20\text{dB}^2$, we found very little consistent improvement to be gained by implementing carrier recovery versus simply using differentially coherent detection. At $E_b/N_o = 8$ dB in an AWGN channel under tight power control, we saw a wide bandwidth Costas loop, $B_{L,c} = 10^{-1}R_b$, give slight improvement over DPSK for conventional receivers but none at all for adaptive receivers. The $N = 5$ modified first-order open-loop estimation structure provided some performance enhancement for the adaptive filters in this situation. In "loose" power control, near-far conditions, no realizable carrier recovery structures were able to outperform DPSK in AWGN.

In fading channels, based on the observations in Chapter 8, we continued to see the poorest performance in traditional Costas loops for either conventional matched filter or adaptive filter receivers in forward link situations. Only open-loop estimation schemes were able to beat differential detection on the forward link and this only some of the time. Typically this improvement was seen for a relatively small number of users. On the reverse link in fading channels, the Costas loop redeemed itself, outperforming the open-loop estimation receivers most of the time and outperforming differential detection some of the time. See, for example, the results for flat fading in Figure 8.4 and those of the two-ray Rayleigh faded channel in Figure 8.8 where the Costas loop performance curve lies between that of "ideal" and differentially coherent reception for nearly all numbers of users. That this improvement was seen in adaptive receivers even more than in conventional receivers was somewhat unexpected.

9.2 Recommendations for Future Work

While a representative variety of structures in a wide variety of conditions have been examined in this work, its observations have in many ways only scratched the surface of the issues concerning carrier recovery in CDMA systems. In this section, we therefore endeavor to expose the shortcomings of our work with the goal of motivating future directions for research.

Many of these recommendations have been hinted at throughout the previous chapters. We summarize them here, delineating each as belonging to one of two broad categories: 1) broadening the scope of the carrier recovery investigation to produce more interesting results, and 2) finding new methods to increase the robustness of adaptive equalization for spread-spectrum MAI suppression.

9.2.1 Broadening the Scope of Investigation

As has been alluded to abundantly in previous chapters, the performance degradation between ideal coherent and differentially coherent reception of PSK is minimal for sparse signal constellations such as $M = 2$. Binary phase signalling is incredibly robust to phase jitter and thus, in the conditions assumed for this work, the widest bandwith systems, the $B_{L,c} = 10^{-1}R_b$ Costas loop and its corresponding $N = 5$ phase estimation structure, have consistently performed best of all realizable carrier recovery systems. For higher-order signal constellations, we could expect just the opposite result to be true. Extending the investigation to QPSK, 8-PSK, and QAM systems is likely to result in observations quite different from those obtained in this present research.

Similarly, the assumptions in this work of low bit energy to noise and interference spectral density ratios as well as relatively large frequency offsets proved prohibitive for a large class of receiver strucutres that would otherwise have been worthy of investigation. AFC was left relatively untouched due especially to the high noise densities. Narrower bandwidth Costas loops were not seriously examined due to their inability to acquire quickly in the presence of a large frequency offset. Future investigations ought to investigate more forgiving E_b/N_o ratios and smaller frequency offsets that would go hand-in-hand with the higher-order signal constellations suggested in the paragraph above.

The amplitude jitter problem for Costas loops on a single-carrier forward link signal, as discussed in section 7.2.1, brings up a significant oversight in this work. In highsight, the digital tanlock loop (DTL) introduced in section 4.1.6 might well have proved an interesting work-around to this pernicious problem. Since the phase detector (PD) in the DTL is an explicit arctangent operation, its performance is expected to be invariant to amplitude fluctuations. Since it is a relatively obscure carrier recovery technique with only a small handful of papers addressing it, a relative lack of attention was given it. In defense of our lack of regard, we point out that an explicit four-quadrant arctangent operation is a rather exotic scheme for real-time systems. Even on a DSP, the processing required for such an operation would likely be considered prohibitive. Nevertheless, we consider the relative lack of consideration given the DTL to have been an oversight and suggest, especially as the

speed and flexibility of digital circuitry is increasing, that future investigations consider this relatively obscure technique. It seems particularly promising for QAM signals or a CDMA single-carrier (forward link) signal.

A final recommendation to broaden the scope of carrier recovery research comes out of the problem of estimator bias due to asynchronous CDMA reverse link interference. Our brief analysis in section 7.3.1 suggests an investigation of a ML approach to phase estimation in CDMA systems. We believe that such an approach will necessarily utilize estimates of the relative phases of all CDMA users. As such, we believe that such an approach will be a perfect match for a variety of multiuser detection schemes, some of which are currently under investigation by my colleagues at the MPRG.

9.2.2 More Robust Adaptive Receiver Designs

High failure rates observed for adaptive receivers in both Chapters 7 and 8 continue to motivate further investigation in adaptive interference suppression for CDMA. One aspect of future investigation ought to dispense with BER as the primary figure of merit for such systems. Instead, a new and arguably better view could be provided by frame or packet error rates for wireless data systems and call-dropping or blocking rates for isochronous telephony. Such investigations would still pertain to carrier recovery in that the degradation of adaptive receiver systems due to differentially coherent reception remains demonstrably greater than that of conventional matched filter systems.

The fact that increasing the training interval from 100 to 1000 symbols for adaptive receivers did not significantly affect the high failure rates serves to point out that there may be a more fundamental weakness of the adaptive receivers in bad wireless channels. In most wireless digital systems and, even more so, in those employing CDMA, interleaving and forward error correction (FEC) are used to combat the periodic and dramatic reductions in received signal strength. Time did not permit the inclusion of these in this research and hence left us with raw, uncoded BER as the main figure of merit. We therefore believe that an important, perhaps the most important, future direction of research in adaptive interference suppresion for CDMA is in *linking* adaptive equalization at the front of the baseband receiver to the FEC at the back end as proposed by [58]. We, in fact, find the paucity of literature following up on this 1993 paper to be surprising. The authors thereof suggest that a highly reliable decision of whether or not to update the adaptive filter can be provided by the output of a decoder. If the decision to update is made, the Euclidean distance between the received vector of statistics and the highly reliable estimate of the transmitted symbol vector provide a highly reliable error for the update equation. The

marriage of adaptive equalization and simpler FEC methods may suggest lower-complexity or more bandwidth efficient alternatives to such powerful schemes as the constraint-length 9, rate 1/3 Viterbi decoder used on the IS-95 reverse link.

9.3 Chapter Summary

In this chapter, we have given a brief synopsis of the work described in this thesis. The emphasis in section 9.1 was primarily on pointing out the most important results among the dizzying myriad of lesser results contained in preceding chapters. This review served additionally as both a thematic and a chronological overview of the research. We concluded this report with suggestions and motivations for future endeavors in section 9.2. These are areas left relatively untouched not only by this work but by most known literature. Finally we point out, as we have abundantly before, that the surface has merely been scratched concerning the topic of carrier recovery for CDMA. What we have presented is intended to be a useful survey of the subject and to create fertile ground for future discovery.

Bibliography

[1] J. G. Proakis, *Digital Communications*, McGraw-Hill, NY, 3rd edition, 1995.

[2] S. C. Gupta, "Phase-locked loops", *Proc. of IEEE*, vol. 63, no. 2, pp. 291–306, Feb. 1975, Classic Tutorial: 188 refs.

[3] W. J. Gruen, "Theory of AFC synchronization", *Proc. of IRE*, vol. 41, pp. 1043–1048, Aug. 1953.

[4] J. P. Costas, "Synchronous communications", *Proc. of IRE*, vol. 44, pp. 1713–1718, Dec. 1956.

[5] A. Blanchard, *Phase-locked Loops: Application to Coherent Receiver Design*, Wiley & Sons,, NY, 1976.

[6] F. M. Gardner, *Phaselock Techniques*, Wiley & Sons, NY, 2nd edition, 1979.

[7] W. C. Lindsey, *Synchronization Systems in Communications and Control*, Prentice-Hall, Englewood Cliffs, NJ, 1972.

[8] W. C. Lindsey and M. K. Simon, *Telecommunication Systems Engineering*, Prentice-Hall, Englewood Cliffs, NJ, 1973.

[9] A. J. Viterbi, *Principles of Coherent Communication*, McGraw-Hill, NY, 1966.

[10] W. C. Lindsey and M. K. Simon, eds., *Phase-Locked Loops & Their Application*, IEEE Press, NY, 1978.

[11] W. C. Lindsey and C. M. Chie, eds., *Phase-Locked Loops*, IEEE Press, Pitscataway, NJ, 1986.

[12] W. C. Lindsey and C. M. Chie, "A survey of digital phase-locked loops", *Proc. of IEEE*, vol. 69, no. 4, pp. 410–431, Apr. 1981.

[13] S. C. Gupta, "On optimum digital phase-locked loops", *IEEE Trans. Comm. Tech.*, vol. 16, pp. 340–344, Apr. 1968.

[14] G. S. Gill and S. C. Gupta, "First order discrete phase-lock loop with applications to demodulation of angle-modulated carrier", *IEEE Trans. Comm.*, vol. 20, pp. 454–462, June 1972.

[15] I. S. Xezonakis and M. S. Sangriotis, "An all digital Costas loop-like PLL circuit with a wide locking range", *Int'nat'l Journal of Electronics*, vol. 71, no. 6, pp. 951–965, 1991.

[16] L. E. Franks, "Carrier and bit synchronization in data communication – a tutorial review", *IEEE Trans. Comm.*, vol. 28, no. 8, pp. 1107–1120, Aug. 1980, Classic Tutorial.

[17] J. J. Spilker, "The delay-lock discriminator – an optimum tracking device", *Proc. of IRE*, vol. 49, pp. 1403–1416, Sep 1961.

[18] J. J. Spilker, "Delay-lock tracking of binary signals", *IEEE Trans. on Space Electronics and Telemetry*, vol. SET-9, pp. 1–8, Mar. 1963.

[19] R. L. Didday and W. C. Lindsey, "Subcarrier tracking methods and communications system design", *IEEE Trans. Comm. Tech.*, vol. 16, no. 4, pp. 541–550, Aug. 1968.

[20] W. C. Lindsey and M. K. Simon, "The performance of suppressed carrier tracking loops in the presence of frequency detuning", *Proc. of IEEE*, vol. 58, no. 9, pp. 1315–1321, Sep 1970.

[21] W. C. Lindsey and M. K. Simon, "Carrier synchronization and detection of polyphase signals", *IEEE Trans. Comm., Concise Papers*, vol. 20, no. 6, pp. 441–454, June 1972.

[22] G. L. Hedin, J. K. Holmes, W. C. Lindsey, and K. T. Woo, "Theory of false lock in costas loops", *IEEE Trans. Comm.*, vol. 26, no. 1, pp. 1–12, Jan. 1978.

[23] M. K. Simon, "The false lock performance of costas loops with hard-limited in-phase channel", *IEEE Trans. Comm.*, vol. 26, no. 1, pp. 23–34, Jan. 1978.

[24] M. K. Simon, "Tracking performance of costas loops with hard-limited in-phase channel", *IEEE Trans. Comm.*, vol. 26, no. 4, pp. 420–432, Apr. 1978.

[25] W. C. Lindsey and M. K. Simon, "Optimum performance of suppressed carrier receivers with Costas loop tracking", *IEEE Trans. Comm.*, vol. 25, no. 2, pp. 215–227, Feb. 1977.

[26] F. D. Natali, "AFC tracking algorithms", *IEEE Trans. Comm.*, vol. 32, no. 8, pp. 935–947, Aug. 1984, Seminal Paper on AFC.

[27] F. M. Gardner, "Characteristics of frequency-tracking loops", in W. C. Lindsey and C. M. Chie, eds., *Phase-Locked Loops*, IEEE Press, Pitscataway, NJ, 1986, Good Intro to analog AFC.

[28] C. R. Cahn, "Improving frequency acquisition of a Costas loop", *IEEE Trans. Comm.*, vol. 25, no. 12, pp. 1453–1459, Dec. 1977.

[29] D. G. Messerschmitt, "Frequency detectors for PLL acquisition in timing and carrier recovery", *IEEE Trans. Comm.*, vol. 27, no. 9, pp. 1288–1295, Sep 1979.

[30] H. Sari and S. Moridi, "New phase and frequency detectors for carrier recovery in PSK and QAM systems", *IEEE Trans. Comm.*, vol. 36, no. 9, pp. 1035–1043, Sep 1988.

[31] A. N. D'Andrea and U. Mengali, "Performance of a quadricorrelator driven by modulated signals", *IEEE Trans. Comm.*, vol. 38, no. 11, pp. 1952–1957, Nov. 1990.

[32] A. N. D'Andrea and U. Mengali, "Design of quadricorrelators for automatic frequency control systems", *IEEE Trans. Comm.*, vol. 41, no. 6, pp. 988–997, June 1993.

[33] H. L. Van Trees, *Detection, Estimation, and Modulation Theory, part I: Detection, Estimation, and Linear Modulation Theory*, Wiley & Sons, NY, 1968.

[34] H. L. Van Trees, *Detection, Estimation, and Modulation Theory, part II: Nonlinear Modulation Theory*, Wiley & Sons, NY, 1971.

[35] H. L. Van Trees, *Detection, Estimation, and Modulation Theory, part III: Radar-Sonar Signal Processing and Gaussian Signals in Noise*, Wiley & Sons, NY, 1971.

[36] H. Meyr and G. Ascheid, *Synchronization in Digital Communications: Phase-, Frequency- Locked Loops, and Amplitude Control*, vol. 1, Wiley & Sons, NY, 1990.

[37] M. K. Simon and D. Divsalar, "The performance of trellis coded multilevel DPSK on a fading mobile satellite channel", *IEEE Trans. on Vehicular Tech.*, vol. 37, no. 2, pp. 78–91, May 1988.

[38] M. K. Simon and D. Divsalar, "Doppler-corrected differential detection of MPSK", *IEEE Trans. Comm.*, vol. 37, no. 2, pp. 99–109, Feb. 1989.

[39] D. Divsalar and M. K. Simon, "Multiple-symbol differential detection of MPSK", *IEEE Trans. Comm.*, vol. 38, no. 3, pp. 300–308, Mar. 1990.

[40] M. K. Simon and D. Divsalar, "Multiple-symbol, partially coherent detection of MPSK", *JPL New Technology Report* NPO-18932, July 1994.

[41] D. Divsalar and M. K. Simon, "Pseudocoherent demodulation of DPSK radio signals", *JPL New Technology Report* NPO-19205, June 1995.

[42] P. Y. Kam, "Maximum likelihood carrier phase recovery for linear suppressed-carrier digital data modulations", *IEEE Trans. Comm.*, vol. 34, no. 6, pp. 522–527, June 1986.

[43] O. C. Mauss, F. Classen, and H. Meyr, "Carrier frequency recovery for a fully digital direct-sequence spread spectrum receiver: A comparison", in *Proc. of IEEE Vehicular Technology Conference*, Secaucus, NJ, May 1993, pp. 392–395.

[44] F. Classen, H. Meyr, and P. Seheir, "Maximum likelihood open loop carrier synchronizer for digital radio", in *Proc. of IEEE Int'nat'l Conf. on Communications (ICC '93)*, Geneva, Switz., 1993, pp. 493–497.

[45] K. E. Scott and E. B. Olasz, "Simultaneous clock phase and frequency offset estimation", *IEEE Trans. Comm.*, vol. 43, no. 7, pp. 2263–2270, July 1995.

[46] G. Karam, et al., "A reduced-complexity frequency detector derived from the maximum-likelihood principle", *IEEE Trans. Comm.*, vol. 43, no. 10, pp. 2641–2650, Oct. 1995.

[47] M. K. Simon, H. Tsou, and S. M. Hinedi, "Closed loop carrier phase synchronization techniques motivated by likelihood functions", *JPL New Technology Report* NPO-19377, Apr. 1996.

[48] B. Y. Chung, et al., "Performance analysis of an all-digital BPSK direct sequence spread spectrum IF receiver architecture", *IEEE JSAC*, vol. 11, no. 7, pp. 1096–1106, Sep 1993.

[49] C. M. Chie and W. C. Lindsey, "Phase-locked loops: Applications, performance measures, and summary of analytical results", in W. C. Lindsey and C. M. Chie, eds., *Phase-Locked Loops*, IEEE Press, Pitscataway, NJ, 1986.

[50] C. H. Wei and W. J. Chen, "Digital tanlock loop for tracking pi/4-DQPSK signals in digital cellular radio", *IEEE Trans. on Vehicular Tech.*, vol. 43, no. 3, pp. 474–479, Aug. 1994.

[51] K. M. Aleong, H. Leib, and P. Kabal, "A technique for combining equalization with generalized differential detection", in *Proc. of IEEE 12th Annual Phoenix Conf. on Computers and Communications*, Phoenix, AZ, Mar. 1993, pp. 416–422.

[52] M. V. Majmundar, "Adaptive single-user receivers for direct sequence CDMA systems", Master's thesis, Virginia Polytechnic Institute and State University, Blacksburg, VA, April 1996.

[53] N. Zecevic, "Techniques and adaptation algorithms for direct-sequence spread-spectrum CDMA single-user detection", Master's thesis, Virginia Polytechnic Institute and State University, Blacksburg, VA, July 1996.

[54] H. Taub and D. L. Schilling, *Principles of Communication Systems*, McGraw-Hill, NY, 2nd edition, 1986.

[55] R. C. Dixon, *Spread Spectrum Systems with Commercial Applications*, Wiley & Sons, NY, 3rd edition, 1994.

[56] M. C. Jeruchim, P. Balaban, and K. S. Shanmugan, *Simulation of Communication Systems*, Plenum Press, NY, 1992.

[57] COST 207: Digital Land Mobile Radio Communications, "Final report", Office for Official Publications of the European Communities, Brussels, 1989, ISBN 92-825-9946-9.

[58] R. Sharma, W. D. Grover, and W. A. Krzymien, "Forward-error-control (FEC)-assisted adaptive equalization for digital cellular mobile radio", *IEEE Trans. on Vehicular Tech.*, vol. 42, no. 1, pp. 94–102, Feb. 1993.

[59] W. H. Beyer, Ed., *CRC Standard Mathematical Tables and Formulae*, CRC Press, Boca Raton, FL, 29th edition, 1981.

Author's Biographical Sketch

Steven P. Nicoloso was born on September 20, 1966 in Portland, OR. He received his B.S. degree, *summa cum laude*, in social science education, from Liberty University in 1988. In 1992, after the birth of his first child, Mr. Nicoloso changed career paths and returned to college to pursue a degree in electrical engineering. In 1993, he entered Virginia Tech to take undergraduate background coursework. From 1995 to the present, he has worked as a graduate research assistant for the Mobile and Portable Radio Research Group. His research interests center in applying DSP techniques and hardware to the communication systems and include interference rejection, adaptive antenna arrays, and software radio concepts. He is happily married and the proud father of currently two wonderful children.